

2012

MAGNETIC AND ORBITAL ORDERS COUPLED TO NEGATIVE THERMAL EXPANSION IN MOTT INSULATORS, CA₂RU₁-XMXO₄ (M = 3D TRANSITION METAL ION)

Tongfei Qi

University of Kentucky, tongfei324@msn.com

[Right click to open a feedback form in a new tab to let us know how this document benefits you.](#)

Recommended Citation

Qi, Tongfei, "MAGNETIC AND ORBITAL ORDERS COUPLED TO NEGATIVE THERMAL EXPANSION IN MOTT INSULATORS, CA₂RU₁-XMXO₄ (M = 3D TRANSITION METAL ION)" (2012). *Theses and Dissertations--Physics and Astronomy*. 6.
https://uknowledge.uky.edu/physastron_etds/6

This Doctoral Dissertation is brought to you for free and open access by the Physics and Astronomy at UKnowledge. It has been accepted for inclusion in Theses and Dissertations--Physics and Astronomy by an authorized administrator of UKnowledge. For more information, please contact UKnowledge@lsv.uky.edu.

STUDENT AGREEMENT:

I represent that my thesis or dissertation and abstract are my original work. Proper attribution has been given to all outside sources. I understand that I am solely responsible for obtaining any needed copyright permissions. I have obtained and attached hereto needed written permission statements(s) from the owner(s) of each third-party copyrighted matter to be included in my work, allowing electronic distribution (if such use is not permitted by the fair use doctrine).

I hereby grant to The University of Kentucky and its agents the non-exclusive license to archive and make accessible my work in whole or in part in all forms of media, now or hereafter known. I agree that the document mentioned above may be made available immediately for worldwide access unless a preapproved embargo applies.

I retain all other ownership rights to the copyright of my work. I also retain the right to use in future works (such as articles or books) all or part of my work. I understand that I am free to register the copyright to my work.

REVIEW, APPROVAL AND ACCEPTANCE

The document mentioned above has been reviewed and accepted by the student's advisor, on behalf of the advisory committee, and by the Director of Graduate Studies (DGS), on behalf of the program; we verify that this is the final, approved version of the student's dissertation including all changes required by the advisory committee. The undersigned agree to abide by the statements above.

Tongfei Qi, Student

Dr. Gang Cao, Major Professor

Dr. Tim Gorringer, Director of Graduate Studies

MAGNETIC AND ORBITAL ORDERS COUPLED TO NEGATIVE THERMAL
EXPANSION IN MOTT INSULATORS, $\text{Ca}_2\text{Ru}_{1-x}\text{M}_x\text{O}_4$ (M = 3D
TRANSITION METAL ION)

DISSERTATION

A dissertation submitted in partial
fulfillment of the requirements for
the degree of Doctor of Philosophy
in the College of Arts and Sciences
at the University of Kentucky

By
Tongfei Qi
Lexington, Kentucky

Director: Dr. Gang Cao, Professor of Physics
Lexington, Kentucky 2012

Copyright© Tongfei Qi 2012

ABSTRACT OF DISSERTATION

MAGNETIC AND ORBITAL ORDERS COUPLED TO NEGATIVE THERMAL EXPANSION IN MOTT INSULATORS, $\text{Ca}_2\text{Ru}_{1-x}\text{M}_x\text{O}_4$ (M = 3D TRANSITION METAL ION)

Ca_2RuO_4 is a structurally-driven Mott insulator with a metal-insulator (MI) transition at $T_{MI} = 357\text{K}$, followed by a well-separated antiferromagnetic order at $T_N = 110\text{ K}$. Slightly substituting Ru with a 3d transition metal ion M effectively shifts T_{MI} and induces exotic magnetic behavior below T_N . Moreover, M doping for Ru produces negative thermal expansion in $\text{Ca}_2\text{Ru}_{1-x}\text{M}_x\text{O}_4$ (M = Cr, Mn, Fe or Cu); the lattice volume expands on cooling with a total volume expansion ratio, $\Delta V/V$, reaching as high as 1%. The onset of the negative thermal expansion closely tracks T_{MI} and T_N , sharply contrasting classic negative thermal expansion that shows no relevance to electronic properties. In addition, the observed negative thermal expansion occurs near room temperature and extends over a wide temperature interval. These findings underscores new physics driven by a complex interplay between orbital, spin and lattice degrees of freedom. These materials constitute a new class of Negative Thermal Expansion (NTE) materials with novel electronic and magnetic functions.

KEYWORDS: Transition Metal Oxide, Ruthenate, Negative Thermal Expansion, Single crystal XRD, Invar Effect, Orbital Ordering, Magnetic Ordering, Jahn-Teller Effect

Author's signature: _____ Tongfei Qi

Date: _____ December 5, 2012

MAGNETIC AND ORBITAL ORDERS COUPLED TO NEGATIVE THERMAL
EXPANSION IN MOTT INSULATORS, $\text{Ca}_2\text{Ru}_{1-x}\text{M}_x\text{O}_4$ ($\text{M} = 3\text{D}$
TRANSITION METAL ION)

By
Tongfei Qi

Director of Dissertation: Gang Cao

Director of Graduate Studies: Tim Gorringer

Date: December 5, 2012

ACKNOWLEDGMENTS

First I would like to thank my advisor Dr. Gang Cao for his detailed guidance, support and encouragement in every step I made in these years. I greatly benefit from his profound knowledge and scientific insight throughout my PhD study. I sincerely appreciate his instructions and help in assisting me to finish my dissertation. The state of the art crystal growth capability and the extensive research facilities I enjoyed in our lab were invaluable. I would also like to acknowledge my committee: Professor Joe Brill, Professor Lance DeLong, Professor Sean Parkin, Professor Yu-Ming Zhang for sharing their valuable time and providing me with helpful feedback of this dissertation.

A large part of my Ph.D. work concerns structural analysis. Thus I would like to thank all the structure people I worked and talked with. Sean, thank you for initiating me in using diffractometer, teaching me all the knowledge and sharing with me your experience in crystallography. Thanks for the 2012 Neutron-Xray Summer school, the soundly lectures were of great help for studying the structural analysis.

I would like to acknowledge the collaboration we had with Dr. Feng Ye from Oak Ridge National Laboratory.

This work would never have become reality without the help and suggestions of many supportive friends and colleagues: Vino, Shaline, Sasha, Angela, Wenhai, Min, Bishnu, Li, Kamal, Erfan, Jasminka, Shujuan. I am really grateful for their cooperation in crystal growth, data collection and analysis of my research.

Thanks for all the people in Physics Department main office, Carol, Eva, Diane, Tammy, Melissa, Angela for handling all the paperwork and all administrative matters, and for their personal support and friendship.

I also want to thank all the technical staffs in the machine, electronics and vacuum shops of our department for their help in using the setup and especially for trouble shooting the devices.

I send my thanks to all my friends in University of Kentucky: Daheng He, Emily Bittle, John Nichols, Gretchen Phelps, Ben Crider, Anton Spektorov, Qiaoli Yang, Ming Gong, Ye Wang, Mingyang Sun, Jae-Hyuk Oh, Archisman Ghosh, Vinayak Bhat, Abhishek Sundararajan.

My final and most heartfelt acknowledgement must go to my family. I greatly thank my parents, my wife Yinglei and my son Ethan for their endless love and supporting my decision to pursue the Ph.D. and Work in research as well as live in a country with a different culture constituted a challenge from which I had a lot to learn. I made a big step forward and it is my pleasure to take this opportunity to thank all the people contributing to it.

This work was supported by NSF grants DMR-0552267, DMR-0856234 and EPS-0814194.

TABLE OF CONTENTS

Acknowledgments	iii
Table of Contents	v
List of Figures	vii
List of Tables	xi
Chapter 1 Introduction	1
1.1 Transition Metal Oxides	1
1.2 Perovskites and the Ruddlesden-Popper Series	1
1.3 Negative Thermal Expansion	3
1.4 Outline of the Thesis	7
Chapter 2 Theoretical Background	8
2.1 Crystal Structure and X-ray crystallography	8
2.1.1 Bragg's Law and X-ray Diffraction	8
2.1.2 Crystal and Reciprocal Lattice	9
2.1.3 Structure Factors and Structure Refinement	12
2.2 Metal-Insulator Transition	15
2.2.1 Metals and Insulators	15
2.2.2 Mott-Hubbard Transition	17
2.2.3 Disorder Induced Metal-Insulator Transitions	18
2.3 Magnetism	19
2.3.1 Hund's Rules	20
2.3.2 Spin Orbit Coupling	20
2.3.3 Crystal Field Environment	22
2.3.4 The Jahn-Teller Effect	24
2.4 Exchange Interaction	25
2.4.1 Direct Exchange	26
2.4.2 Indirect Exchange	27
2.4.3 Superexchange	28
2.4.4 Double Exchange	28
2.4.5 Anisotropic Exchange Interaction	29
Chapter 3 Experimental Methods	31
3.1 Single Crystal Synthesis	31
3.1.1 Floating-Zone Technique	31
3.1.2 Flux Technique	33
3.2 Structural Characterization	34
3.2.1 Energy Dispersive X-ray	34

3.2.2	Powder X-ray Diffraction	35
3.2.3	Single Crystal X-ray Diffraction	37
3.3	Physical Properties Measurement	39
3.3.1	Magnetization and Susceptibility Measurement	39
3.3.2	Resistivity Measurement	41
3.3.3	Specific Heat Measurement	42
Chapter 4	Novel Mechanism in Doped Ca_2RuO_4	45
4.1	Ca_2RuO_4	45
4.2	$\text{Ca}_2\text{Ru}_{1-x}\text{Cr}_x\text{O}_4$	46
4.2.1	Structure of $\text{Ca}_2\text{Ru}_{1-x}\text{Cr}_x\text{O}_4$	46
4.2.2	Temperature dependence of the $\text{Ca}_2\text{Ru}_{1-x}\text{Cr}_x\text{O}_4$	48
4.2.3	Cr concentration dependence of the $\text{Ca}_2\text{Ru}_{1-x}\text{Cr}_x\text{O}_4$	52
4.3	$\text{Ca}_2\text{Ru}_{1-x}\text{Mn}_x\text{O}_4$	61
4.3.1	Negative Thermal Expansion in $\text{Ca}_2\text{Ru}_{1-x}\text{Mn}_x\text{O}_4$	61
4.3.2	Temperature dependence of the $\text{Ca}_2\text{Ru}_{1-x}\text{Mn}_x\text{O}_4$	62
4.3.3	Mn concentration dependence of the $\text{Ca}_2\text{Ru}_{1-x}\text{Mn}_x\text{O}_4$	65
4.4	$\text{Ca}_2\text{Ru}_{1-x}\text{Fe}_x\text{O}_4$	68
4.4.1	Negative Thermal Expansion in $\text{Ca}_2\text{Ru}_{1-x}\text{Fe}_x\text{O}_4$	68
4.4.2	Temperature dependence of the $\text{Ca}_2\text{Ru}_{1-x}\text{Fe}_x\text{O}_4$	69
4.4.3	Fe concentration dependence of the $\text{Ca}_2\text{Ru}_{1-x}\text{Fe}_x\text{O}_4$	71
4.4.4	Magnetization Reversal in $\text{Ca}_2\text{Ru}_{1-x}\text{Fe}_x\text{O}_4$	72
4.5	$\text{Ca}_2\text{Ru}_{1-x}\text{M}_x\text{O}_4$, $\text{M} = 3\text{d transition metal ion}$)	75
Chapter 5	Conclusions	78
5.1	The New Type of NTE in $\text{Ca}_2\text{Ru}_{1-x}\text{M}_x\text{O}_4$	78
5.2	New Theoretical Paradigm in $\text{Ca}_2\text{Ru}_{1-x}\text{M}_x\text{O}_4$	78
	Bibliography	81

LIST OF FIGURES

1.1	Ruddlesden-Popper series with chemical formula $A_{n+1}B_nO_{3n+1}$, for $n=1$, 2, 3 and ∞	2
1.2	Schematic phase diagram (T vs W/U) for $Ca_{n+1}Ru_nO_{3n+1}$ and $Sr_{n+1}Ru_nO_{3n+1}$	3
1.3	An asymmetric interatomic potential well: dependence of the potential energy E on the inter-atomic spacing r for a diatomic molecule.	4
1.4	A schematic representation of how transverse thermal vibrations of M-O-M bonds can give rise to linear NTE in oxide structures.	6
1.5	Crystal structure of single crystal ZrW_2O_8 . ZrO_6 octahedra shown in blue, WO_4 tetrahedra shown in orange.	6
2.1	Illustration of the fulfillment of the Bragg's equation.	9
2.2	Illustration of a unit cell in (a) 2-dimensions and (b) 3-dimensions showing cell parameters.	10
2.3	Illustration of various planes and their (hkl) identification in a 2-dimensional lattice. One square block represents a unit cell; Blue dotted lines are sets of atomic planes.	10
2.4	Illustration of real (in red) and reciprocal (in blue) lattices.	11
2.5	Density of states as a function of band energy for electrons that are (a) independent (b) nearly independent (weakly correlated) (c) strongly correlated and (d) localized.	16
2.6	Illustration of the upper and lower Hubbard bands in Mott insulator as a function of reciprocal interatomic distance. Here U ($U = I - A$) is the intra-atomic energy and W is the bandwidth.	17
2.7	Schematic pictures of the density of states in a disordered system. E_c and E'_c represent the mobility edges, that separate the localized states in the band tails (shaded areas) from the extended states in the band center.	19
2.8	Illustration of angular distribution of the d-orbitals. The $d_{x^2-y^2}$ and d_{z^2} orbitals are grouped together and called the e_g levels. The d_{xy} , d_{yz} , and d_{xz} orbitals are grouped together and called the t_{2g} levels.	22
2.9	Splitting of the electronic d orbitals due to the crystal field in (a) octahedral and (b) tetrahedral environment.	23
2.10	Illustration of the Jahn-Teller effect for Mn^{3+} ($3d^4$). A distorted octahedral complex splits the t_{2g} and e_g levels.	25
2.11	Direct exchange energy as a function of the interatomic distance r divided by the radius of the d orbital r_d . The curve is known as the Bethe-Slater curve.	26
2.12	The coefficient of RKKY exchange as a function of the interatomic distance r multiplied by the radius of the Fermi sphere k_F	27
2.13	Schematic illustration of the superexchange interaction between two magnetic ions M mediated by a non-magnetic oxygen atom.	28

2.14	Double exchange mechanism gives ferromagnetic coupling between metallic ions with different oxidation states. In a (a) FM configuration, electron delocalization is possible due to the lowering of kinetic energy. In a (b) AFM configuration, electron delocalization is not possible.	29
3.1	A Schematic diagram of the optical floating zone furnace.	32
3.2	(a) Feed rod preparation. (b) FZ furnace in action during a crystal growth. (c) Different stages in a crystal growth. (d) Actual size of single crystal $\text{Ca}_2\text{Ru}_{1-x}\text{Cr}_x\text{O}_4$	33
3.3	Some representative crystals of recently grown using flux techniques. . .	34
3.4	EDX spectrum of a single crystal of $\text{Ca}_2\text{Ru}_{1-x}\text{Cr}_x\text{O}_4$ studied in this work, with corresponding element peaks labeled.	35
3.5	Schematic diagram of a powder X-ray diffractometer in θ - 2θ configuration.	36
3.6	Schematic of the classical four-circle single-crystal X-ray diffractometer. .	37
3.7	Nonius kappaCCD $\text{MoK}\alpha$ X-ray diffractometer.	38
3.8	Diffraction pattern from Ca_2RuO_4 sample obtained with the Kappa CCD diffractometer. Each point in reciprocal space represents a family of atomic planes in real space.	38
3.9	Illustration of DC-SQUID and V (Φ/Φ_0) for constant bias current I	39
3.10	Schematic cross-section of the Quantum Design MPMS.	40
3.11	(a) Schematic diagrams of the four-leads method measurement for in-plane resistivity; (b)Equivalent circuit of four-point probe setup for resistivity measurements.	41
3.12	(a) Illustration of Two-Tau model for sample and sample holder; (b) schematic drawing of microcalorimeter sample holder design.	42
3.13	(a) A heat pulse input; (b) The change of sample temperature in a microcalorimeter as a function of time due to the heat applied.	43
4.1	Temperature dependence of the a- and b-axis lattice parameters, and the ab-plane resistivity ρ_{ab} (right scale) for Ca_2RuO_4	45
4.2	Room-temperature structure of $\text{Ca}_2\text{Ru}_{1-x}\text{Cr}_x\text{O}_4$ with projection onto the ac plane and the ab plane.	48
4.3	Temperature dependences of lattice parameters a-, b- and c-axis (right scale)for $x = 0.067$	49
4.4	Temperature dependences of unit cell volume V and thermal expansion ratio V/V (right scale) for $x = 0.067$	49
4.5	(a) Temperature dependence of the tilt, rotation and bond angles in $\text{Ca}_2\text{Ru}_{1-x}\text{Cr}_x\text{O}_4$ ($x = 0.67$), obtained from single-crystal X-ray diffraction; and (b) definition of $\Theta\text{-O1}$, $\Theta\text{-O2}$ and Ru-O-Ru distortion angles. .	50
4.6	Temperature dependences of ab-plane resistivity ρ_{ab} and magnetic susceptibility χ_{ab} (right scale)at $\mu_0 H = 0.5$ T for $x = 0.067$	51
4.7	Fit of the electrical resistivity in the ab plane, $\rho_{ab}(T)$, of single crystal $\text{Ca}_2\text{Ru}_{1-x}\text{Cr}_x\text{O}_4$ for $x = 0.032$ to variable-range hopping with $n = 3$. Inset: (a) Fit to activation-type insulating behavior were not good; and (b) variable-range hopping with $n = 1$ is less good.	52

4.8	Cr concentration x dependence of the a -, b - and c -axis lattice parameters (right scale) for $T = 90$ K.	53
4.9	Ru-O1-Ru bond angle θ and the Ru-O2 bond distance (right scale) for $T = 90$ K. Inset: Schematics of the distorted Ru-O1-Ru bond angle θ and a RuO6 octahedron.	56
4.10	Unit cell volume V for $T = 90$ K and 295 K, and thermal expansion ratio $[V(295K)-V(90K)]/V(295K)$ (right scale) for $0 \leq x \leq 0.135$	57
4.11	Temperature dependences of the ab -plane resistivity ρ_{ab} for $\text{Ca}_2\text{Ru}_{1-x}\text{Cr}_x\text{O}_4$ with $0 \leq x \leq 0.135$	57
4.12	The magnetic susceptibility χ_{ab} at applied field $\mu_0 H = 0.5$ T for $\text{Ca}_2\text{Ru}_{1-x}\text{Cr}_x\text{O}_4$ with $0 \leq x \leq 0.135$	58
4.13	T_N , T_C and Curie-Weiss temperature Θ_{CW} for $\text{Ca}_2\text{Ru}_{1-x}\text{Cr}_x\text{O}_4$ with different x	59
4.14	The isothermal magnetization $M(H)$ at 100 K for representative compositions $x = 0$ and 0.032.	59
4.15	The T - x phase diagram summarizing observed phase transitions and phase types. Right scale shows the Cr concentration (x) dependence of the thermal expansion ratio $\Delta V/V$. Note that the hatched region represents NVTE.	60
4.16	For $\text{Ca}_2\text{Ru}_{1-x}\text{Mn}_x\text{O}_4$ with $0 < x < 0.25$, x dependence of (a) the lattice parameter a -, b - and c -axis (right scale) at $T = 90$ K and (b) unit cell volume V and thermal expansion ratio $\Delta V/V = [V(295K)-V(90K)]/V(295K)$ (right scale). Note that $\Delta V/V$ is only for $90 \text{ K} \leq T \leq 295 \text{ K}$, and this value is much greater for $90 \text{ K} \leq T \leq T_{MI} \sim 380 \text{ K}$	61
4.17	For $\text{Ca}_2\text{Ru}_{1-x}\text{Mn}_x\text{O}_4$ with $x = 0.10$, temperature dependences of (a) lattice parameters a -, b - and c -axis (right scale), (b) unit cell volume V and (c) magnetic susceptibility χ_{ab} at $\mu_0 H = 0.1$ T (field cooled) and ab -plane resistivity ρ_{ab} (right scale). The shaded area indicates the concomitant occurrence of the NTE and MI transition.	63
4.18	For $\text{Ca}_2\text{Ru}_{1-x}\text{Mn}_x\text{O}_4$ with $x = 0.25$, temperature dependences of (a) lattice parameters a -, b - and c -axis (right scale), (b) unit cell volume V and (c) the magnetic susceptibility χ_{ab} at $\mu_0 H = 0.1$ T (field cooled) and the ab -plane resistivity ρ_{ab} (right scale).	64
4.19	Temperature dependence of the ab -plane resistivity ρ_{ab} for $\text{Ca}_2\text{Ru}_{1-x}\text{Mn}_x\text{O}_4$ with $0 < x < 0.25$	65
4.20	Temperature dependence of the magnetic susceptibility χ_{ab} for $\text{Ca}_2\text{Ru}_{1-x}\text{Mn}_x\text{O}_4$ with $0 < x < 0.25$	66
4.21	The isothermal magnetization M_{ab} for $\text{Ca}_2\text{Ru}_{1-x}\text{Mn}_x\text{O}_4$ with $0 < x < 0.25$	67
4.22	Temperature dependence of the specific heat $C(T)$ for $\text{Ca}_2\text{Ru}_{1-x}\text{Mn}_x\text{O}_4$ with $0 < x < 0.25$. Inset: enlarged $C(T)$ near T_N . Note that T_N and the order moment increase with x	67
4.23	For $\text{Ca}_2\text{Ru}_{1-x}\text{Fe}_x\text{O}_4$ with $0 < x < 0.22$, x dependence of (a) the lattice parameters a -, b - and c -axis (right scale) and (b) unit cell volume V at $T = 90$ K and 295 K ; thermal expansion ratio $\delta V/V = [V(295K)-V(90K)]/V(295K)$ for $0 \leq x \leq 0.22$	69

4.24	For $\text{Ca}_2\text{Ru}_{1-x}\text{Fe}_x\text{O}_4$ with $x = 0.08$, temperature dependences of (a) lattice parameters a -, b - and c -axis (right scale), (b) lattice volume V and specific heat $C(T)$ (right scale) and (c) magnetic susceptibility χ_{ab} at $\mu_0 H = 0.1$ T (field cooled) and ab -plane resistivity ρ_{ab} (right scale).	70
4.25	For $\text{Ca}_2\text{Ru}_{1-x}\text{Fe}_x\text{O}_4$ with $x = 0.08, 0.091$ and 0.122 , temperature dependences of (a) ab -plane resistivity ρ_{ab} , (b) specific heat $C(T)$	71
4.26	Temperature dependence of the magnetic susceptibility χ_{ab} at $\mu_0 H = 0.1$ T (field cooled) for $\text{Ca}_2\text{Ru}_{1-x}\text{Fe}_x\text{O}_4$ with $x = 0$ (right scale), $0.08, 0.091$ and 0.122	72
4.27	Temperature dependence of the magnetization M_{ab} at $B = 0.1\text{T}, 1\text{T}, 2\text{T}, 3\text{T}, 5\text{T}$ and 7T (field cooled) for $\text{Ca}_2\text{Ru}_{1-x}\text{Fe}_x\text{O}_4$ with $x = 0.091$	73
4.28	For $\text{Ca}_2\text{Ru}_{1-x}\text{Fe}_x\text{O}_4$ with $x = 0.091$, (a) isothermal magnetization M on ab plane at $5\text{K}, 30\text{K}, 60\text{K}, 80\text{K}, 100\text{K}$ and 120K ; (b) Field dependence of magnetization M at 5K for the Field Cooled and Zero Field Cooled sequences.	74
4.29	Temperature dependences of lattice parameters a -axis for $x = 0, 0.10$ (Mn) and 0.08 (Fe).	75
4.30	Temperature dependences of the Ru/M-Ru/M distance d and the Ru/M-O1-Ru/M bond angle θ (right scale) for $x = 0.08$ (Fe). Inset: schematics illustrating changes of d and θ on cooling.	76

LIST OF TABLES

4.1	Experimental and refinement details of $\text{Ca}_2\text{Ru}_{1-x}\text{Cr}_x\text{O}_4$ ($x = 0.067$) at selected temperatures.	47
4.2	Experimental and refinement details of $\text{Ca}_2\text{Ru}_{1-x}\text{Cr}_x\text{O}_4$ with different x	54
4.3	Structure refinement results of $\text{Ca}_2\text{Ru}_{1-x}\text{Cr}_x\text{O}_4$ with different x at 90 K.	55

Chapter 1 Introduction

1.1 Transition Metal Oxides

Transition metal oxides (TMO) have a long history and have received considerable attention in condensed matter physics due to their special structural, mechanical, physical and electronic properties [1–4]. In recent years they have aroused new interest with the discovery of high-temperature superconductivity, colossal magnetoresistance and high capacity batteries [5–12]. The TMOs form a large, rich and still not well understood class of compounds. Many of these properties strongly depend on the defect structures within a material, such as vacancies [13, 14], dislocations [15], stacking faults [16, 17] and grain boundaries [18, 19], which can affect local bonding of oxygen in the structure. The unusual properties of TMOs are clearly due to the unique nature of the outer shell electrons. The strong interactions between valence electrons and superexchange interactions via oxygen [20, 21], together with other interactions, ensure that TMOs are strongly correlated systems. TMOs include a wide variety of basic structure types: rocksalt, spinel, corundum, perovskite, rutile, garnet, pyrochlore and others. In particular, TMOs with structures derived from metal-oxygen MO_6 octahedra (usually the perovskite, rutile or pyrochlore structure types) display an array of exotic properties with potential or proven technological applications [22–24].

1.2 Perovskites and the Ruddlesden-Popper Series

Perovskite is a mineral composed of CaTiO_3 , which was named after the Russian mineralogist Lev Aleksevich von Perovski [25]. Perovskites have the general chemical formula ABX_3 , where A and B are both cations of very different sizes and X is an anion bonded to both [26, 27]. Although most perovskites share the same canonical structure, their physical properties exhibit tremendous variation from element to element, and as a consequence, they have a wide range of potential applications. The ideal Perovskite structure is cubic with atom B in the center, A at the eight corners and with face centers are occupied by X. This structure can be easily altered by temperature changes, pressure, oxygen vacancies or by dopants with different ionic radius. This variability gives us the freedom to manipulate TMO materials and thereby tune their interesting physical properties.

In a perfect perovskite structure, corner sharing BX_6 octahedra surround interstitial A cations [28]. In an idealized cubic perovskite constructed of rigid spheres, each cation has the perfect size to be in contact with an anion. In such case the unit cell axis can be determined from the following equation:

$$a = \sqrt{2}(r_A + r_X) = 2(r_B + r_X) \quad (1.1)$$

Where r_A , r_B and r_X represent the relative ionic radius of different elements. In the case of the A cation size being too big to remain in contact with the anions in the

cubic structure, the BX_6 octahedra will be tilted and the B-O-B links will thus bend slightly to bring some anions into contact with the A cations [28]. This requires a constant t to be introduced to describe the distortion, thus:

$$t\sqrt{2}(r_A + r_X) = 2(r_B + r_X)$$

or $t = \frac{2(r_B + r_X)}{\sqrt{2}(r_A + r_X)}$ (1.2)

This quantity t is named the *tolerance factor*, and was first derived by Goldschmidt [29]. Thus when $t = 1$, the structure can hold the ideal geometrical ratio of A-O and B-O bond lengths. The tolerance factor is a good indicator of the stability and distortion of these TMO crystal structures [30]. Perovskite structures with tolerance factors within the range from 0.75 to 1.0 preserve cubic symmetry.

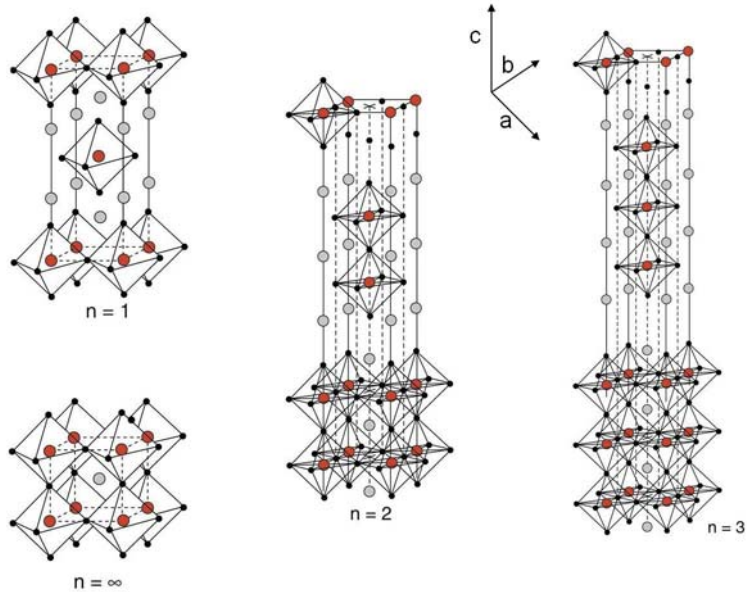


Figure 1.1: Ruddlesden-Popper series with chemical formula $A_{n+1}B_nO_{3n+1}$, for $n=1, 2, 3$ and ∞ .

The Ruddlesden-Popper series is a special group of layered perovskites that is named after S.N. Ruddlesden and P. Popper [31, 32]. This type of crystal consists of rock salt type layers and perovskite-like layers [33], which leads to the general formula $AX(ABX_3)_n$. Here A and B are cations, X is an anion and n indicates how many layers of octahedra are in the perovskite-like structure (see Fig. 1.1). The Ca_2RuO_4 crystal studied in this work is an example of the $n = 1$ member of a group of 4d-based Ruddlesden-Popper type ruthenates, which have the general formula $A_{n+1}Ru_nO_{3n+1}$ with $n = 1, 2, 3, \infty$ ($A = Ca$ or Sr).

The Coulomb interaction U is generally comparable to the 4d-bandwidth W in these ruthenates, which leaves them precariously balanced on the border between

metallic and insulating behavior, and/or on the verge of long-range magnetic order as shown in Fig. 1.2. Note the ground state can be readily changed by changing the cation, and that physical properties can be systematically tuned by altering the number of Ru-O layers [34]. In this phase diagram, SC stands for superconductor, FM-M means ferromagnetic metal, AFM-I stands for antiferromagnetic insulator, PM-M means paramagnetic metal and M-M indicates magnetic metal. As the dimensionality of the structure increases with n , the materials start to demonstrate metallic behavior and magnetic interactions are suppressed.

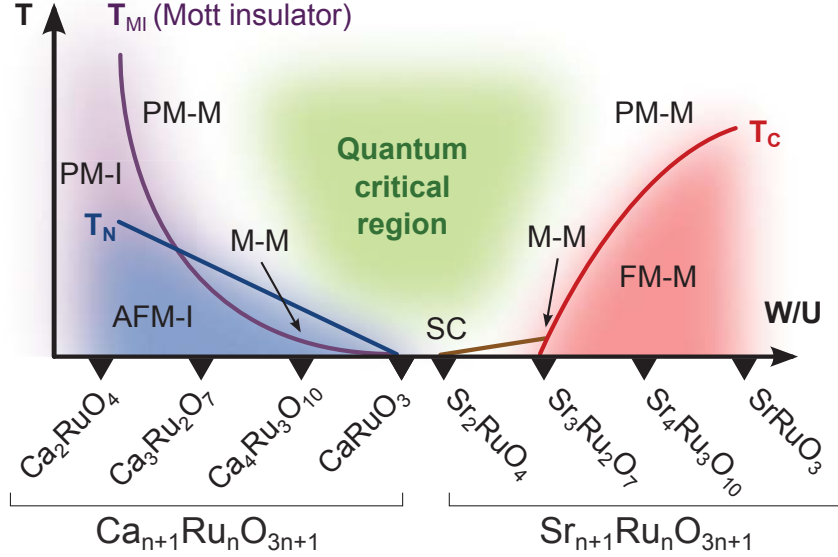


Figure 1.2: Schematic phase diagram (T vs W/U) for $\text{Ca}_{n+1}\text{Ru}_n\text{O}_{3n+1}$ and $\text{Sr}_{n+1}\text{Ru}_n\text{O}_{3n+1}$.

A common characteristic of these materials is that underlying physical properties are critically linked to the lattice and orbital degrees of freedom, and tend to exhibit a non-linear or so-called "giant" response to modest lattice changes. This is illustrated by observations of a p-wave superconducting state in Sr_2RuO_4 [6] and a first-order metal-insulator transition at $T_{MI} = 357$ K in Ca_2RuO_4 that is more structurally distorted due to the smaller ionic radius $r_{\text{Ca}} < r_{\text{Sr}}$ [35,36]. In Ca_2RuO_4 , the metal-insulator transition induces a radical change in electrical resistivity $\rho(T)$ by over nine orders of magnitude between 70 K and T_{MI} [35,36], which also marks a concomitant and particularly violent structural transition between a high-T tetragonal and a low-T orthorhombic phase.

1.3 Negative Thermal Expansion

Thermal expansion is an important property of materials for many engineering applications. Most materials expand on heating. The thermal expansion of a diatomic molecule is the simplest case, and can be explained by the asymmetric interatomic potential well (see Figure 1.3). Vibrational amplitudes increase with temperature,

which leads to an increase in time average bond distance due to the asymmetry. If the interatomic potential was perfectly harmonic, the average distance would be the same for all vibrational energies and then zero expansion would be observed.

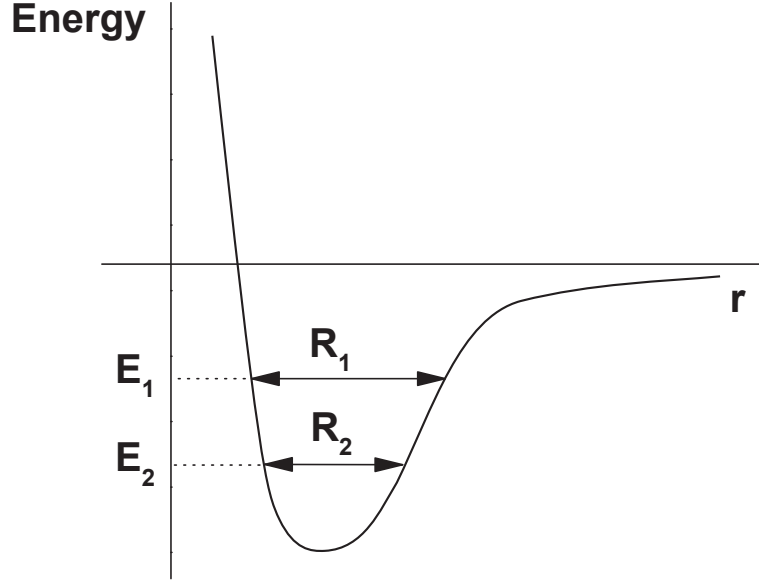


Figure 1.3: An asymmetric interatomic potential well: dependence of the potential energy E on the inter-atomic spacing r for a diatomic molecule.

For a single crystal, the situation becomes more complicated. Higher thermal energy leads to higher energy vibration that results in thermal expansion. Here, the *coefficient of thermal expansion* (CTE or α) was introduced in order to quantitatively measure and compare the extent of thermal expansion. The linear CTE α_L can be defined as:

$$\alpha_L = \frac{L_f - L_0}{L_0(T_f - T_0)} = \frac{1}{L_0} \frac{dL}{dT} \quad (1.3)$$

where L_0 and L_f represent the original and final values of the lattice constant with the temperature change from T_0 to T_f . Then α_L represents the relative change in linear dimensions per unit of temperature change. In a three dimensional case, e.g. in a crystal, heating or cooling affects all the dimensions, with a resultant change in volume. The volume CTE α_V may be determined from:

$$\alpha_V = \frac{V_f - V_0}{V_0(T_f - T_0)} = \frac{1}{V_0} \frac{dV}{dT} \quad (1.4)$$

where V_f and V_0 are the final volume and original volume, respectively. For many materials, α_V and the heat capacity C_V have a similar temperature dependence, as predicted by vibration models in solids [37]. This relationship can be expressed by Grüneisen Relationship:

$$\alpha_V(T) = \frac{\gamma B_0 C_V(T)}{V_0} \quad (1.5)$$

where B_0 is the isothermal compressibility and V_0 is molar volume at $T = 0$ K. γ is the Grüneisen parameter. As B_0 and V_0 are always positive, the signs of the Grüneisen parameter and the magnitude of the contribution of the associated vibrational modes to the overall expansion will determine whether a material shows positive or negative thermal expansion.

Thermal expansion of a material can be isotropic or anisotropic. Isotropic materials show the same thermal expansion in all directions. They could be either cubic crystal, if crystalline, or amorphous. Anisotropic materials have different magnitudes of thermal expansion along different axes, and this can cause microscopic cracks when an anisotropic material is heated or cooled. This in turn will lower the mechanical strength of the material. Therefore, isotropic materials with low or near zero CTE are very important for applications. Understanding and controlling the thermal expansion of materials is needed for a wide variety of applications in cookware, electronic devices, engine components, high performance optical mirror substrates, etc. In addition to the usual materials with positive CTEs, some other materials exhibit thermal contraction, or negative thermal expansion (NTE), and decrease in volume when subjected to a positive temperature change. In these materials, the value of the CTE is negative in at least one direction and in some of those materials, the CTE is isotropically negative. The use of NTE materials in composites could in principle allow the design of materials with a specific expansion coefficient over some particular temperature range.

The earliest observation of negative thermal expansion was probably in water, which has its highest density at around 4°C and therefore displays NTE between 0 and 4°C. The recent study of NTE materials has been ongoing for roughly twenty years. The study of oxide NTE materials has focused mainly on materials that fall into the following five big families: AM_2O_7 [38–41], AM_2O_8 [42–45], $A_2M_3O_{12}$ [46–49], AO_2 networks or framework silicates/zeolites [50–54] and AMO_5 [55,56] networks. There are some general structural features that can be associated with these compounds, which include 1) strongly bonded polyhedra/octahedra linked in three dimensions, 2) open and flexible structures, and 3) ferromagnetic or ferroelectric microdomains. Thus the linkages and rotations of the polyhedral/octahedral network is likely to accommodate transverse vibrational modes, which can lead to a significant negative contribution to the thermal expansion if the Grüneisen parameters are large enough [57].

A general case which can give rise to linear NTE in oxide structures is oxygen vibrations [58]. If we consider a simple M-O-M bond in Fig. 1.4, the shape of a typical M-O potential implies that longitudinal oxygen vibrations will in general cause an increase in M-O and, consequently, M-M distances. A transverse vibration in which individual M-O bond distances are unchanged, however, can lead to a reduction in M-M distance; the greater the mean square displacement of the O atom the greater the effective reduction in M-M distance. This phenomenon can be generalized to two and three dimensions, which is associated with transverse vibrations of individual M-O-M linkages of corner sharing polyhedra/octahedra (Fig. 1.5). ZrW_2O_8 is a good example of this type of NTE oxide. The Zr-O-W bridging oxygen groups (Fig. 1.5) are the source of the negative thermal expansion in this material. A systematic change in

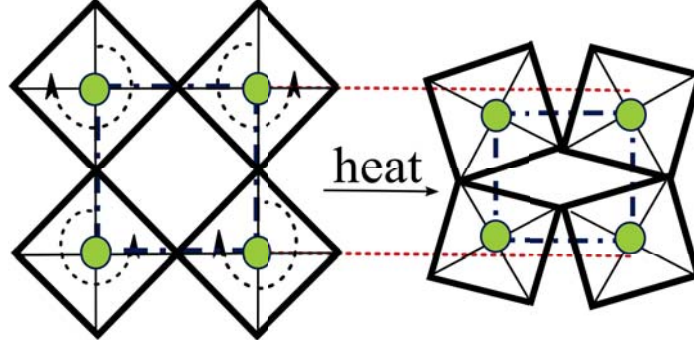


Figure 1.4: A schematic representation of how transverse thermal vibrations of M-O-M bonds can give rise to linear NTE in oxide structures.

these bond angles, corresponding to a coupled twisting of polyhedra could give rise to the volume NTE observable by X-ray diffraction [42]. For a more sophisticated understanding of this mechanism, a rigid unit mode (RUM) can be expressed as following: The WO_4 tetrahedra and ZrO_6 octahedra are considered to be rigid on the relative energy scale of all other deformations of the ZrW_2O_8 structure. Then in a dynamic situation the tetrahedra/octahedra will undergo continuous rotary oscillation backwards and forwards due to the propagating RUM phonons, with no distortions of the tetrahedra/octahedra themselves, thereby resulting in NTE [43, 59].

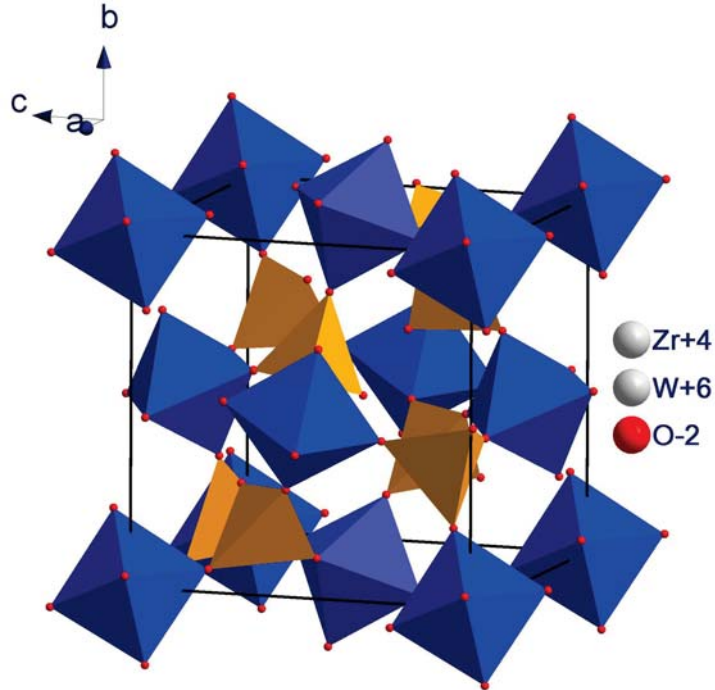


Figure 1.5: Crystal structure of single crystal ZrW_2O_8 . ZrO_6 octahedra shown in blue, WO_4 tetrahedra shown in orange.

Materials with negative and zero (or Invar effect) thermal expansion are clearly of fundamental interest and technological importance for applications such as metrology, chronometry, precision optics and cryogenic storages.

1.4 Outline of the Thesis

The outline of the dissertation is as following:

Chapter 1 presented a brief introduction to transition metal oxides, Ruddlesden-Popper series, negative thermal expansion and our motivation for studying the doped Ca_2RuO_4 system.

Chapter 2 presents the theoretical background and concepts closely related to the study in this thesis, such as crystal structure analysis, magnetism, spin-orbit coupling, Mott transition and metal-insulator transition. This chapter should prepare the reader for the subsequent discussion of real measurement results and different physical properties of studied compounds.

Chapter 3 details the experimental procedures and techniques available in our lab and used in this work. For single crystal synthesis we use both flux and floating zone techniques. The synthesis of high quality single crystal is then followed by sample characterization techniques such as Energy Dispersive X-ray and X-ray diffraction. Then physical property measurements such as magnetic, thermal and transport properties for data presented in this thesis are also described.

Chapter 4 presents the result and discussion for the structural and physical properties measurements for Ca_2RuO_4 , $\text{Ca}_2\text{Ru}_{1-x}\text{Cr}_x\text{O}_4$, $\text{Ca}_2\text{Ru}_{1-x}\text{Mn}_x\text{O}_4$, $\text{Ca}_2\text{Ru}_{1-x}\text{Fe}_x\text{O}_4$ and other $\text{Ca}_2\text{Ru}_{1-x}\text{M}_x\text{O}_4$ with the focus on the correlations of structure change and physical properties in this system.

Chapter 5 presents the conclusions and summary of the physical phenomenon observed in chapter 4 with suggested outlines for additional follow-up research.

Chapter 2 Theoretical Background

2.1 Crystal Structure and X-ray crystallography

2.1.1 Bragg's Law and X-ray Diffraction

A single crystal's structure and symmetry play a major role in determining many of its physical properties, therefore characterization of the crystal symmetry and knowledge of the crystal structure provides a fundamental foundation for studying physical and chemical properties of materials [60–64].

The key feature of structure in a periodic crystal is that the constituent units (atoms, molecules, or ions) are arranged with periodic order. This character can be conveniently investigated by diffraction methods. Diffraction occurs as waves interact with the regular structure whose repeat distance is similar to the wavelength. X-rays have wavelengths on the order of several angstroms, similar to the typical interatomic distances in crystalline solids, which means X-ray can be diffracted from crystals and is a good probe of crystal structure. X-ray powder diffraction is the most commonly used tool for routine structural characterization and comparison of TMO materials. The samples for powder diffraction may be large crystals, or a powder composed of micro-crystals that are too small to be seen. Single crystal X-ray diffraction is generally used to determine the structures of new materials. Compared with powder diffraction, single crystal diffraction can measure much smaller samples, larger molecules and unit cells, has less absorption problem and can uniquely characterize non-standard scattering, e.g., superlattice and satellite peaks (commensurate and incommensurate) [65–67], diffuse scattering (rods, planes, etc.) [68, 69]. However, the technique is limited by the ability to grow high quality crystals that are suitable for diffraction, which has limited its application for routine structural characterization. The underlying principles of the experiments are the same in both powder diffraction and single crystal diffraction.

Fig. 2.1 shows two X-ray beams incident on a family of parallel atomic planes of a crystal separated by the distance d . The rays of the incident beam are always in phase and parallel up to the point at which the top beam strikes the top layer and the second beam continues to the next layer where it is scattered by a next-layer atom. If the two beams are to continue traveling adjacent and parallel, the extra distance the second beam traveled must be an integral number of wavelengths for the phases of the two beams to be the same. Application of trigonometry to reflection geometry allows for the derivation of *Bragg's Law*:

$$n\lambda = 2d\sin(\theta) \quad (2.1)$$

This equation was first derived by the Anglo-Australian physicists Sir W.H. Bragg and his son Sir W.L. Bragg in 1913 to explain why the cleavage faces of crystals appear to reflect X-ray beams at certain angles of incidence [70, 71]. Here d is the

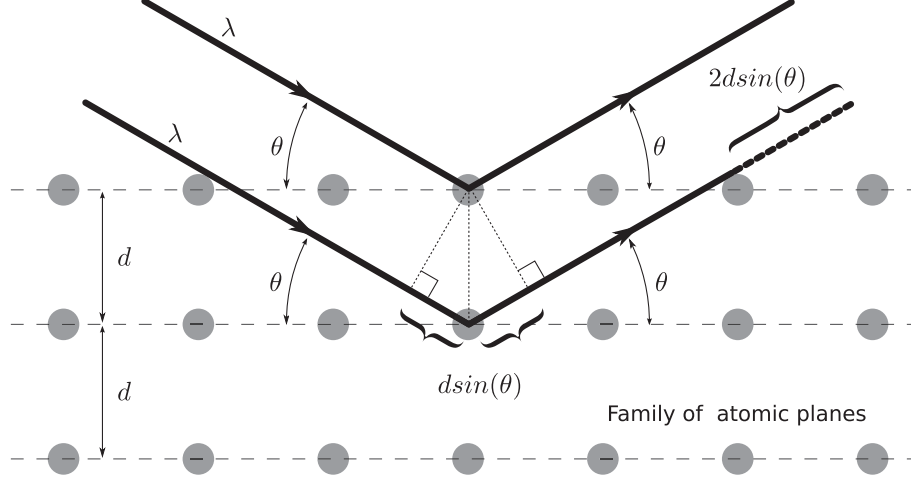


Figure 2.1: Illustration of the fulfillment of the Bragg's equation.

distance between atomic layers, λ is the wavelength of the incident X-ray, θ is the incidence angle (Bragg's angle) and n is an integer.

X-rays are electromagnetic radiation, so we can study the electric and magnetic components of X-rays, named X-ray photons [72, 73]. In a scattering process, most of the scattered photons are emitted at the same energy as the energy of the incident photons, this process is called coherent (or Rayleigh) scattering [74–76]. Some photons are emitted at lower energies, this is named incoherent scattering or Compton scattering. The intensity of coherent scattering can be expressed as below, which was first derived by John William Strutt (Lord Rayleigh) [77]:

$$I(2\theta) = I_0 \cdot \frac{ne^4}{2r^2m^2c^4} \cdot \frac{1 + \cos^2(2\theta)}{2} \quad (2.2)$$

Here I_0 is the intensity of a non-polarized incident beam, e is the electron charge, c is the speed of light, n is the number of scattering sources, m is the mass of scattering source, r is the distance from the sample to the detector and 2θ is the angle between the incident and scattered photon. According to this formula, the scattered intensity is inversely proportional to the square of the mass of the particle emitting the X-ray photon, then the scattering from the nucleus is considered smaller and negligible compared to the scattering from the electrons. Thus, X-ray scattering is considered to be due to the electrons, and thereby provides a probe of the *electron density of the atoms* in the crystal [75, 78, 79].

2.1.2 Crystal and Reciprocal Lattice

Crystals often have well-defined smooth flat faces and straight edges; between similar faces of different samples of a crystalline substance, the angles are always constant; some crystals easily cleave along well-defined faces. All these properties led to an assumption that crystals are made of many tiny identical pieces that are stacked in a 3-dimensional array related by simple translation. In crystallography, periodic

crystals are defined as solids with long range 3-dimensional internal order, and each unique piece of the 3-dimensional array is called a unit cell [80]. In two dimensions, the size and orientation of the axes in a unit cell can be characterized by two translation vectors a and b and the angle γ between them (see Fig. 2.2 (a)). If we extend the description to three dimensions, the unit cell is delimited by three pairs of parallel planes, and thus is defined by six parameters, namely three axial lengths a , b and c and the three inter-axial angles α , β and γ . As shown in Fig. 2.2 (b), the angle α is the angle between b and c ; β is the angle between a and c ; and γ is the angle between a and b . By convention the unit cell axes are chosen so as to form a right-handed rectilinear coordinate system, to have the highest symmetry and smallest volume.

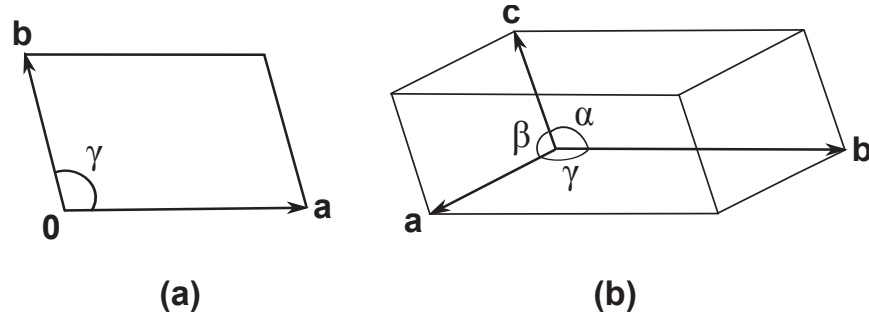


Figure 2.2: Illustration of a unit cell in (a) 2-dimensions and (b) 3-dimensions showing cell parameters.

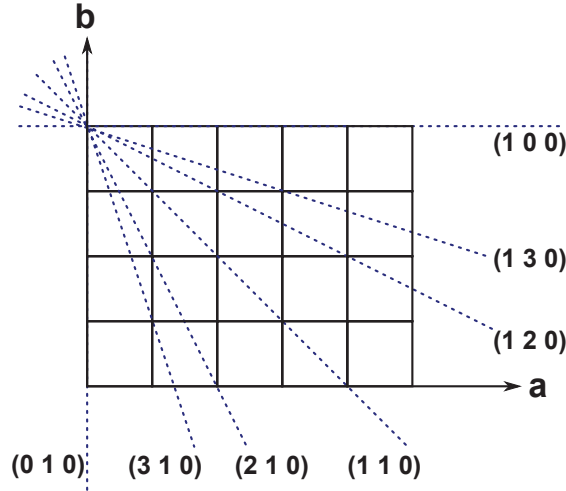


Figure 2.3: Illustration of various planes and their (hkl) identification in a 2-dimensional lattice. One square block represents a unit cell; Blue dotted lines are sets of atomic planes.

The sets of parallel atomic planes that reflect X-ray beams can be chosen in different ways (see Fig. 2.3). However, these planes must intersect all of the ions

in a lattice, then the intercepts of the planes with the cell edges must be fractions of the cell edge. Thus cell intercepts can be at $1/0 (= \infty)$, $1/1$, $1/2$, $1/3 \dots 1/n$. The conventional way of describe the orientation of these families of plane is with a *Miller Index* of the form (hkl) in which the plane makes the intercepts with a unit cell of a/h , b/k and c/l (h , k and l are three integers), as shown in Fig. 2.3. The Miller index indicates the reciprocal of the intercepts. For example, a set of planes intercept at $1/1$ in a , $1/2$ in b , and $1/3$ in c , then the planes would be referred to as the $(1\ 2\ 3)$ set of planes in Miller index. The orientation of planes can also be represented by a vector normal to the plane. The direction of the vector denoted by square brackets containing the Miller indices of the set of planes. For example, $[1\ 0\ 0]$ vector is normal to $(1\ 0\ 0)$ planes.

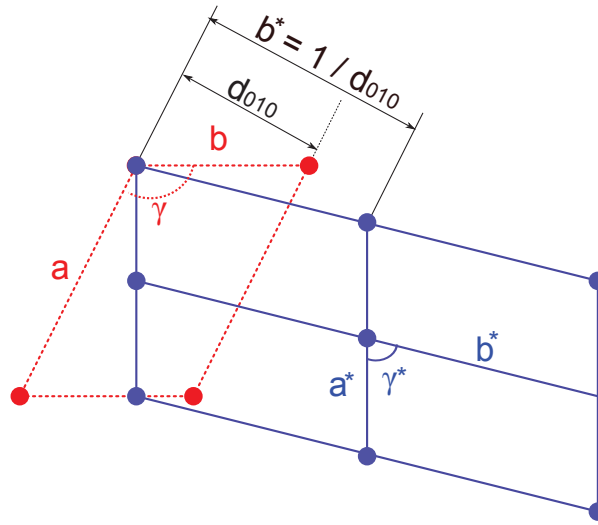


Figure 2.4: Illustration of real (in red) and reciprocal (in blue) lattices.

The scattered photon produces a resulting diffraction pattern. Because of the reciprocal nature of d spacings and θ from Bragg's Law, the observed diffraction pattern can be related to the crystal lattice by a mathematical construct called the *reciprocal lattice* [81]. Fig. 2.4 shows the relation between a real lattice and reciprocal lattice. One way to conceptually construct the diffracted lattice pattern is as following: First, choose a point in the crystal lattice to be the common origin. Then consider normals to all possible direct lattice planes (hkl) to radiate from this origin. Terminate each normal at a point that is a distance $1/d_{hkl}$ from this origin, where d_{hkl} is the perpendicular distance between planes of the plane set (hkl) , as shown in Fig. 2.4. Repeat these steps for all real lattice planes, then the set of points so determined constitutes the reciprocal lattice. Note that a short axis in real space corresponds to a large separation between points in reciprocal space, and obtuse angles in the real unit cell lead to acute angles in the reciprocal cell [81]. We can then define reciprocal lattice vectors a^* , b^* , and c^* (see Fig. 2.4), which have following relations with real

cell vectors a , b , and c :

$$\begin{aligned} a^* \cdot b &= a^* \cdot c = b^* \cdot a = b^* \cdot c = c^* \cdot a = c^* \cdot b = 0 \\ a^* \cdot a &= b^* \cdot b = c^* \cdot c = 1 \end{aligned} \quad (2.3)$$

The first set of equations above state that a^* is perpendicular to the bc plane, b^* is perpendicular to the ac plane, and c^* is perpendicular to the ab plane. The following set of equations can give length and direction of the reciprocal lattice vectors, from which the definition of individual lattice vectors can be derived [81]:

$$\begin{aligned} a^* &= 2\pi \frac{b \times c}{a \cdot b \times c}; \quad b^* = 2\pi \frac{c \times a}{a \cdot b \times c}; \quad c^* = 2\pi \frac{a \times b}{a \cdot b \times c}; \\ V &= a \cdot b \times c = b \cdot c \times a = c \cdot a \times b. \end{aligned} \quad (2.4)$$

Here " \times " denotes the cross product between two vectors and V is the volume of the unit cell in real space. An interesting property of the reciprocal lattice vector is that the relations are still valid if we replace real lattice vectors by reciprocal lattice vectors and inversely reciprocal lattice vectors by lattice vectors. Thus it is straight forward to convert between real and reciprocal space. The reciprocal vectors play an important role in diffraction and structure determination.

2.1.3 Structure Factors and Structure Refinement

Let the electron density at a position \vec{r} from the center of an atom be $\rho(\vec{r})$. Consider the X-ray scattered at the position \vec{r} in a direction \vec{s} relative to the incident beam of radiation in the direction \vec{s}_0 . The scattered intensity depends on the phase difference δ , which is $2\pi/\lambda$ times the path length difference:

$$\delta = \frac{2\pi}{\lambda} [\vec{r} \cdot (\vec{s} - \vec{s}_0)] = 2\pi \vec{r} \cdot \vec{S} \quad (2.5)$$

where $\vec{S} = (\vec{s} - \vec{s}_0) / \lambda$. The vector \vec{S} is called the *scattering vector*, which is a vector in reciprocal space that is normal to the plane defined by (hkl) . The wave scattered by the volume element $d\nu$ at \vec{r} will have an amplitude with a maximum of $\rho(\vec{r})d\nu$. Combining this with the phase factor then the amplitude of the wave at \vec{r} can be expressed as $\rho(\vec{r}) e^{2\pi i \vec{r} \cdot \vec{S}} d\nu$. The total scattering power of the atom is given by integrating over all volume elements $d\nu$ of the atom:

$$f_0 = \int \rho(\vec{r}) e^{2\pi i \vec{r} \cdot \vec{S}} d\nu \quad (2.6)$$

This expression represents the *atomic scattering factor*. Then we assume this atom in a unit cell of a crystal is located at \vec{r}_j from the coordinate origin. This shift in

origin from the center of the individual atom makes the distance \vec{r} in the previous equation becomes $\vec{r} + \vec{r}_j$. Thus the scattering by atom j becomes:

$$\vec{f}_j = \int \rho(\vec{r}) e^{2\pi i(\vec{r} + \vec{r}_j) \cdot \vec{S}} d\nu = f_0 \cdot e^{2\pi i \vec{r}_j \cdot \vec{S}} \quad (2.7)$$

where $f_0 = \int \rho(\vec{r}) e^{2\pi i \vec{r} \cdot \vec{S}} d\nu$

Similar expressions can be derived for all of the other atoms in the unit cell. The total scattering power of all of the atoms is given by the sum of the individual scattering amplitudes:

$$\vec{F}(\vec{S}) = \sum \vec{f}_j = \sum f_0 \cdot e^{2\pi i \vec{r}_j \cdot \vec{S}} \quad (2.8)$$

The scattering vector \vec{S} satisfies the *Laue equations*, which are analogous to a 3-dimensional representation of Bragg's Law:

$$\begin{aligned} (2\pi/\lambda)(\vec{a} \cdot \vec{S}) &= 2\pi h/\lambda \\ (2\pi/\lambda)(\vec{b} \cdot \vec{S}) &= 2\pi k/\lambda \\ (2\pi/\lambda)(\vec{c} \cdot \vec{S}) &= 2\pi l/\lambda \end{aligned} \quad (2.9)$$

Since for the jth atom, its coordinate is labeled x_j , y_j , and z_j . Then the \vec{r}_j vector can be written as:

$$\vec{r}_j = \vec{a} x_j + \vec{b} y_j + \vec{c} z_j. \quad (2.10)$$

Thus the product $\vec{r}_j \cdot \vec{S}$ can be written as:

$$\begin{aligned} \vec{r}_j \cdot \vec{S} &= \vec{a} x_j \cdot \vec{S} + \vec{b} y_j \cdot \vec{S} + \vec{c} z_j \cdot \vec{S} \\ &= hx_j + ky_j + lz_j. \end{aligned} \quad (2.11)$$

So the final expression of the total scattering power for all of the atoms in the unit cell can be written as:

$$\vec{F}(hkl) = \int f_0 \cdot e^{2\pi i(hx_j + ky_j + lz_j)} \quad (2.12)$$

Here the exponential part is the phase angle of the individual atom diffraction. The ideal picture of Bragg's Law in Fig. 2.1 oversimplifies the real situation, in which the electron densities in the unit cell are not concentrated in parallel planes. A more realistic depiction would have atoms dispersed at various locations in between these planes. Then the expression above can be considered as a correction to the phase angle necessitated by the atom being "out of" the Bragg plane. The quantities x_j , y_j , z_j are the atom fractional coordinates along the a, b and c unit cell axes, respectively.

To get an expression for the electron density of the unit cell, we need to do a reverse Fourier Transform of $\vec{F}(hkl)$. And since $\vec{F}(hkl)$ is nonzero only at the lattice

points, the integral may be written as discrete sums over the three indices h, k, and l, where in real space the three summations run over all values of x, y, and z:

$$\begin{aligned}\rho(xyz) &= \frac{1}{V} \sum_h \sum_k \sum_l \vec{F}(hkl) \cdot e^{-2\pi i(hx+ky+lz)} \\ &= \frac{1}{V} \sum_h \sum_k \sum_l |F|(hkl) \cdot e^{-2\pi i[hx+ky+lz-\varphi(hkl)]}\end{aligned}\tag{2.13}$$

Here $|F|(hkl)$ is the amplitude of $\vec{F}(hkl)$ and $\varphi(hkl)$ is its phase angle, also called *Intrinsic Phase* angle. Since we don't have any information about the relative phases, we cannot directly calculate electron density. There are several ways to solve this so-called "phase problem". The two most commonly encountered in small moiety crystallography are: Patterson Methods and Direct Methods. Patterson Methods extract information on interatomic vectors by using an analogous equation to 2.13, but using unphased intensities $I(hkl)$ rather than structure factors, while Direct Methods use statistical methods that rely on a few physically reasonable assumptions of electron density distributions. When supplied with appropriate phases, Eq.2.13 enables the calculation of a three dimensional electron density map throughout the unit cell, and is therefore a very important equation in x-ray crystallography. The peaks in the electron density map define the locations of individual atoms, and this allows the building of a structure model. Since the calculation of electron density is a Fourier transform, the back transform allows calculation of structure factors for the model. Comparison of observed and calculated structure factors allows the model to be fine-tuned, so as to minimize the difference.

Structure refinement is actually a series of steps trying to adjust the various atomic parameters so that the calculated structure factors match the observed structure factors as closely as possible. One of the ways to measure the agreement between them is with the *R-factor*. The most used two R-factors are:

$$R_1 = \frac{\sum ||F_o| - |F_c||}{\sum |F_o|} \quad \text{and} \quad R_\sigma = \frac{\sum \sigma |F_o|}{\sum |F_o|}\tag{2.14}$$

Here F implies $F(hkl)$, F_o means observed F value, F_c means calculated F value and σ is the appropriate standard deviation. In general, the lower these R values are, the better the correspondence of the structure model to reality. Other agreement factors used in crystallography include the R_{int} value, which provides a measure of the consistency of intensity measurements for symmetry related (hkl) values and multiple measurements of the same (hkl) values. Similarly, the R_σ values tell us about the accuracy of the data and the data reduction process. Since diffracted intensities are generally weaker for higher resolution reflections, it is often useful to use the variation of R_{int} and R_σ as a function of resolution to get some idea of data quality. If either of these values is much greater than around 0.1 (10%) for the whole dataset, then the data might not be suitable for refinement and solution. In the very highest resolution shells, values of around 0.3(30%) are often used to define the "resolution" of the resulting structure.

2.2 Metal-Insulator Transition

2.2.1 Metals and Insulators

The first successful theoretical distinction between metals and insulators, together with the transitions between them is based on noninteracting electron systems. The definition based on the filling of the electronic bands: For insulators the highest filled band is completely filled; for metals, it is partially filled [82, 83]. For metals, the Fermi level lies inside a band, whereas for insulators it lies in a band gap. In this picture insulators can be generally classified into main types. In a *Band insulator* (or Bloch-Wilson insulator), the electrons interact with the ions and the electron can be defined by an effective single particle Hamiltonian in the periodic potential of the ion [84–86]. For a *Peierls insulator*, the electron-ion interaction produces a lattice distortion that changes the periodicity of the crystal which in turn affects the electron transport [86–88]. In *Anderson insulators*, the insulating behavior is produced by the interaction of independent electron with random lattice defects [86, 89, 90]. All these three types of insulating behavior can be understood on the basis of interaction of single electrons with the electrostatic field of the ions in the crystal [86]. This band picture was very successful in many respects, however, it was found later that many TMOs with a partially filled d-electron band were nonetheless poor conductors or insulators [82, 91, 92]. Then the importance of the electron-electron correlation (strong coulomb repulsion between electrons) was first recognized [92], followed by a long and continuing history of the developing field of strongly correlated electrons. This generates the other main types of insulators: the *Slater insulator* and *Mott insulator*, in which band theory and hence the independent electron assumption fails. The Slater insulator, in close analogy to the Peierls insulator, is related to a periodic modulation of the spatial charge and/or spin distribution which in this case is generated by the electron-electron interaction instead of the electron-lattice interaction [93]. In an antiferromagnetic (AFM) Slater insulator, every neighboring spin is oppositely aligned (AFM order) below a transition temperature from metal to insulator, creating an opposite periodic potential on each nearest neighbor, which leads to an insulating ground state. Different from the Slater insulator, Mott insulator emphasizes the existence of moments but not on whether or not they are ordered [82, 93], although later Mott also considered the importance of magnetically ordered state [94]. Mott insulators are characterized by correlated many-electron phenomenon and coulomb interaction between the charge carriers [82, 86, 92].

One of the simple and successful models to describe these strongly correlated electrons can be addressed from the competition between interaction energy (U) and the kinetic energy of electrons (W) [95]. The electron hopping process (the kinetic energy term) likes to delocalize the electrons into Bloch states and thus metallic behavior. The correlated electron-electron interaction tends to delocalize the electrons into their own atomic states thus making it insulating. The local density of states (DOS) depends on the ratio of them, as shown in Fig.2.5. In this situation band theory concepts are not sufficient and ideas such as Hubbard bands and narrow coherent quasi-particle bands are needed for the description of the electronic structure. In a

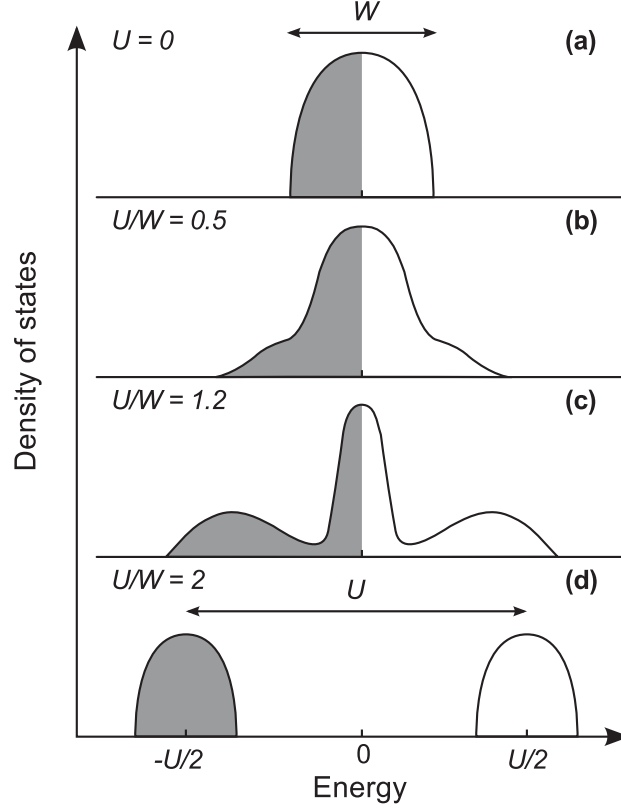


Figure 2.5: Density of states as a function of band energy for electrons that are (a) independent (b) nearly independent (weakly correlated) (c) strongly correlated and (d) localized.

pure metal, electrons are completely independent with no interaction energy ($U=0$), as shown in Fig. 2.5(a). The DOS takes up a shape of a half ellipse with Fermi level E_F being located in the middle of the band. In the opposite condition, when U is sufficiently stronger than W , the electron system is localized and the DOS peaks at the ionization energy (see Fig. 2.5(d)). In between of these two well-established limits, both elementary band theory and localized electron theory are failed. In a weakly correlated case shown in Fig. 2.5(b), electrons can be described as quasi-particles with DOS resembling free electrons. In a strongly correlated material (see Fig. 2.5(c)), the spectrum constructs of quasi-particle peak near E_F and Hubbard bands broadened by the hopping of electrons away from the atom [95].

The efforts of related experimental study were particularly emphasized on understanding how an insulator could become a metal as controllable parameters were varied [82]. This transition from metal to insulator is called *Metal-Insulator Transition* (MIT). MITs are accompanied with huge resistivity changes, even over many orders of magnitude, and are widely observed in condensed-matter systems [82,83,94].

2.2.2 Mott-Hubbard Transition

Mott took the first several important steps to understand how electron-electron correlations could be related to the insulating state, and we call this insulating state the Mott insulator [82, 94, 96, 97]. First, Mott considered a lattice model with a single electronic orbital on each site. Without electron-electron interactions, a single band is filled with two electrons, one with spin-up and the other with spin-down. However, two electrons sitting on the same site would have a large Coulomb repulsion, which would then split the band in two. Then with one electron per site, the system is an insulator [82]. Mott then described a metal-insulator transition by imagining a crystalline array of hydrogen-like atoms on a d -dimensional cubic lattice with a lattice constant \mathbf{a} that could be varied. The electron density $n = N/L$ where N is the total number of electrons and L is the number of lattice sites. For half-filled bands $n = 1$. We assume that the effective electron-electron interaction will be local, which has the electrons dominantly sit on and not between the lattice sites. A further assumption is that electrons may hop between neighboring atoms. For large values of \mathbf{a} as $\mathbf{a} \gg \mathbf{a}_0$ (\mathbf{a}_0 is Bohr radius), the overlap between atomic orbitals is small, the material would be insulating (like in nickel oxide); while for small \mathbf{a} values, a single half-filled band makes the system a paramagnetic metal (like in monovalent metal sodium) [94]. Then a transition from insulator to metal is expected in an intermediate condition where the intra-atomic energy and bandwidth are comparable.

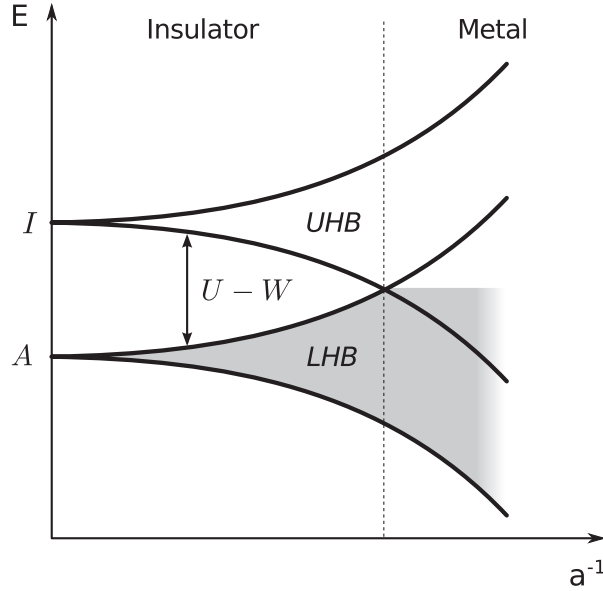


Figure 2.6: Illustration of the upper and lower Hubbard bands in Mott insulator as a function of reciprocal interatomic distance. Here U ($U = I - A$) is the intra-atomic energy and W is the bandwidth.

Fig. 2.6 shows the two bands, which we call the lower and upper Hubbard bands. We can clearly see as the bandwidth W increases the gap $U - W$ decreases until the bands overlap and material becomes a metal [98]. This illustration about Hubbard

bands provides a direct explanation for Mott metal insulator transitions. For $U \gg W$ the bands are separated with a gap, which makes it an insulator. At a critical value $U = W$ the bands come closer and touch each other. When $U \ll W$ the band overlap and there is a finite density of states at Fermi level and hence the system has metallic behavior. The MIT then appears as a band-crossing transition, from AFM metal to AFM insulator or from AFM metal to normal metal [94]. Mott-Hubbard transition doesn't consider ordering of moments. By calculating the AFM coupling between spin 1/2 electrons on neighboring lattice sites using second order perturbation theory, we can include long range ordering of magnetic moments, which is called a *Mott-Heisenberg transition*. When we lower the temperature, local magnetic moments in the Hubbard insulator may go through a long range order around Neel temperature. Thus the system undergoes a phase transition from Mott-Hubbard insulator into the antiferromagnetic Mott-Heisenberg insulator [86, 99]. For a metallic state, it may undergoes a phase transition from paramagnetic metallic state to AFM Mott-Heisenberg insulating state at the transition temperature [86, 99].

2.2.3 Disorder Induced Metal-Insulator Transitions

When perfect crystalline symmetry is broken by introduction of impurities, existence of disorder may cause electrons to be localized. For disordered systems, then, this kind of quite different form of metal-insulator transition is called the *Anderson transition* [100] or disorder induced transition. Two majors conditions of Anderson transition are: First, we suspect that transport occurs by quantum-mechanical jumps of the mobile entities from site to site instead of motion of free charge carriers. Second common feature of this phenomena is random spacings of impurities and random arrangements of electronic spins [100]. In these systems a range of energies exists in which the electron states are localized, and if at zero temperature the Fermi energy lies in this range then the material will not conduct, even though the density of states is not zero. The Anderson transition can be discussed in terms of non-interacting electrons, though in real systems electron-electron interaction plays an important part. [94, 100]

When a system becomes disordered, localized states first appear in the band tails, while the states in the band center remain extended, as shown in Fig. 2.7. There exist two limiting energies E_c and E'_c , suggested by Mott [101], called the mobility edges, which separate extended states from localized states [100–102]. As the strength of the disorder increases, more states become localized, and the two mobility edges approach each other and finally merge at some critical disorder strength, beyond which no extended states exist in the band. Fig. 2.7 shows the two mobility edges and Fermi level E_F , where (a) and (b) shows metallic and insulating state, respectively. They have the same Fermi level E_F , i.e., the electronic density is the same. However, in Fig. 2.7(a) E_F lies in the center of band, make the system a metal, whereas in Fig. 2.7(b) the states are localized around E_F , cause a insulter. With the increase of the disorder strength, the lower mobility edge E_c will move towards and finally cross the Fermi level E_F . During this process, the system will make a transition from metallic (Fig. 2.7(a)) to insulating (Fig. 2.7(b)) state [100–102], which is the so-called Anderson

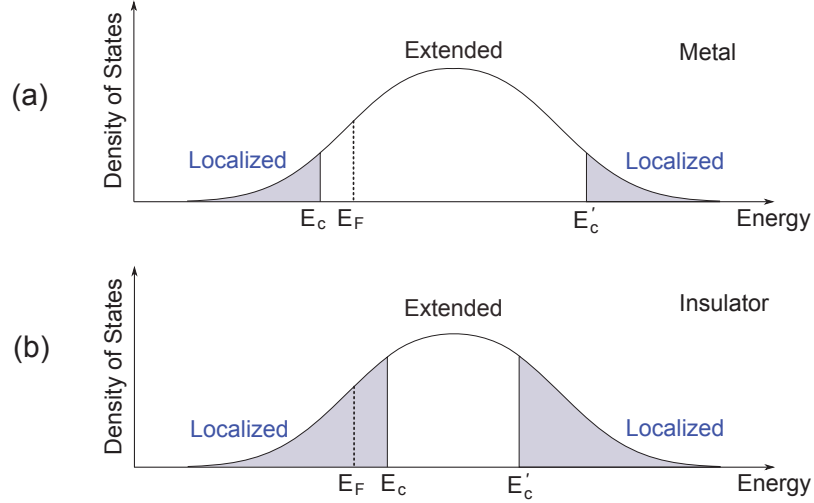


Figure 2.7: Schematic pictures of the density of states in a disordered system. E_c and E'_c represent the mobility edges, that separate the localized states in the band tails (shaded areas) from the extended states in the band center.

Metal-Insulator Transition.

2.3 Magnetism

Magnetism has been studied for nearly three thousand years [103]. During the Qin dynasty (221-206 B.C.) or even earlier, the magnetic compass was already made in China, which is the first technological product resulting from magnetic study [104, 105]. Much more progress has been made since the discovery and application of electromagnetic waves. In condensed matter physics, magnetism is a powerful tool to study the basic constituents of magnetic systems including ferromagnets, spin glasses and low dimensional systems. Nowadays the interest of fundamental research, in company with the technological drive to find new materials, makes more powerful and useful permanent magnets, sensors, storage and memory facilities [103, 106–109].

The main feature of magnetism in 4d TMOs is the more extended d-orbitals compared with those of the 3d ions [35]. This leads to comparable and thus competing energies, mainly due to the more pronounced orbital degree of freedom. The energies due to crystalline field, Hund's rule interactions, spin-orbit coupling, p-d electron hybridization and electron-lattice coupling are comparable, which makes the system highly sensitive to external perturbations. In a Ru^{4+} ($4d^4$) ion, the crystalline field can overcome the Hund's rule coupling, yielding a low spin state with $S = 1$ rather than an expected high spin state with $S = 2$ for free ions. The significance of crystalline field splitting and the other competing energies will be discussed in detail.

2.3.1 Hund's Rules

Hund's rules are used to determine the electronic configuration that corresponds to the ground state of a multi-electron atom. Hund's rules works pretty well except when the electrons become relativistic in heavy atoms and spin-orbit effects become comparable to the electron repulsion. A set of principles called the three Hund's rules can be stated as below [110, 111]:

1. For a given electron configuration, the term with maximum spin S has the lowest energy.
2. For a given multiplicity, the term with the largest value of the orbital angular momentum L has the lowest energy.
3. For a given term, in an atom with outermost subshell half-filled or less, the level with the lowest value of the total angular momentum quantum number ($J = |L - S|$) lies lowest in energy. If the outermost shell is more than half-filled, the level with the highest value of the total angular momentum ($J = L + S$) is lowest in energy.

Here L and S are the total orbital and total spin angular momentums. The first Hund's rule "maximum spin" can be understood from the Pauli exclusion principle: electrons with parallel spins must be in different orbitals, which overall implies larger separations, hence lower energies. The second rule deals with reducing the repulsion between electrons. It can be understood from the classical picture that if all electrons are orbiting in the same direction (higher orbital angular momentum) they meet less often than if some of them orbit in opposite directions. In the latter case the repulsive force increases, hence separates electrons, which adds potential energy and make their energy level higher. The third rule specifies the way in which spin and orbital moments are coupled with each other. It is an attempt to minimize the spin-orbit energy and is only applicable when it is significantly higher than other energies.

2.3.2 Spin Orbit Coupling

Spin-orbit coupling (SOC) is a well-known phenomenon that could lift the degeneracy of one-electron energy levels in atoms, molecules, and solids. The interaction between the electron spin and the orbital angular momentum can be described by the spin-orbit Hamiltonian defined as follows:

$$\hat{H}_{SO} = \frac{1}{2m_e c^2} \frac{1}{r} \left(\frac{\partial V}{\partial r} \right) \hat{L} \cdot \hat{S} = \xi \hat{L} \cdot \hat{S} \quad (2.15)$$

Here V is the columbic potential of the electron in the field of the atom. Note that the spin-orbit interaction is proportional to $\hat{L} \cdot \hat{S}$. In order to compute the spin-orbit Hamiltonian of a many-electron atom, it is necessary to compute first an approximate

effective potential V_i of each electron i in the total electric field of electrons and nuclear charges. Then, we can calculate the sum over all electrons as follows:

$$\hat{H}_{SO} \approx \frac{1}{2m_e c^2} \sum_i \frac{1}{r_i} \frac{\partial V_i}{\partial r_i} \hat{L}_i \cdot \hat{S}_i = \sum_i \xi_i \hat{L}_i \cdot \hat{S}_i \quad (2.16)$$

The correction of eigenfunctions and eigenvalues, due to the spin-orbit coupling, is usually calculated according to perturbation theory after solving the atomic eigenvalue problem in the absence of the spin-orbit interaction. For example, the spin-orbit correction to the eigenvalue of state $|\Psi\rangle$ for a one-electron atom is,

$$E_{S.O.}^{(1)} \approx \langle \Psi | \xi \hat{L} \cdot \hat{S} | \Psi \rangle \quad (2.17)$$

Note that the $L \cdot S$ product can be written in terms of J^2, L^2 and S^2 as follows, $L \cdot S = \frac{1}{2}(J^2 - L^2 - S^2)$, because, $J^2 = J \cdot J = (L + S)(L + S) = L^2 + S^2 + 2L \cdot S$, and, since the unperturbed wave function is an eigenfunction of L^2, S^2 and J^2 :

$$L \cdot S |\psi\rangle = \frac{1}{2} \hbar^2 (J(J+1) - L(L+1) - S(S+1)) |\psi\rangle \quad (2.18)$$

Therefore,

$$E_{S.O.} \approx \frac{1}{2} \hbar^2 \langle \xi \rangle [J(J+1) - L(L+1) - S(S+1)] \quad (2.19)$$

Note that due to the spin-orbit coupling, the total energy of a state depends on the value of the total angular momentum quantum number J . Furthermore, each of the energy levels is $(2J+1)$ times degenerate, as determined by the possible values of M_J . For example, when $L=1$, and $S=1/2$, then the possible values of J are $1/2$ and $3/2$ ($J=L+S, L+S-1, \dots, L-S$). Therefore, the spin orbit interaction is responsible for splitting of spectroscopic lines in atomic spectra.

The degeneracy of energy levels could be removed by applying an external magnetic field that perturbs the system as follows, $H_B = -m \cdot B$, where $m = m_L + m_S$, with $m_L = -\frac{e}{2m_e} L$, and $m_S = -\frac{e}{m_e} S$. Therefore, the external perturbation can be described by the following Hamiltonian:

$$H_B = -\frac{e}{2m_e} (L + 2S) \cdot B = -\frac{e}{2m_e} (J + S) \cdot B \quad (2.20)$$

The energy correction according to first-order perturbation theory is:

$$E_B = -\frac{e}{2m_e} B (\hbar M_J + \langle S_z \rangle) = A B M_J \quad (2.21)$$

where

$$\langle S_z \rangle = \hbar M_J \frac{J(J+1) - L(L+1) + S(S+1)}{2J(J+1)} \quad (2.22)$$

and A is a proportionality constant. Therefore, the perturbation of an external magnetic field splits energy level characterized by quantum number J into $2J+1$ energy sub-levels, corresponding to different possible values of M_J .

Recently, a SOC driven novel angular momentum state and a giant magnetoelectric effect in Sr_2IrO_4 attracted a lot of attention. In iridates, a strong SOC plays an important role, especially for t_{2g} electrons. The spin-orbit coupling for 5d TMOs is about 0.3-0.4 eV, which is much larger than that of 3d TMOs (20 meV). This makes the SOC in 5d TMOs is comparable to their U values (about 0.5eV), therefore leads to a cooperative interaction. For the layered iridates the SOC can induce a novel $J_{eff} = 1/2$ state [112–115]. These observations emphasizes the importance of this category of materials and provides an indication to a possibility of new physics.

2.3.3 Crystal Field Environment

The crystal field is an electric field derived from the neighboring atoms in the crystal [103]. In *crystal field theory* the bonding between the central metal atom and the ligands is completely ignored and the ligands are viewed simply as point charges. the size and nature of crystal field effects strongly depend on the symmetry of the local environment. We focus on the valence d orbitals of the central transition metal atom and examines how the relative energies of the d orbitals change upon introduction of external negative point charges. Thus, it is necessary to first review the shapes of various d orbitals, as shown in Fig. 2.8.

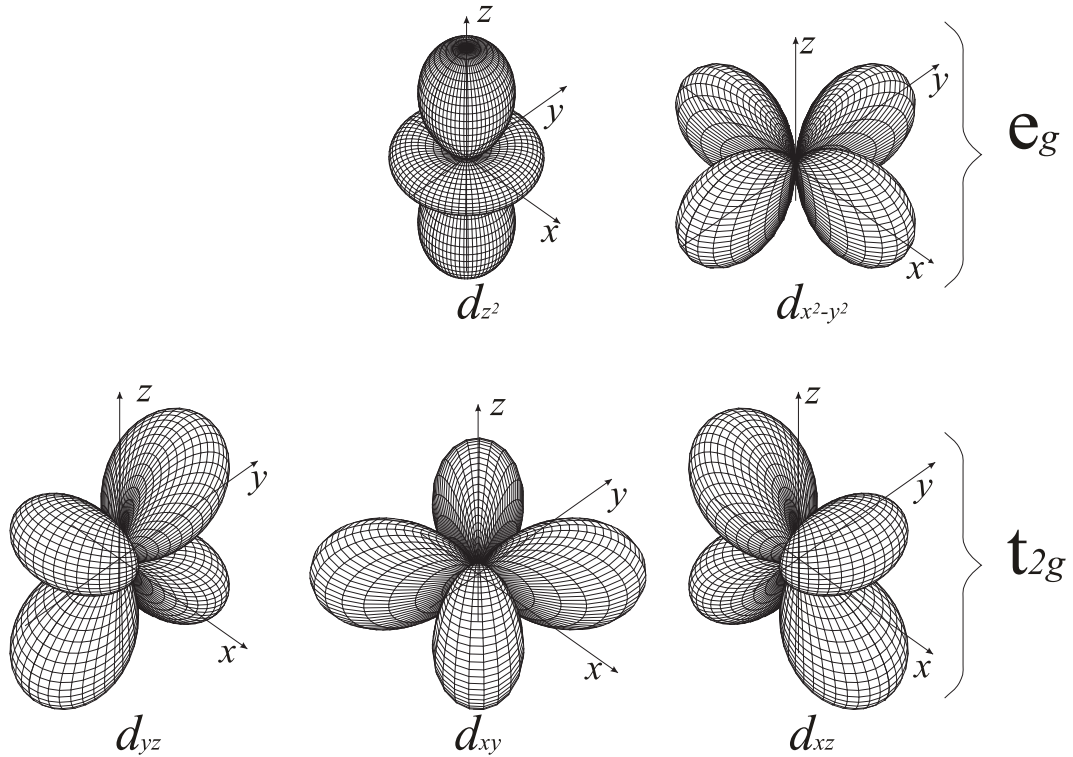


Figure 2.8: Illustration of angular distribution of the d-orbitals. The $d_{x^2-y^2}$ and d_{z^2} orbitals are grouped together and called the e_g levels. The d_{xy} , d_{yz} , and d_{xz} orbitals are grouped together and called the t_{2g} levels.

There are two classes of d orbitals, t_{2g} and e_g [103,116]. t_{2g} orbitals point **between** the x, y and z axes, while the e_g orbitals point **along** these axes. In an ideal transition metal ion only by itself, all of the five d-orbitals have equal energy, but they are at different spatial orientations around the nucleus. Based on the geometric structure of the molecule, when electrons from a ligand approach the metal ion, some follow a more direct line of opposition from the d-orbital electrons than others. Since ligands approach in different directions, different splitting patterns of the d energy level can then be created [103,116].

Crystal field theory was developed by considering different local environments. For example, we can consider a molecule with an octahedral structure, e.g. manganese(II) oxide, MnO; and a tetrahedral structure, e.g. copper(I) chloride, CuCl (see Fig. 2.9).

In the MnO structure, each Mn^{2+} ion is surrounded by six O^{2-} ions arranged on the corners of an octahedron. MnO is therefore a model for an octahedral complex in which a transition metal ion is coordinated to six ligands [117]. O^{2-} approaches the Mn^{2+} ions along the x, y and z axes. The electrons in the $d_{x^2-y^2}$ and d_{z^2} orbitals, which lie along the x, y and z axes feel the most repulsion. Therefore, it takes more energy to have an electron in these orbitals than it would need to put an electron in one of the other orbitals. This causes a splitting in the energy level of the d orbitals as shown in Fig. 2.9. The difference between the energies of these two groups is represented by the symbol Δ_{oct} . The energies of the $d_{x^2-y^2}$ and d_{z^2} orbitals increase from the normal energy of the d orbitals, while the d_{xy} , d_{yz} , and d_{xz} orbitals are lower and become more stable [103,117]. The magnitude of Δ changes from one octahedral complex to another. It depends on the identity of the metal ion, the charge on this ion, and the nature of the ligands coordinated to the metal ion [118–120].

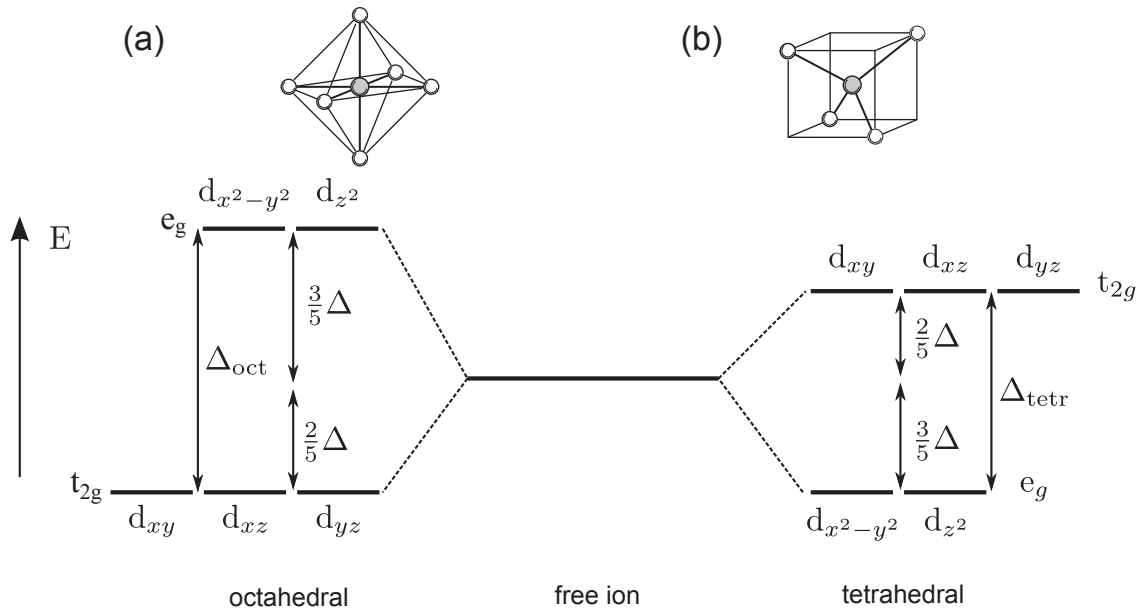


Figure 2.9: Splitting of the electronic d orbitals due to the crystal field in (a) octahedral and (b) tetrahedral environment.

The crystal field in CuCl is a tetrahedral type [121]. In this structure the Cu^+ is inside a cube with its d_{z^2} and $d_{x^2-y^2}$ orbitals pointing at the center of the cube faces. The point charges approach via the four opposite corners of the cube (see Fig. 2.9). The orbitals d_{xy} , d_{yz} , and d_{xz} are pointing towards the center of the cube edges. As a result, the splitting observed in a tetrahedral crystal field is opposite to the splitting in an octahedral complex: the two orbitals in the e_g set are now lower in energy than the three orbitals in the t_{2g} set. The splitting energy Δ_{tet} in a tetrahedral field is smaller than the splitting in an octahedral case because there are fewer ligands involved [103, 118–120]. The size of Δ_{tet} tends to be smaller than the pairing energy, so it usually has high spin state, which usually makes it paramagnetic.

The use of these splitting diagrams can aid in the prediction of the magnetic properties of TMOs. A TMO compound with unpaired electrons in its splitting diagram is usually paramagnetic and will be attracted by magnetic fields, while a compound that lacks unpaired electrons in its splitting diagram will be diamagnetic and will be weakly repelled by a magnetic field [103].

2.3.4 The Jahn-Teller Effect

The *Jahn-Teller effect*, named after Hermann Arthur Jahn and Edward Teller, describes the geometrical distortion of non-linear molecules. It was first published in 1937 and essentially means that: "any non-linear molecular system in a degenerate electronic state will be unstable and will undergo distortion to form a system of lower symmetry and lower energy thereby removing the degeneracy" [122]. Generally, Jahn-Teller effect states that in molecules/ions that have a degenerate ground state, the molecule/ion will distort to remove the degeneracy. The Jahn-Teller effect is most often encountered in octahedral complexes of the transition metals [123]. In an octahedral crystal field, the t_{2g} orbitals occur at lower energy than the e_g orbitals [103] 2.3.3. Due to a shielding effect, the Jahn-Teller effect is generally only important for odd number occupancy of the e_g level.

The Jahn-Teller effect is best documented for Mn^{3+} ($t_{2g}^3 e_g^1$) complexes, which are found to have elongation along the z-axis. The energy cost of increased elastic energy can be balanced by a resultant electronic energy saving due to the distortion. As a result, the e_g and t_{2g} group of orbitals may become nondegenerate, making the levels splitting picture becomes more complicated (see Fig. 2.10). When the two apical atoms move away from the ion, which corresponding to an elongation of octahedral, the energy of d_{z^2} becomes lower than that of $d_{x^2-y^2}$ and the degeneracy is lifted. The opposite of this happens when the octahedra is compressed, corresponding to a flattening of octahedral and the lowering of d_{xy} level and $d_{x^2-y^2}$ level in energy scale [103, 124].

To describe the effect, we can define a parameter Q , which denotes the distance of distortion along an appropriate normal mode coordinate. Then the energy cost of this distortion is [103]:

$$E(Q) = \frac{1}{2} M \omega^2 Q^2 \quad (2.23)$$

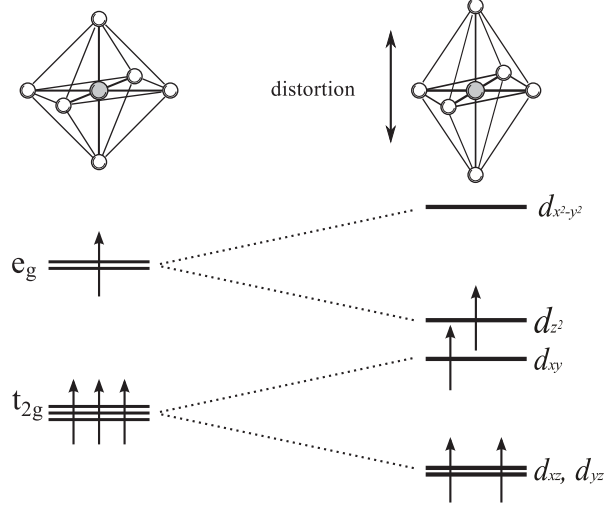


Figure 2.10: Illustration of the Jahn-Teller effect for Mn^{3+} ($3d^4$). A distorted octahedral complex splits the t_{2g} and e_g levels.

where M is the mass of the anion and ω is the angular frequency corresponding to the particular normal mode. Clearly when $Q = 0$, which means there is no distortion, the minimum distortion energy is 0. Then if we suppose there is a raising or lowering of the electronic energy AQ or $-AQ$, the total energy can be written as:

$$E(Q) = \frac{1}{2}M\omega^2Q^2 \pm AQ \quad (2.24)$$

where the two possible choices of the sign of AQ give rise to two different minimum energy for that orbital. The the system can make a net energy saving by spontaneously distortion [103]. In contrast, Mn^{4+} ($t_{2g}^3e_g^0$) would not show this effect because there is no net lowering of the electronic energy by a distortion. This model is called a *static* Jahn-Teller effect. On top of this, if we consider the distortion can switch from one axis to another at high temperature, this can give rise to a *dynamic* Jahn-Teller effect. And if we further imagine that a Jahn-Teller distortion of each complex can occur cooperatively throughout the crystal, then this effect is known as a *cooperative* Jahn-Teller effect [103, 125–127].

2.4 Exchange Interaction

There are two major groups of magnetism. In one group there is no interaction between the individual moments and each moment acts independently, as in diamagnets and paramagnets. In another group of material the magnetic moments couple to one another and form magnetically ordered states. The coupling is known as the exchange interaction and is rooted in the overlap of electrons in conjunction with the Pauli's exclusion principle [128]. This interaction should be analyzed by means of quantum mechanics, since it strongly concerns with spin-spin interactions [128, 129]. More specifically, on an atomic scale, the exchange interaction tends to align spins with

their neighbors. This exchange interaction between the neighboring magnetic ions will force the individual moments into parallel (ferromagnetic) or antiparallel (antiferromagnetic) alignment. They are usually separated to three types of exchanges: direct exchange, indirect exchange and superexchange [128–130].

2.4.1 Direct Exchange

Direct exchange operates between moments close enough to have sufficient overlap of their wave functions [131, 132]. This coupling is strong but decreases rapidly as the ions are separated. An initial simplified understanding of direct exchange can be modeled by two atoms with one electron each. When the atoms are very close together, the electrons are required to be at the same place in space most of time, then Pauli's exclusion principle requires that they possess opposite spins. This gives rise to antiparallel alignment and therefore negative exchange, which will induce antiferromagnetism. If the atoms are far apart, the electrons tend to be away from each other in order to minimize the electron-electron repulsion. This gives rise to parallel alignment, which will cause positive exchange and ferromagnetism.

For a many electron case, the exchange energy can be given by the expectation value of the Heisenberg Hamiltonian [103]:

$$\hat{H} = \sum_{i < j} J_{ij} \hat{\mathbf{S}}_i \cdot \hat{\mathbf{S}}_j \quad (2.25)$$

where J_{ij} is the exchange integral describing the coupling between two spins or magnetic moments represented by the spin operators $\hat{\mathbf{S}}_i$ and $\hat{\mathbf{S}}_j$ [103, 133]. The Bethe-Slater curve, shown in Fig. 2.11, represents the magnitude of direct exchange as a function of interatomic distance.

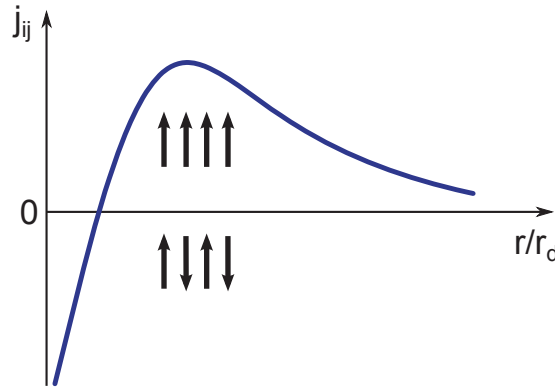


Figure 2.11: Direct exchange energy as a function of the interatomic distance r divided by the radius of the d orbital r_d . The curve is known as the Bethe-Slater curve.

Depending on the interatomic distances or orbital overlapping, the values of J_{ij} might have positive or negative value, resulting in the parallel or antiparallel ground state, respectively [134]. When the interatomic distance is too large, the wave function overlap will become too small, then the direct exchange coupling is not strong enough

to overcome thermal excitations, which will then give rise to paramagnetism. So the direct exchange is a short range interaction. For transition metals, Cobalt is situated near the peak of this curve, while Chromium and Manganese are on the side of negative exchange. Iron is sitting around the zero-crossing point of the curve, with its sign depending on the crystal structures [135]. However, the theoretical estimation of TMOs using this model resulted in values far off from the experimental values, indicating other types of exchanges need to be involved in most TMOs [136].

2.4.2 Indirect Exchange

Indirect exchange couples moments over relatively large distances. It plays an important role in metals, where there is little or no direct overlap of the wave functions with unpaired electrons [103,134]. In this case the interaction between two magnetic moments at sites i and j is mediated by the polarization of the conduction electrons, which in metals are the itinerant electrons. This type of exchange is also known as the RKKY interaction stands for Ruderman-Kittel-Kasuya-Yosida [103,129,137].

The interaction between local magnetic moments $\hat{\mathbf{S}}_i$ and $\hat{\mathbf{S}}_j$ can be given by [103,134]:

$$\hat{H}_{RKKY} = \sum_{i=0}^n J_{ij} \hat{\mathbf{S}}_i \cdot \hat{\mathbf{S}}_j \quad (2.26)$$

where the RKKY exchange coefficient J_{ij} (J_{RKKY}) can be given by:

$$J_{RKKY} \propto \frac{\cos(2rk_F)}{r^3} \quad (2.27)$$

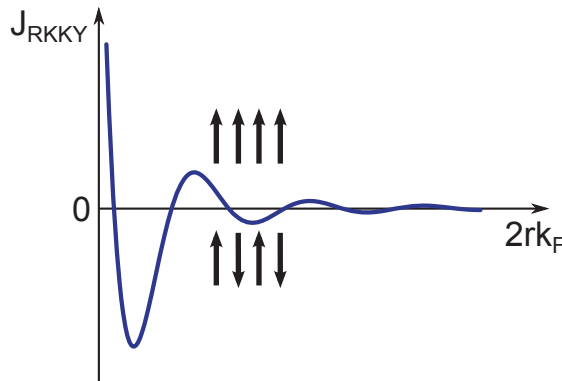


Figure 2.12: The coefficient of RKKY exchange as a function of the interatomic distance r multiplied by the radius of the Fermi sphere k_F .

J_{RKKY} changes from positive to negative as the separation of the ions changes and the characteristic for this coupling mechanism is an oscillatory behavior shown in Fig. 2.12. Therefore depending on the separation between a pair of ions their magnetic coupling can be ferromagnetic or antiferromagnetic. A magnetic ion induces a spin polarization in the neighborhood conduction electrons, which can be felt by

the moments of other magnetic ions within the range. This leads to an indirect coupling [103] and therefore this type of interaction is long-range.

2.4.3 Superexchange

Superexchange is another kind of indirect exchange interaction, which describes the interaction between moments on ions too far apart to be connected by direct exchange, but coupled over a relatively long distance through a non-magnetic material [103,132,138]. Superexchange is important in ionic solids such as the TMOs and transition metal fluorides [1,3,120,139,140].

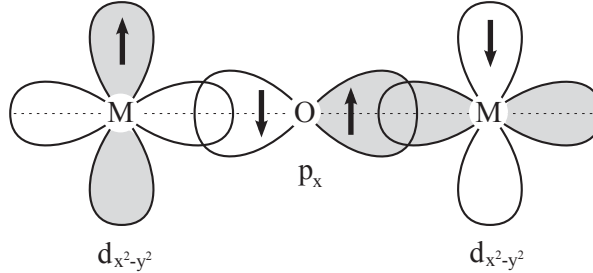


Figure 2.13: Schematic illustration of the superexchange interaction between two magnetic ions M mediated by a non-magnetic oxygen atom.

We take as an example the coupling between the moments on a pair of 3d metal cations (e.g. Mn) separated by a diatomic anion oxygen atom as illustrated in Fig. 2.13. The interaction between the magnetic M atoms is mediated by oxygen through the overlap of the metal's 3d and oxygen's 2p orbital, and a partial delocalization of the involved electrons [103]. For example in MnO, the ground state consists of one electron on each Mn^{2+} in the state $d_{x^2-y^2}$, and two electrons on the O^{2-} ion in identical p orbitals. The p orbitals have a dumbbell shape that coincides with the axis joining the two Mn^{2+} ions. Because of the overlap of their wavefunctions, one p electron from the O^{2-} ion hops over to one of the Mn^{2+} ions. The remaining unpaired p electron on O^{2-} ion then enters into a direct exchange with one electron of the other Mn^{2+} ion [103,141]. The superexchange interaction between the two Mn^{2+} spins is then AFM as shown in Fig. 2.13.

Tuning the moment of M alters the overlap of the cation in the molecule, which changes the magnitude of both the Coulomb and exchange interactions between the cations, leading to a coupling, which depends on the moment's orientation, the orbital overlap between M and the non-metallic element, and the bond angles [103].

2.4.4 Double Exchange

Double exchange happens in compounds which have ions with more than one oxidation state [142]. It was first proposed by Clarence Zener [131] that the e_g electron could hop to a ferromagnetically aligned neighboring ion with a vacancy on the same energy level. However, if the ions are antiferromagnetically aligned, the hopping is

impossible due to the Pauli exclusion principle [124,131]. That's because this electron movement from one ion to another will be facilitated more easily if the electrons do not have to change spin direction in order to conform with Hund's rules when on the accepting ion. The ability to hop (to delocalize) reduces the kinetic energy [143,144].

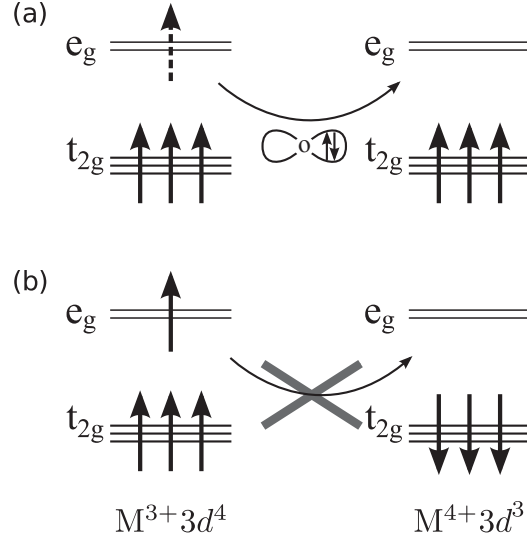


Figure 2.14: Double exchange mechanism gives ferromagnetic coupling between metallic ions with different oxidation states. In a (a) FM configuration, electron delocalization is possible due to the lowering of kinetic energy. In a (b) AFM configuration, electron delocalization is not possible.

To show as an example, in $\text{La}_{1-x}\text{Ba}_x\text{MnO}_3$, Mn has Mn^{3+} and Mn^{4+} [142]. Mn^{3+} ions have four unpaired electrons and Mn^{4+} ions have three unpaired electrons (see Fig. 2.14). When they are ferromagnetically coupled through a double exchange mechanism, the connecting O gives its spin-up electron to Mn^{4+} , its vacant orbital can then be filled by an electron from Mn^{3+} . At the end of the process, an electron has moved between the neighboring Mn ions, retaining its spin direction. Moreover, these hopping e_g electrons can make the material become metallic [103], evidenced by the reduced Jahn-Teller distortion and colossal magnetoresistance. Double exchange is important also for dilute magnetic semiconductors such as $\text{Ga}_{1-x}\text{Mn}_x\text{N}$.

2.4.5 Anisotropic Exchange Interaction

Anisotropic exchange interaction is usually considered as a combined effect of spin-orbit coupling and exchange interaction [145]. It is an extension of the superexchange theory to include the effect of spin-orbit coupling in one of the magnetic ions, which was first suggested from purely symmetry grounds by Dzyaloshinsky [145,146]. This exchange interaction between the excited state of one ion and the ground state of the other ion is also called Dzyaloshinsky-Moriya (DM) interaction [103,145,146]. The

Hamiltonian can be given by [145, 146]:

$$\hat{H}_{DM} = \mathbf{D} \cdot \hat{\mathbf{S}}_1 \times \hat{\mathbf{S}}_2 \quad (2.28)$$

Here \mathbf{D} is the DM vector, which is proportional to the strength of spin-orbit interaction [124]. \mathbf{D} depends on the symmetry of crystal field. When the crystal field has an inversion symmetry with respect to the center between the two magnetic ions, \mathbf{D} vanishes in this ideal case [103]. But in a more common situation, \mathbf{D} will lie parallel or perpendicular to the line connecting the two spins. Then the interaction forces $\hat{\mathbf{S}}_1$ and $\hat{\mathbf{S}}_2$ to be at right angles in a plane perpendicular to the vector \mathbf{D} , which will ensure that the energy is negative [103]. Then this effect usually slightly rotate or cant the spins by a small angle. When this happens in an AFM system, it will result in a small FM component perpendicular to the AFM spin axis. This *weak ferromagnetism* was found in many systems, e.g. α -Fe₂O₃, MnCO₃, CoCO₃ and a most recently studied system Sr₂IrO₄ [103, 115, 124, 145, 146].

Chapter 3 Experimental Methods

The experimental research in our lab focuses on development of novel materials and synthesis of single crystals of d- and f-electron based oxides; experimental studies of highly correlated electron systems with an emphasis on magnetic, transport and thermal properties. In recent years, we have been focusing on growing single crystals of TMOs, e.g. $\text{Ca}_2\text{Ru}_{1-x}\text{M}_x\text{O}_4$ ($\text{M} = 3\text{d}$ transition metal ion) [147–149], $\text{Sr}_2\text{Ir}_{1-x}\text{M}_x\text{O}_4$ ($\text{M} = 3\text{d}$ and 4d transition metal ion) [114,115], $\text{BaIr}_{1-x}\text{M}_x\text{O}_3$ ($\text{M} = 3\text{d}$ and 4d transition metal ion) [150], $\text{Bi}_2\text{Ir}_2\text{O}_7$ [151], NaIrO_3 [152], $\text{Sr}_3\text{CuIrO}_6$ [153]. We are one of the few groups in U.S. who have all the materials synthesis and characterization activities under the same roof. Therefore new developed materials can be expeditiously studied via a broad spectrum of experimental probes. Then these experimental activities can be studied promptly by theoretical modeling, which, in turn, will guide our future design and exploration of new materials.

3.1 Single Crystal Synthesis

It is widely recognized that whoever discovers and controls the optimized synthesis of novel materials generally controls the investigation of their often unique properties and, ultimately, their successful integration into advanced technologies. Research of advanced materials requires the critical capability to synthesize single crystals of new materials. Compared with polycrystalline samples, single crystals have several major advantages for our research: (1) Without the defects associated with grain boundaries or artificial effects due to strain or impurities, single crystals can present unique and clearer properties in mechanical, optical and electrical measurements. (2) For certain types of crystallographic structures with strong anisotropy, which means physical properties are directionally dependent, big differences in physical or mechanical properties can be found when single crystals are measured along different axes. This fact is particularly relevant for the layered compound Ca_2RuO_4 that exhibits strong anisotropic physical properties. (3) These properties ensure that single crystals can be used industrially in a variety of technological applications, especially in optics and electronics. In our lab, we can synthesize large, high quality single crystals. The state-of-the-art bulk crystal growth facility in our lab permits growth of single crystals of a wide range of materials, especially TMO single crystals. Two most-used single crystal growing techniques in our lab are the floating zone (FZ) technique and the flux method. These two techniques complement each other, and the combination of the two makes it possible to grow single crystals of almost all stable TMO materials.

3.1.1 Floating-Zone Technique

Most of the crystals studied in this work were grown by the FZ technique, which has been widely proven to grow high quality single crystals, including for example, the high temperature cuprate superconductors. The FZ technique (Fig. 3.1) is a crystal

growth method that does not use a crucible, and is widely used for semiconductor and metal crystal growth [154]. The method was first used for zone melting purification, taking advantage of the tendency for impurities contained in the feed material to prefer to remain in the melt and thus could be preferentially moved to the end of the feed stock. If the rod was seeded properly, the newly crystallizing material could be obtained as a single crystal. Since the melt never comes into contact with anything but vacuum or inert gases, there are no impurities that the melt could pick up by dissolving the crucible material, which is the major problem for conventional Czochralski method [155].

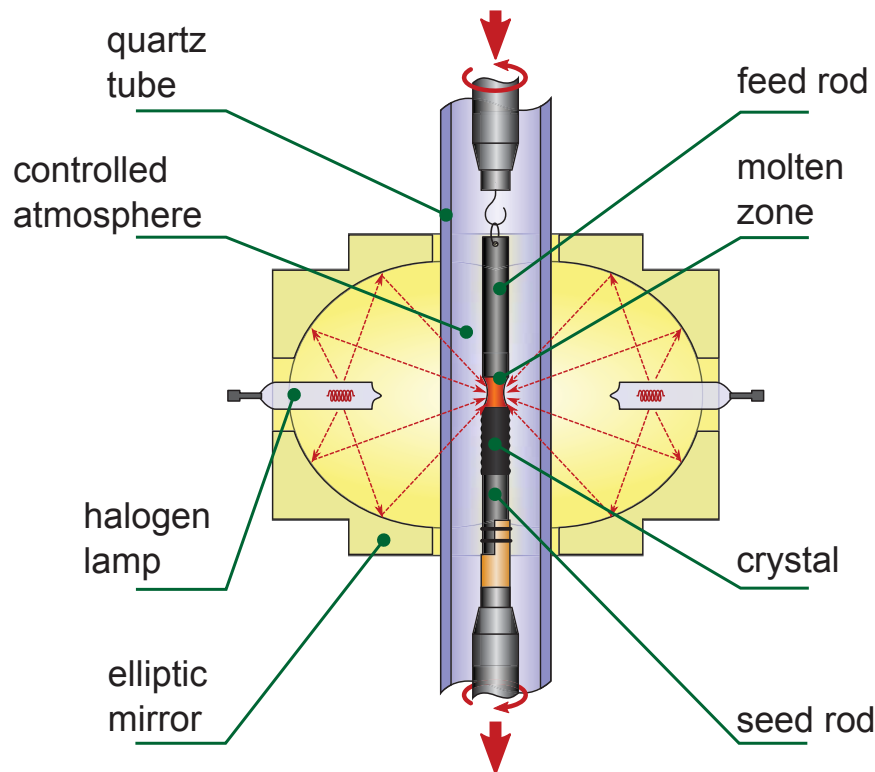


Figure 3.1: A Schematic diagram of the optical floating zone furnace.

Fig. 3.1 shows how a double elliptic type image furnace works. Two halogen lamps of 1.5 KW power are installed in the mirrors outer focus, and act as a heating source. The inside surface of the mirrors are gold-plated to increase their reflectance [156]. With two 1.5kW halogen lamps, the ultimate temperature at the focal point can reach as high as 2000 °C. The temperature at the central focus point can then be adjusted by tuning the power of the lamps [156]. A polycrystalline feed rod prepared by a standard solid-state reaction method is suspended using a platinum wire from a platinum hook on the upper shaft. The seed rod is fastened coaxially to the sample holder on the top of the lower shaft. Both the upper and lower shafts are connected

to controlling motors that allow for independent vertical translation and rotational motions (Fig. 3.1). Different types of gas atmosphere and pressure can be applied within the quartz tube during crystal growth. The growing process starts by forming a floating molten zone between feed and seed rod. Then the seed rod moves down continuously from the molten zone while the feed rod is continuously lowered into the molten zone to supplement lost material. The whole growth process is monitored through a CCD camera connected to a computer.

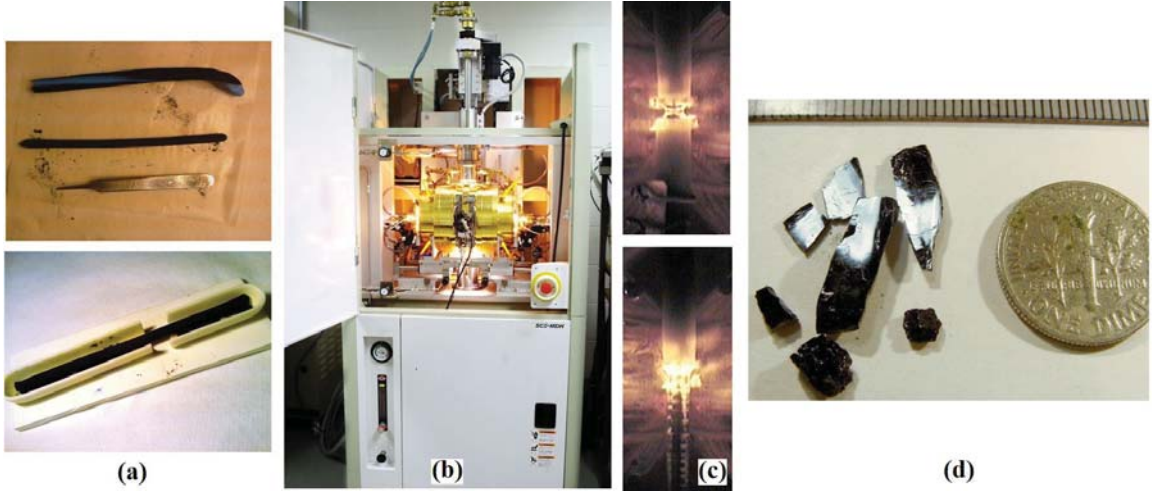


Figure 3.2: (a) Feed rod preparation. (b) FZ furnace in action during a crystal growth. (c) Different stages in a crystal growth. (d) Actual size of single crystal $\text{Ca}_2\text{Ru}_{1-x}\text{Cr}_x\text{O}_4$.

The single crystals of $\text{Ca}_2\text{Ru}_{1-x}\text{M}_x\text{O}_4$ ($\text{M} = \text{Cr}, \text{Mn}$ and Fe) with $0 < x < 0.25$ were grown using a NEC Model SCII-MDH-11020 FZ optical furnace. The polycrystalline rods for the crystal growth are prepared with starting material, CaCO_3 and RuO_2 and M_2O_3 compounds, which are preheated separately to get rid of moisture. Then they are mixed and ground in an agate mortar and cooked twice to ensure a uniform mixing. After that, the mixtures are filled into a clean cylinder-shaped rubber balloon (Fig. 3.2(a)) and compressed under a pressure of around 40MPa. Fig. 3.2(b) shows the actual FZ machine during operation and Fig. 3.2(c) shows the feed and seed rod at the beginning and the end of the growth process. Due to the volatility of RuO_2 , the ratio of Ca to Ru in the feed rod has to be adjusted in order to compensate for this loss. At the same time, the crystal growth has to be performed at an extremely fast rate. With combination of all these adjustments, we can obtain high-quality $\text{Ca}_2\text{Ru}_{1-x}\text{M}_x\text{O}_4$ crystals as large as $20 \times 5 \times 5 \text{ mm}^3$ as shown in Fig. 3.2(d).

3.1.2 Flux Technique

The Flux method is also commonly used in our lab to grow crystals from molten salts or from pure metal solvents at high temperature. With the flux solvent, the synthesis

can happen well below the melting temperature of the solute phase, which is the main advantage of this method over growth from the pure melt. In the flux technique, the idea is not to crystallize the entire mixture, but to grow a few, smaller crystals, using a melt or solution that has the necessary composition to give the best results. Fig. 3.3 shows some representative crystals recently grown using the flux technique.

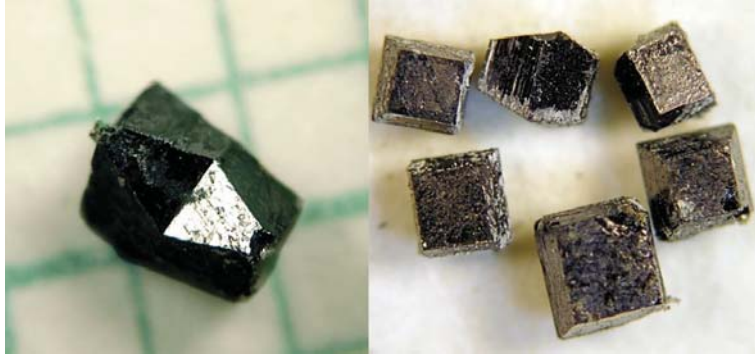


Figure 3.3: Some representative crystals of recently grown using flux techniques.

Some single crystals of pure Ca_2RuO_4 for this study were grown using self-flux techniques from non-stoichiometric quantities of RuO_2 , CaCO_3 , and CaCl_2 . The general self-flux method procedure involves loading this mixture into a crucible, melting it, cooling it through the temperature range where crystals form, and extracting the crystals. Ruthenium oxides, being relatively volatile, usually require that the crucible is equipped with a lid to help suppress the diffusion of RuO_2 vapours. The starting ratio of Ca:Ru has a large influence not only on the form of crystals but also on the ratio of Ca:Ru in the crystals [157]. The resulting shapes of Ca_2RuO_4 tend to be plate-like with an average size of the single crystals being $1 \times 1 \times 0.4 \text{ mm}^3$. The correct phase is initially confirmed using powder X-ray diffraction, followed by detailed single-crystal X-ray measurements at various temperatures.

3.2 Structural Characterization

3.2.1 Energy Dispersive X-ray

Energy Dispersive X-ray (EDX) is a chemical analysis technique to determine the concentration of most elemental species in a given sample. The fundamental principle behind this method is the emission and detection of X-rays from a given sampling volume that are characteristic to specific elements. A material can produce x-rays when bombarded with high-energy electrons. Assuming the Bohr model for an atom, the electron beam excites the tightly-bound inner shell electron of an atom sufficiently to eject an electron and thereby produce a hole in the inner shell. The atom is then left in an excited or ionized state. To compensate, an electron from an outer shell will drop to fill the inner shell hole, and then this transition will emit an X-ray with energy equal to that energy difference between the two electron states [158]. The energy and wavelengths of the emitted X-rays are characteristic of the excited atom

of the particular chemical elements, from which the chemical composition can be obtained by integrating the area under the intensity peak. The output for an EDX analysis is a plot of X-ray counts as function of characteristic energy in kiloelectron volts (keV).

The energy difference between the shells changes significantly even when the atomic number Z changes by one unit. That is why EDX is able to provide reliable data. This dependence may be expressed as equation 3.1, which is called Moseley's relation [159,160]:

$$\lambda = \frac{B}{Z - C^2} \quad (3.1)$$

Where B and C are constants that differ for each family of transitions and λ is the wavelength of characteristic X-ray beam. For heavier elements ($Z \geq 11$) the shell structure is sufficiently complex that ionization of the innermost shell leads to a transition from more than one shell, thus the subscript of α , β , γ is used to define the most probable transitions to K , L or M shells in order of observed intensity [159,160].

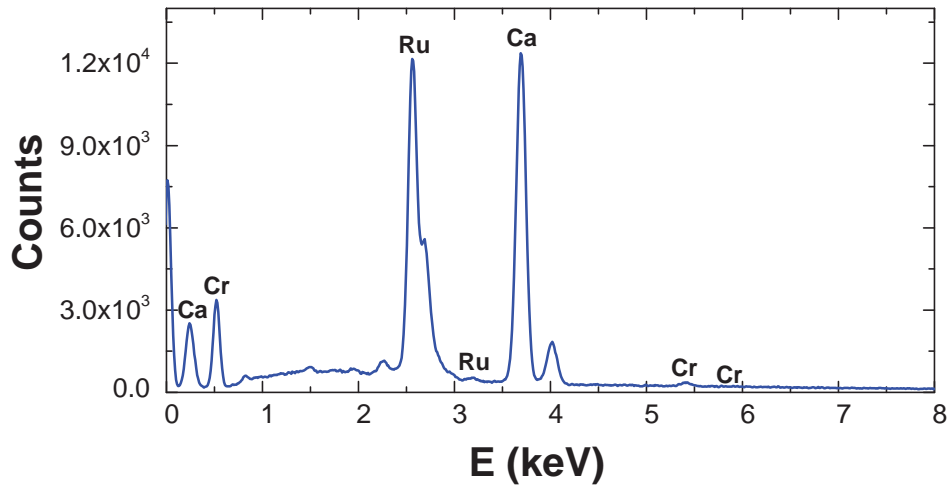


Figure 3.4: EDX spectrum of a single crystal of $\text{Ca}_2\text{Ru}_{1-x}\text{Cr}_x\text{O}_4$ studied in this work, with corresponding element peaks labeled.

Chemical compositions of our samples were determined by EDX using a commercial Scanning Electron Microscope (SEM) instrument, the Hitachi S3200-N, which is equipped with a liquid nitrogen cooled Si(Li) EDX detector. The data (see Fig. 3.4) was plotted in the form of photon counts as a function of their characteristic energy, as discussed above. This instrument has an ultra thin window (UTW) which enables us to detect chemical elements above carbon. The EDX data confirmed the high homogeneity of all crystals studied in this work.

3.2.2 Powder X-ray Diffraction

Powder X-ray diffraction (XRD) is a commonly used and a highly effective technique for the phase identification of crystalline solids in that the diffraction pattern for every

phase is unique. X-ray diffractometers consist of three basic elements: an X-ray tube, a sample holder, and an X-ray detector [161] (see Fig. 3.5). By heating its filament, a cathode ray tube produces electrons, which can then be accelerated toward a target by applying a voltage. The impact of the electrons with the target will then generate characteristic X-ray spectra if electrons have sufficient energy to dislodge inner shell electrons of the target material. These X-rays are collimated and directed onto the sample. When the wavelength of the incoming X-ray satisfies the Bragg equation, constructive interference occurs. A detector will then record this diffraction X-ray signal and convert the signal to a count rate which is then output to computer.

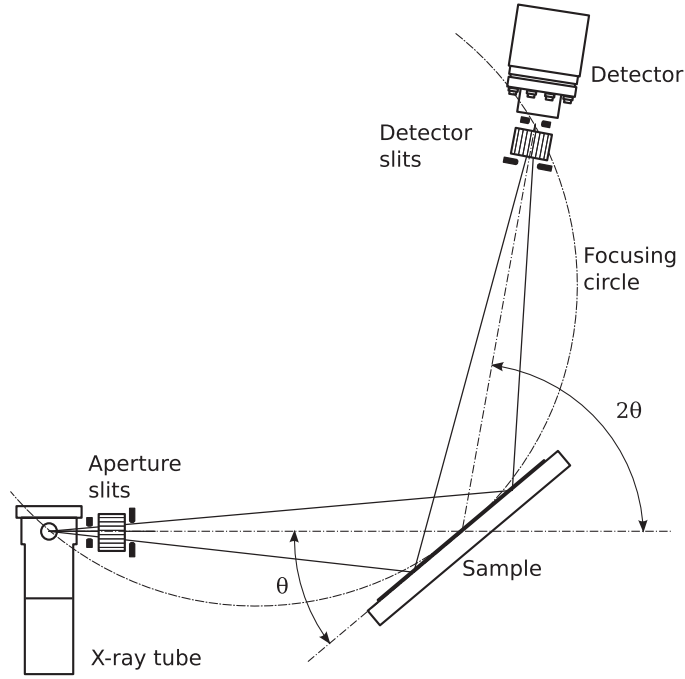


Figure 3.5: Schematic diagram of a powder X-ray diffractometer in θ - 2θ configuration.

A schematic diagram of a typical powder X-ray diffractometer is shown in Fig. 3.5. The X-ray source and detector are mounted on the coaxial rotating goniometer arms. For the most common θ - 2θ mode, the rotation angle of the detector is twice that of the sample holder. A sample is placed on a stationary holder made of a polymer or a zero background silicon oxide single crystal cut along a non-diffracting plane.

In this work, powder XRD measurements were carried out on a Scintag X1 diffractometer equipped with Cu $K\alpha$ X-ray source ($\lambda = 1.5418 \text{ \AA}$) and a liquid- N_2 cooled germanium solid state detector [161] and on a Bruker D8 powder X-ray diffractometer housed in Center for Advanced Materials (CAM) at University of Kentucky. The samples are single crystals ground into fine powder using an agate mortar and pestle. The powdered sample is smeared in the center of a zero-background quartz sample holder. Phase identification from the recorder scan is performed using the International Centre for Diffraction Data (ICDD) database [162].

3.2.3 Single Crystal X-ray Diffraction

The single crystal X-ray diffraction is dedicated to the understanding of crystal and molecular structure, packing, symmetry, pseudosymmetry, polymorphism, structure-function, structure-reactivity and structure-property relationships.

For single-crystal studies the X-ray beam source is usually configured to produce a spot-like beam shape whereas in powder instruments X-ray sources are usually set to produce a line-focused beam shape. Compared to the sample holder in a powder diffractometer, single crystal diffractometers use a more complicated goniometer to position or rotate the sample in a variety of orientations. Historically, most single-crystal diffractometers have used a 4-circle goniometer, as shown in Fig. 3.6. These circles refer to the four independent angles: ϕ - the angle of rotation of the crystal about the axis of goniometric head; χ - the angle of inclination of the ϕ -axis; Ω - the angle of rotation of the crystal with respect to the principal axis of the goniometer; 2θ - the swing angle of the detector. These angles define the relationship between the crystal lattice, the incident ray and detector. Samples are mounted on thin glass fibers which are attached to hollow copper pins and mounted onto goniometer heads. Adjustment of the X, Y and Z orthogonal directions allows centering of the crystal within the X-ray beam.

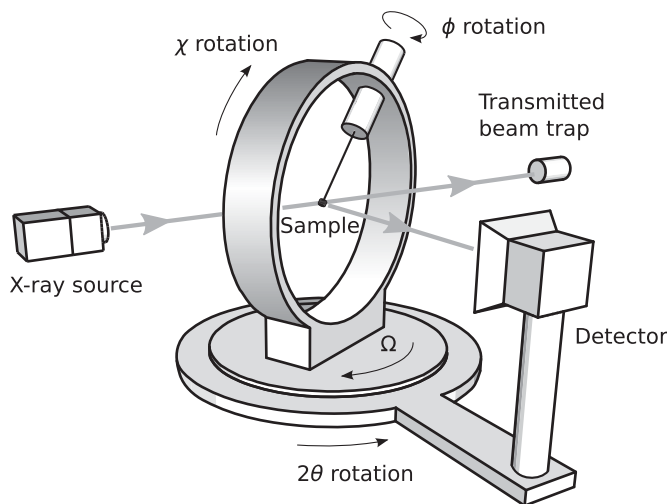


Figure 3.6: Schematic of the classical four-circle single-crystal X-ray diffractometer.

There are a variety of detectors for diffraction measurements, which can be mainly divided into two major types: point type detectors and area detectors. Point type detectors are usually made of a scintillator, photomultiplier tube, and electronics. Area detectors include image plates, multi-wire proportional counters, vidicons (TV cameras), and charge-coupled devices (CCDs). For single crystal diffractometers, the ccd detectors have become the most popular because of their short readout time, broad counting range, and robust nature [163]. The two great benefits of area detectors over point detectors are: first, the background is greatly reduced, so that weaker spots are measured more precisely; second, the entire diffraction pattern can be collected more quickly [164, 165].



Figure 3.7: Nonius kappaCCD MoK α X-ray diffractometer.

The single crystal X-Ray diffractometer used most in this research is a Nonius kappaCCD sealed-tube MoK α diffractometer. This diffractometer is equipped with low-temperature machine from CryoIndustries of America which can deliver a constant, low-velocity flow of cold nitrogen gas over the crystal. Low temperature has many benefits for X-ray structure determination, including better quality data in less time than for room-temperature work, the ability to handle highly reactive compounds with minimal fuss, and most importantly, structure transition due to temperature change can be investigated using this setup.

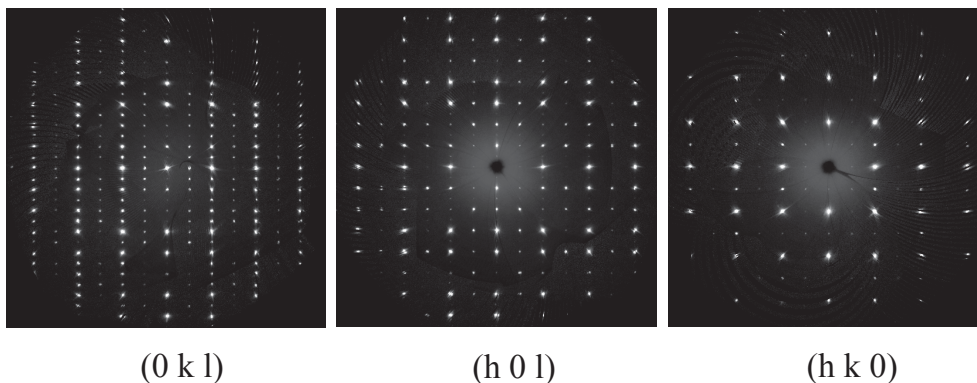


Figure 3.8: Diffraction pattern from Ca_2RuO_4 sample obtained with the Kappa CCD diffractometer. Each point in reciprocal space represents a family of atomic planes in real space.

Fig. 3.8 shows the Bragg diffraction peaks on (0kl), (h0l) and (hk0) directions for Ca_2RuO_4 . A full data set may consist of hundreds of separate images taken at different orientations of the crystal. After merging and scaling these various images, the position of spots (reflections) and the relative strength of each spot (intensities) can be used to calculate electron density, and thereby determine the structure. The structure of the Ca_2RuO_4 single crystal is highly ordered, as evidenced by sharp and

bright Bragg diffraction spots along all the directions.

Our single-crystal x-ray diffraction study of $\text{Ca}_2\text{Ru}_{1-x}\text{M}_x\text{O}_4$ was performed as a function of temperature between 90K and 430K. The data treatment of the observed reflections and the structural refinement were carried out using the SHELX-97 package [166]. All structures affected by absorption and extinction were corrected by comparison of symmetry-equivalent reflections using the program SADABS [167] and occasionally with *XABS2* [168]. It needs to be emphasized that the single crystals are of high quality and there is no indication of any mixed phases or inhomogeneity in all doped single crystals studied. The presence of any mixed phases or inhomogeneity in the single crystals would likely have prevented successful structural refinements.

3.3 Physical Properties Measurement

3.3.1 Magnetization and Susceptibility Measurement

The magnetization M is the vector field that expresses the density of induced magnetic dipole moments in a magnetic material, which can be either from the motion of electrons in atoms or the spin of the electrons [169]. Magnetic susceptibility χ is a dimensionless constant that indicates the degree of magnetization of a material in response to an applied magnetic field H [170], which can be given by $M = \chi H$. The measurement of the magnetic susceptibility of a TMO allows us to determine the number of unpaired electrons in this compound. This knowledge of the number of unpaired electrons associated with the transition metal in the compound is especially useful in understanding the compound's bonding and its magnetic characteristics [171, 172]. Materials are classified as paramagnetic if $\chi > 0$ (field is strengthened by the material) and as diamagnetic if $\chi < 0$ (field is weakened). In superconducting states $\chi = -1$ (perfect diamagnet).

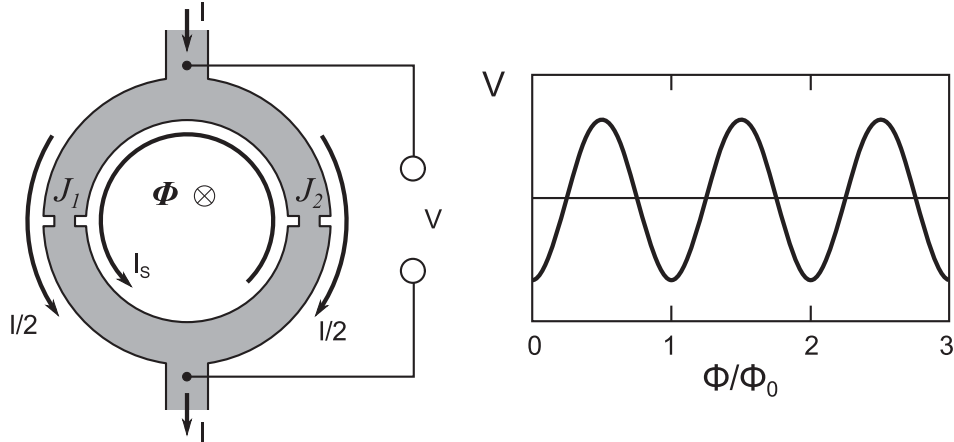


Figure 3.9: Illustration of DC-SQUID and $V (\Phi/\Phi_0)$ for constant bias current I .

A setup we used most to measure magnetization and susceptibility is a Quantum Design MPMS XL system which is a high-sensitivity SQUID magnetometer. The core part of the SQUID is a ring formed by Josephson junctions connected in parallel, as

illustrated in Fig. 3.9. One of the discoveries associated with Josephson junctions was that flux is quantized in unit of Φ_0 :

$$\Phi_0 = \frac{h}{2e} = 2.067833636 \times 10^{-15} T \cdot m^2 \quad (3.2)$$

When there is no external magnetic field, a current will tunnel through the junction and split symmetrically into the two branches. The application of an external magnetic field will lead to a screening current I_s . Due to a quantization of magnetic flux in a superconducting material, the magnitude and direction of I_s will depend on the ratio Φ/Φ_0 . The change in current is detected by the counter in form of voltage pulses. Each voltage peak equates to an increase in one flux quanta Φ_0 . Thus such a system can be used to convert electrical voltage into magnetic flux [173,174].

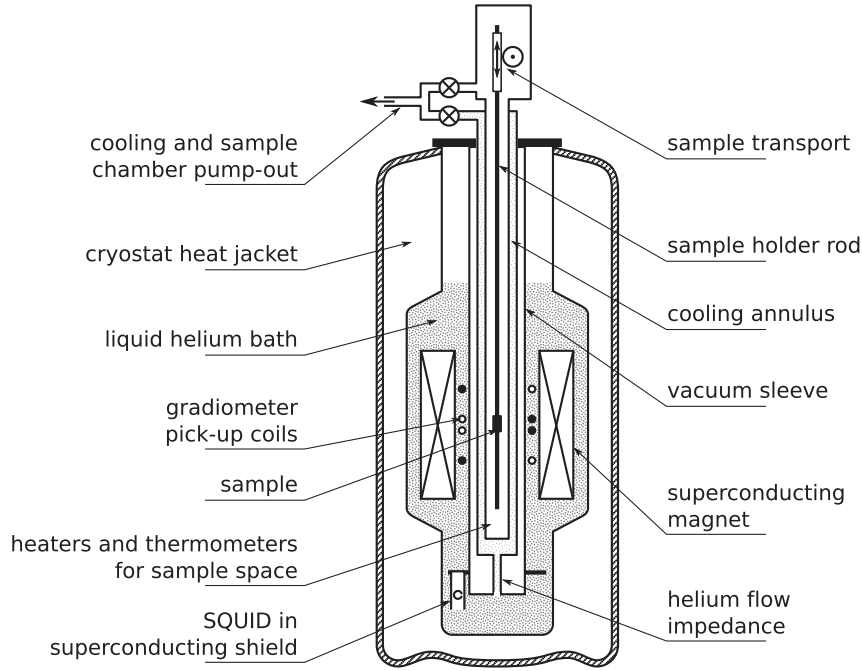


Figure 3.10: Schematic cross-section of the Quantum Design MPMS.

The sample chamber of the MPMS is located inside the superconducting magnet, which is immersed in liquid helium, as shown in Fig.3.10. The sample space temperature can be controlled by the combination of flowing liquid helium and built-in heaters and thermometers. The sample is mounted on a quartz rod and fixed onto one end of the nonmagnetic probe, with which the sample can be moved up and down through a set of pickup coils. Then voltages are read as a function of the sample's position in the pickup coils [175–177]. The maximum applied magnetic field in our SQUID is 7 T and the measured temperature range is 1.7 K - 400 K .

3.3.2 Resistivity Measurement

Electrical resistivity quantifies how strongly the material opposes the flow of electric current [178]. Resistivity measurements have typically been employed to examine electronic properties of TMOs. TMOs include insulators, metals as well as superconductors. It is common to see the same material display both types of transport properties, hence a Metal-Insulator transition, obtained by varying temperature.

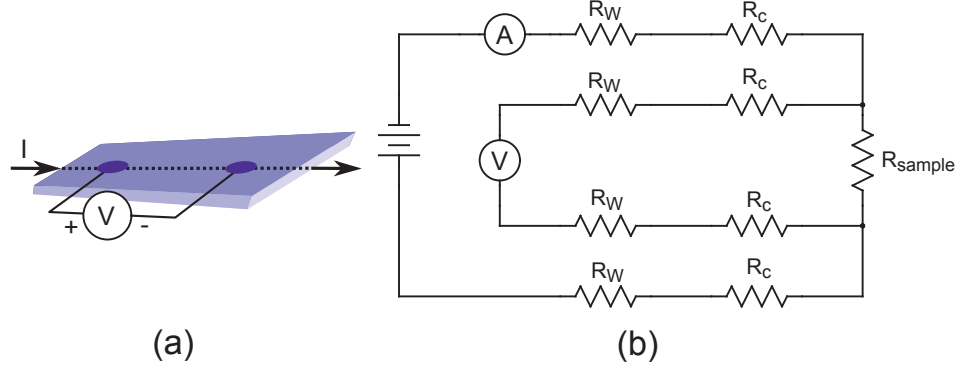


Figure 3.11: (a) Schematic diagrams of the four-leads method measurement for in-plane resistivity; (b) Equivalent circuit of four-point probe setup for resistivity measurements.

The electric resistivity of the crystal can be measured using the standard four-probe method shown in Figure 3.11(a): a input current I is applied parallel to ab plane and passes through the entire transverse crosssection area. The contour forms a series loop, therefore the electric current is the same everywhere. then the potential difference can be measured by two leads ($V+$ and $V-$). The potential difference is measured only across the sample, thus the probe resistance, probe contact resistance and spreading resistance can be excluded from measurements. Therefore the four-point method has more accuracy than the regular two point method. According to Ohm's law, the ratio of voltmeter indication to applied current value yields the resistance:

$$R = \frac{V}{I} \quad (3.3)$$

Here, V is the voltage drop across the inner two probes and I is the current flow through the sample. Thus, the resistivity of the material can be assessed using the resistance R and geometry of the sample:

$$\rho = \frac{R \cdot A}{L} \quad (3.4)$$

where A is the cross-sectional area and L is the distance between the two inner probes.

Fig. 3.11(b) is an equivalent circuit to show this four probe setup, where R_W is connecting wire resistance and R_C is the contact resistance of the leads/sample interface. R_W is clearly outside the points between which the potential difference

was measured. Thus they are prevented from being added to sample resistance. R_C will also not be added simply because an ideal voltmeter is supposed to have an infinite resistance and thus no current flows through it, and hence no voltage drop across it. However, effort still needs to be invested to minimize the contact resistance to effectively avoid the local resistive heating of the sample. Thus the single crystal sample surface should be prepared and the leads bonding compound should be selected according to the experimental conditions and type of materials. In this study, we use two-component solid silverfilled epoxy EPO-TEK H20E from Epoxy Technology Inc. [179] for leads attachment. The electrical leads connecting between the sample and sensing probes are gold wires of diameter 0.001". The samples are glued on sample holders using highly thermoconducting adhesives such as Phenolic Butvar varnish VGE-7031 by General Electric [180].

The AC-resistivity between 1.7K and 400K was measured with an LR-700 AC resistance bridge from Linear Research Inc. , which allow us to resolve the resistance from nano-Ohm range up to $2M\Omega$ [181]. To avoid the contribution of the reactance of the circuit in AC measurements, we usually verify the data by DC resistivity method. In a DC measurement, current is provided with a Keithley Model 2400 or Model 6220 Current Source and voltage is recorded with a Keithley 2182 nanovoltmeter. Data are recorded under GPIB control of these instruments with a computer. A custom transport measurements probe for the standard Quantum Design MPMS serves within a broad temperature range 1.7K-400K and external magnetic field can be applied up to 7 Tesla [175].

3.3.3 Specific Heat Measurement

Heat capacity or specific heat is a key property in thermodynamics and solid state physics. It includes information on how much the energy of the material increases when the temperature rises, depending on the type and number of excited states in the material. Obviously, this property is also of interest in daily use and applications.

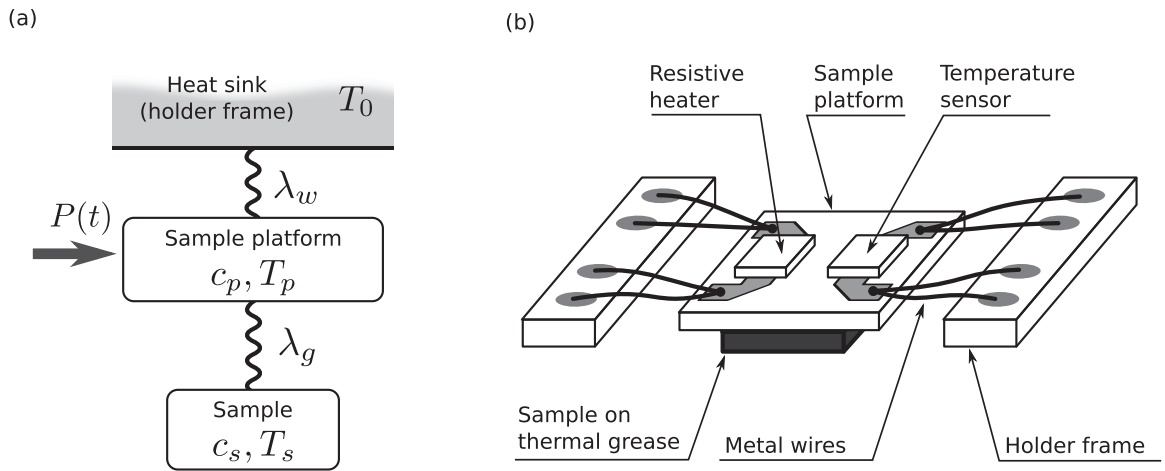


Figure 3.12: (a) Illustration of Two-Tau model for sample and sample holder; (b) schematic drawing of microcalorimeter sample holder design.

All the specific-heat measurements in this work were carried out on a heat capacity option of Quantum Design PPMS, which can ramp within a wide temperature range from 1.8K to 400K with applied field up to 9 Tesla. Fig. 3.12 (b) shows the specific sample puck used with the PPMS. A small quartz plate is used as sample platform, which is fixed by very thin wires to reduce heat transfer to the environment as much as possible. A thermometer and resistive heater are integrated in the plate. A certain amount of thermal conducting grease is applied to the surface of the sample platform to provide reliable thermal contact. In our lab we use vacuum grease Apiezon type N [182] for measurements at low temperature range and Apiezon type H [183] for high temperature measurements up to 400 K.

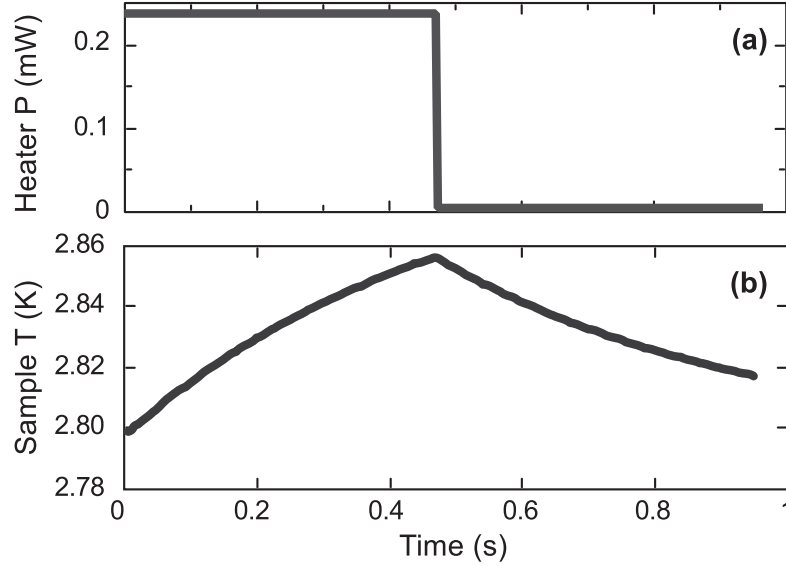


Figure 3.13: (a) A heat pulse input; (b) The change of sample temperature in a microcalorimeter as a function of time due to the heat applied.

As shown as a flow chart in Fig. 3.12 (a), heat capacity measurement on PPMS consists of several distinct stages: First, the sample platform and puck temperatures are stabilized at some initial temperature. Then a heat signal is applied to the sample platform heater for a predetermined length of time, causing the sample platform temperature to rise. After that, the temperature of the sample platform relaxes toward the puck temperature. The sample platform temperature is monitored throughout both warming and cooling (see Fig. 3.13). After each warming and cooling cycle, the temperature response of the system can be fitted by two-tau model [184, 185], which can be expressed as below:

$$\begin{aligned}
 c_p \frac{dT_p}{dt} &= P(t) - \lambda_g(T_p(t) - T_s(t)) - \lambda_w(T_p(t) - T_0(t)) \\
 c_s \frac{dT_s}{dt} &= \lambda_g(T_p(t) - T_s(t))
 \end{aligned}
 \tag{3.5}$$

where "p" represents "platform" and "s" represents "sample"; c_p / c_s are heat capacities; $T_p(t) / T_s(t)$ are the temperatures. λ_g is the thermal conductivity of the grease between the two; λ_w is the thermal conductance of the wires supporting the platform as can be seen in Fig. 3.12.

Specific heat measurement can directly probe phase transitions. When a first order phase transition happens, the heat capacity is, in principle, a delta function at the transition temperature. In real measurement, it is a very narrow sharp peak observed at the transition temperature [186]. If the system undergoes a second-order phase transition, a broad anomaly in specific heat will appear around the transition temperature. In $\text{Ca}_2\text{Ru}_{1-x}\text{M}_x\text{O}_4$ samples, we can see both first order structural transition and second order magnetic transition.

4.1 Ca_2RuO_4

The pure compound Ca_2RuO_4 exhibits a MI transition at $T_{MI} = 357$ K and a radical change in electrical resistivity $\rho(T)$ below T_{MI} , which also marks a concomitant and particularly violent structural transition between a high-T tetragonal and a low-T orthorhombic phase (see Fig. 4.1) [36, 157]. Particularly, the a-axis contracts by 1.5% below T_{MI} , but the b-axis expands by 3% on cooling over an interval of 250 K; the combined effect of these uniaxial thermal expansions is to drive an increasingly strong orthorhombic distortion that shatters single-crystal samples and contracts the volume by 1.3% as T is lowered from 400 K to 70 K [35, 36, 187, 188]. Then one may suggest that Ca_2RuO_4 is a simple band insulator due to the structural changes. But the long-range antiferromagnetic order at $T_N = 110$ K suggests that such a model is not compatible since the equally filled bands of spin-up and spin-down electrons in a band insulator would not show magnetic ordering. So the MI transition in Ca_2RuO_4 should be Mott type, which resembles that in V_2O_3 [94, 189].

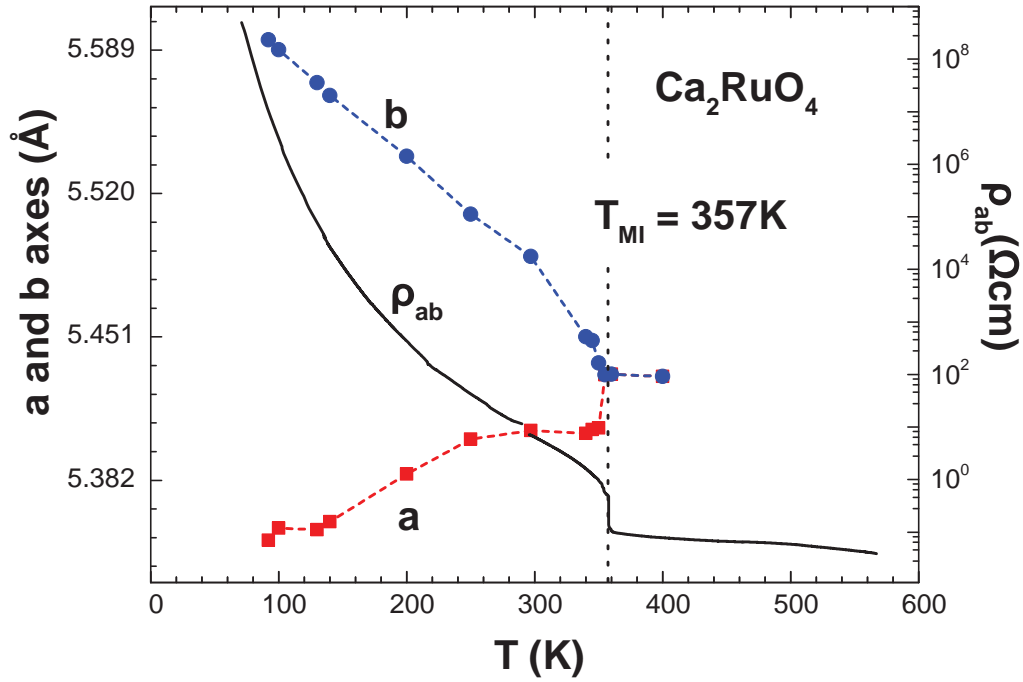


Figure 4.1: Temperature dependence of the a- and b-axis lattice parameters, and the ab-plane resistivity ρ_{ab} (right scale) for Ca_2RuO_4 .

The MI transition induces a radical change in electrical resistivity by over nine orders of magnitude below T_{MI} (see Fig. 4.1), which marks the concomitant and violent structural transition between the high-T tetragonal and the low-T orthorhombic

phase at T_{MI} and a strong cooperative Jahn-Teller distortion [35, 36, 187]. It is already established that such a strong cooperative Jahn-Teller distortion removes the degeneracy of the three Ru t_{2g} orbitals (d_{xy} , d_{yz} , d_{zx}) via a transition to orbital order that, in turn, drives the MI transition at $T_{MI} = 357$ K [190–194], which is followed by the AFM order at $T_N = 110$ K, well below $T_{MI} = 357$ K, sharply contrasting classic Mott insulators that undergo simultaneous transitions to AFM order and an insulating state at T_{MI} . This behavior, which is also observed in its sister compound, $\text{Ca}_3\text{Ru}_2\text{O}_7$ [157], separates the layered $\text{Ca}_{n+1}\text{Ru}_n\text{O}_{3n+1}$ ($n = 1$ and 2) from classic Mott insulators as a unique archetype of Mott insulators in which the MI transition is not primarily driven by AFM order. Controversy over the exact nature of the orbital state remains, but the extraordinary sensitivity of T_{MI} to modest changes in lattice parameters or modest pressure [188, 190–196] clearly indicate that the lattice and orbital degrees of freedom play a decisive role in the new physics that drives Ca_2RuO_4 .

4.2 $\text{Ca}_2\text{Ru}_{1-x}\text{Cr}_x\text{O}_4$

4.2.1 Structure of $\text{Ca}_2\text{Ru}_{1-x}\text{Cr}_x\text{O}_4$

Impurity doping is a perturbation that can tip the balance of U/W ratio (see Chap. 2.2.1 and Chap. 1.1) and as a result change the physical properties drastically. We first pursued studies of Cr doped Ca_2RuO_4 [148] as Cr substitution for Ru tends to significantly change physical properties but retain the crystal structure in the ruthenates, such as $\text{CaRu}_{1-x}\text{Cr}_x\text{O}_3$ [197] and $\text{Ca}_3(\text{Ru}_{1-x}\text{Cr}_x)_2\text{O}_7$ [198]. By substituting elements with a different ionic radius and the same valence, bandwidth can be controlled relative to the amplitude of the local electron - electron interaction by keeping the electron density fixed at a commensurate value [199]. This approach is advantageous to the study of lattice structure, especially the distortion of RuO_6 octahedra, and its direct relation with transport properties.

$\text{Ca}_2\text{Ru}_{1-x}\text{Cr}_x\text{O}_4$ consists of layers of RuO_6 octahedrons with Ca between the layers (Fig. 4.2). Note that the neighboring layers are not stacked exactly on top of each other, but are offset with respect to each other. This pattern clearly demonstrates the enormous structural distortion in this system. The in-plane tilt and rotation around the c axis of RuO_6 octahedra is readily apparent and all the distortion angles can be measured directly. The neighboring octahedra tilt in an ordered way, which becomes clearer in a projection of the unit cell on the ac plane (Fig. 4.2). The layers are formed by corner-sharing RuO_6 octahedra. Looking down on the ab plane, we find that octahedra on the same layer rotate left and right alternately along the $[1\ 1\ 0]$ direction (Fig. 4.2). That reflects the change of Ru - O - Ru bond angle, which should be 180° in the ideal case.

$\text{Ca}_2\text{Ru}_{1-x}\text{Cr}_x\text{O}_4$ has only one Ru position, so Cr is doped on this specific site. The room-temperature lattice parameters (Table 4.1) agree well with literature values [35, 187] and theoretical values [200]. An important feature of this structure is that there is only one in-plane oxygen position, which means all in-plane oxygen ions have the same distance to the planes formed by the Ru atoms.

Table 4.1: Experimental and refinement details of $\text{Ca}_2\text{Ru}_{1-x}\text{Cr}_x\text{O}_4$ ($x = 0.067$) at selected temperatures.

	90 K	190 K	290 K
Crystal Data			
Chemical formula	$\text{Ca}_4\text{Ru}_{1.866}\text{Cr}_{0.134}\text{O}_8$	$\text{Ca}_4\text{Ru}_{1.866}\text{Cr}_{0.134}\text{O}_8$	$\text{Ca}_4\text{Ru}_{1.866}\text{Cr}_{0.134}\text{O}_8$
M_r	474.02	474.02	474.02
Crystal system, space group	Orthorhombic, <i>Pbca</i>	Orthorhombic, <i>Pbca</i>	Orthorhombic, <i>Pbca</i>
Temperature (K)	90	190	290
a, b, c (Å)	5.3917 (2), 5.5157 (2), 11.8804 (4)	5.3920 (3), 5.4432 (3), 12.0037 (6)	5.3359 (3), 5.3528 (3), 12.2571 (7)
V (Å ³)	353.31 (2)	352.31 (3)	350.09 (3)
Z	2	2	2
Radiation type	$\text{MoK}\alpha$	$\text{MoK}\alpha$	$\text{MoK}\alpha$
μ (mm ⁻¹)	6.99	7.01	7.05
Crystal size(mm)	$0.05 \times 0.05 \times 0.05$	$0.01 \times 0.05 \times 0.05$	$0.01 \times 0.05 \times 0.05$
Data Collection			
Diffractometer	Nonius KappaCCD diffractometer	Nonius KappaCCD diffractometer	Nonius KappaCCD diffractometer
Absorption correction	Multi-scan SADABS	Multi-scan SADABS	Multi-scan SADABS
No. of measured, independent and observed [$I > 2\sigma(I)$] reflections	7241, 398, 352	7265, 396, 260	7243, 403, 228
R_{int}	0.03	0.026	0.027
Refinement			
$R[F^2 > 2\sigma(F^2)], \omega R(F^2), S$	0.016, 0.046, 1.13	0.028, 0.080, 1.10	0.016, 0.044, 1.14
No. of reflections	398	396	393
No. of parameters	36	36	36
No. of restraints	0	0	0
$\Delta\rho_{max}; \Delta\rho_{min}$ (e Å ⁻³)	0.66, -0.60	1.33, -0.96	0.58, -0.57

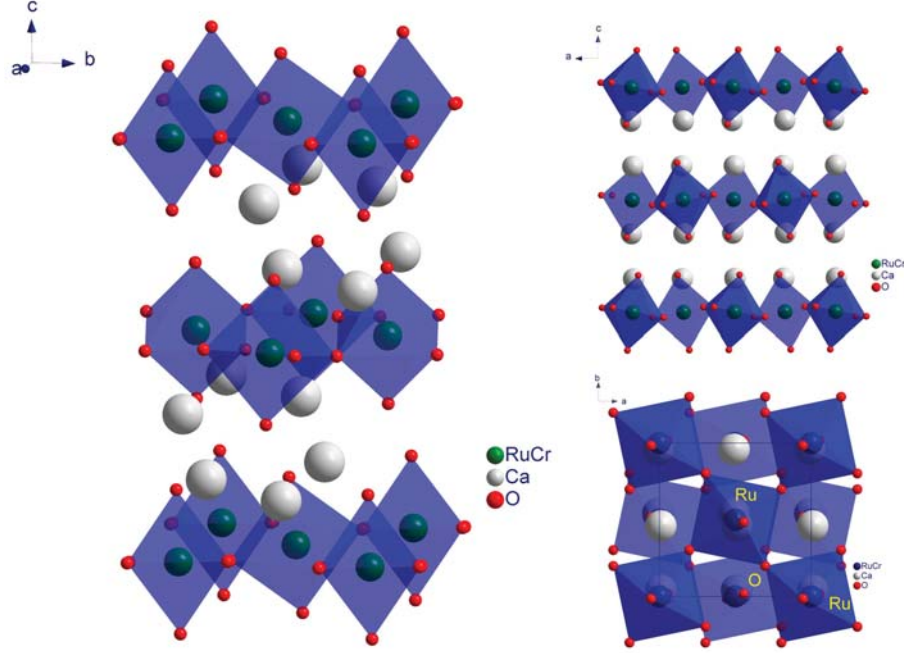


Figure 4.2: Room-temperature structure of $\text{Ca}_2\text{Ru}_{1-x}\text{Cr}_x\text{O}_4$ with projection onto the ac plane and the ab plane.

4.2.2 Temperature dependence of the $\text{Ca}_2\text{Ru}_{1-x}\text{Cr}_x\text{O}_4$

The cell parameters all changed significantly with decreasing temperature (Table 4.1). These changes were not simply a result of thermal contraction because they were not uniform. Indeed, we observed opposite trends for cell parameters parallel and perpendicular to the direction of buckling of the layers. Comparing high temperature and low temperature lattice parameters in Fig. 4.3, it is clear that a and b are elongated while c shrink, reflecting the flattening of RuO_6 octahedra, which is expected to greatly influence the crystal field that determines electron occupancy in the triply degenerate orbital state of ruthenate. It was ascertained to arise from a Jahn-Teller effect [187]. The temperature dependence of the lattice constants (Fig. 4.3) and the volume (Fig. 4.4) is indicative of profound structural changes. Moreover, the lattice volume V of $\text{Ca}_2\text{Ru}_{1-x}\text{Cr}_x\text{O}_4$ abruptly expands with cooling below T_{MI} , giving rise to a huge *negative volume thermal expansion* (NVTE) with total volume expansion $\Delta V/V \sim 0.9\%$ over the temperature range $90\text{K} < T < 290\text{K}$. This orthorhombic distortion and the extremely large and anisotropic thermal expansions indicate a dominant structural distortion, which is frequently due to a rotation of the octahedral [187]. In $\text{Ca}_2\text{Ru}_{1-x}\text{Cr}_x\text{O}_4$ the RuO_6 octahedra have the freedom to rotate around an axis parallel to c , which is in turn related to the observed increase of b .

Fig. 4.5 shows the temperature dependence of the three angles which are used to describe the tilt and distortion of the octahedra. The definition of the angles are the same with Braden et al. [187]: O1 is the oxygen on basal plane and O2 on top and bottom vertex. Θ -O1 is the tilt angle between the octahedron basal

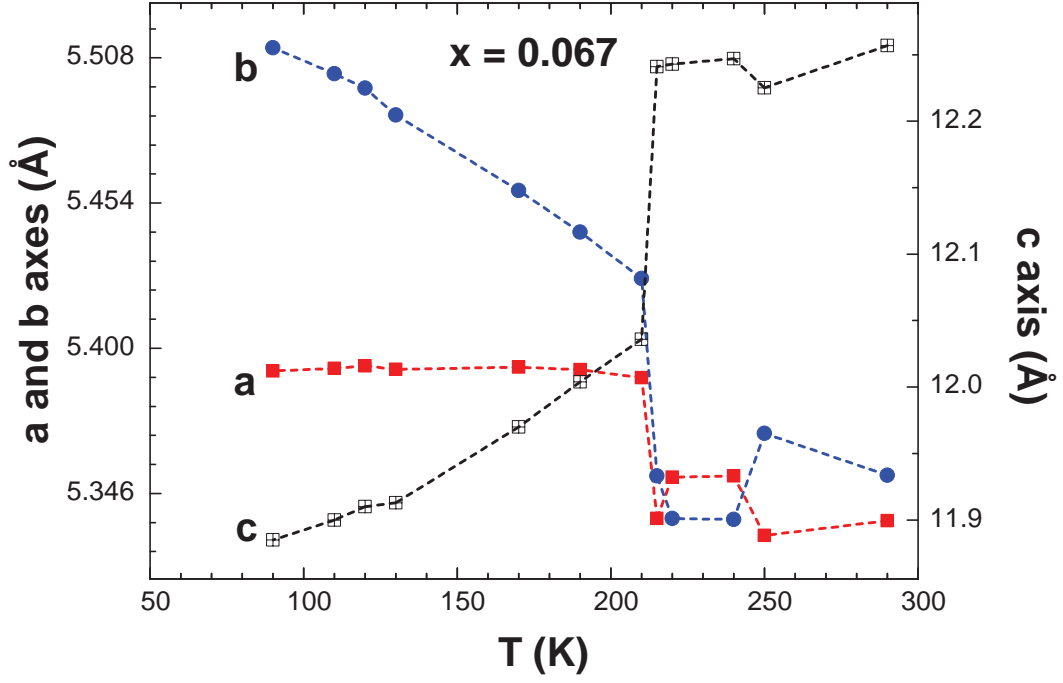


Figure 4.3: Temperature dependences of lattice parameters *a*-, *b*- and *c*-axis (right scale) for $x = 0.067$.

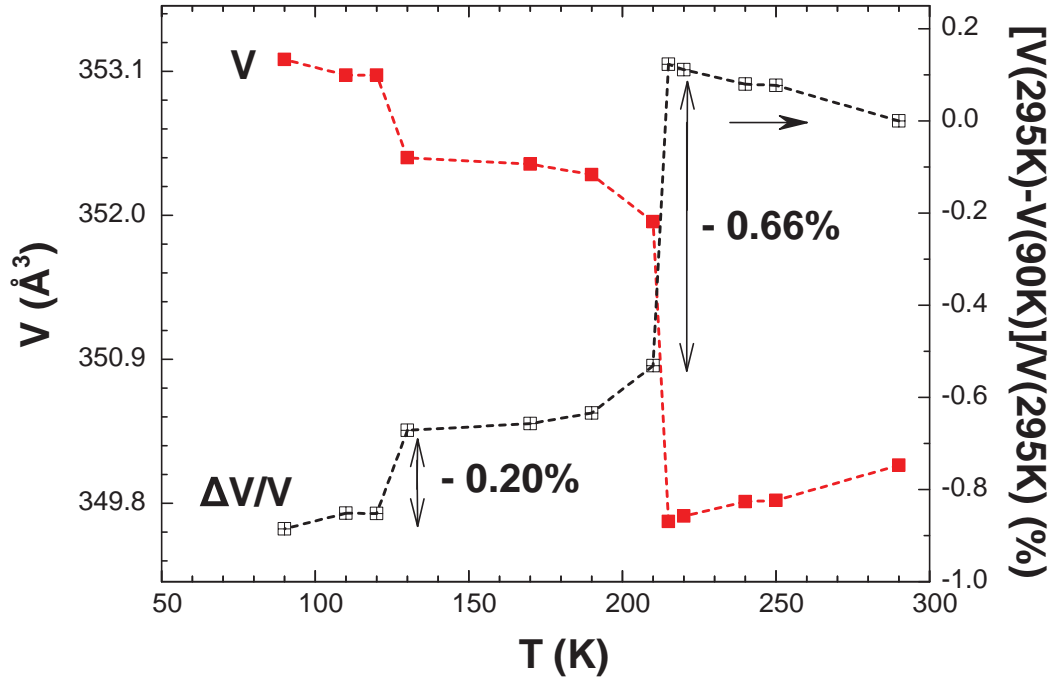


Figure 4.4: Temperature dependences of unit cell volume V and thermal expansion ratio V/V (right scale) for $x = 0.067$.

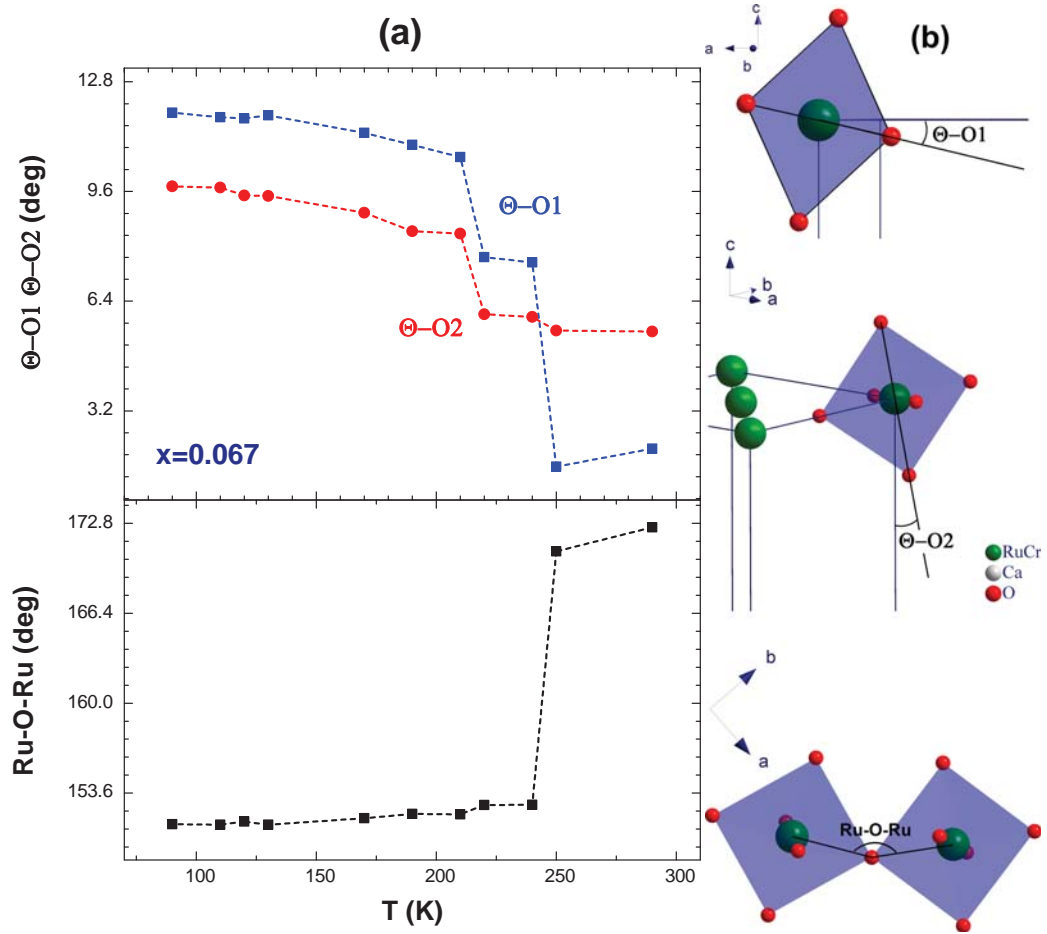


Figure 4.5: (a) Temperature dependence of the tilt, rotation and bond angles in $\text{Ca}_2\text{Ru}_{1-x}\text{Cr}_x\text{O}_4$ ($x = 0.67$), obtained from single-crystal X-ray diffraction; and (b) definition of $\Theta\text{-O1}$, $\Theta\text{-O2}$ and Ru-O-Ru distortion angles.

plane and the ab plane. $\Theta\text{-O2}$ is the angle between the Ru-O2 bond and the c axis. Ru-O-Ru is the bond angle between two connected Ru-O bonds. Dramatic changes of all three distortion angles can be observed in Fig. 4.5. All the RuO_6 octahedra alternately rotate in opposite directions in the direction of infinite chains of corner-sharing RuO_6 octahedra. The big decrease of Ru-O-Ru bond angle and the big increase of both $\Theta\text{-O1}$ and $\Theta\text{-O2}$ on cooling show the incremental structure distortions with decreasing temperature. The Ru-O-Ru bond angle is considerably less than the ideal 180 degree and the decrease of Ru-O-Ru bond angle upon cooling shows the rotation of octahedra around the c axis. This implies insulating behavior due to narrowing of the d -electron bandwidth [35]. The temperature change provides sufficient perturbation to the system to tip the balance of U/W ratio across the metal - nonmetal boundary, resulting in an insulator.

The resistivity and magnetic susceptibility as a function of temperature are shown in Fig.4.6. The abrupt transition from an insulating state to a nearly metallic state occurs at $T_{MI}=357$ K in the pure compound [36]. In our $x = 0.067$ sample, the sudden

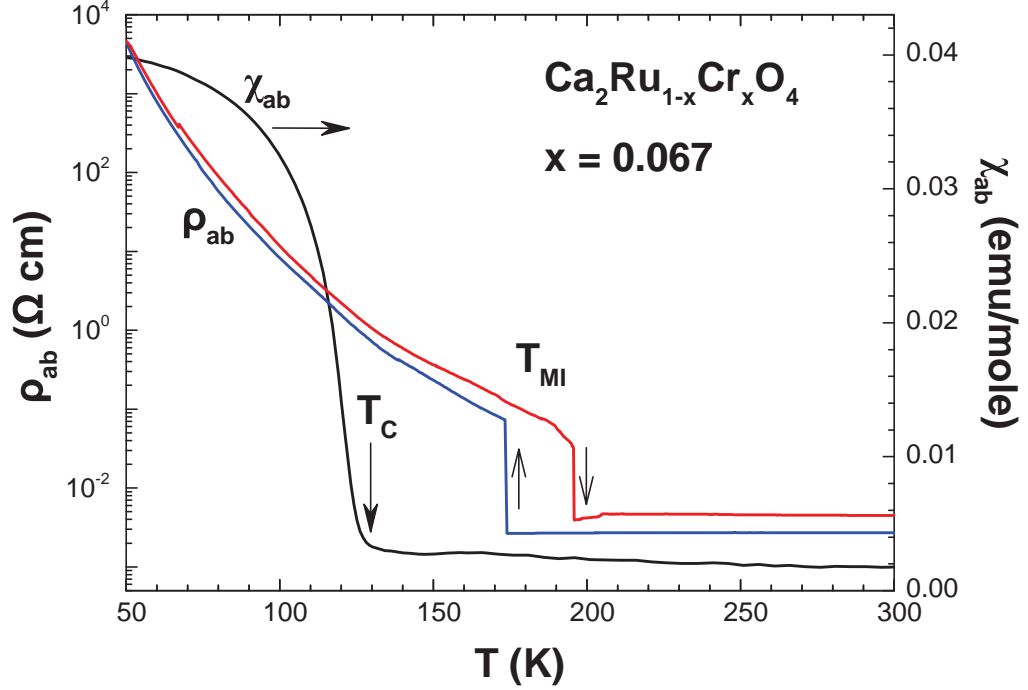


Figure 4.6: Temperature dependences of ab-plane resistivity ρ_{ab} and magnetic susceptibility χ_{ab} (right scale) at $\mu_0 H = 0.5$ T for $x = 0.067$.

decrease of resistivity by more than two orders of magnitude can be clearly observed and it characterizes a discontinuous alteration in the d-band structure typical of a metal-insulator transition [36]. Below the transition, $\rho(T)$ rises rapidly, increasing several orders of magnitude over a relatively narrow temperature interval. The wide hysteresis region are shown in Fig.4.6, indicating that the metal-insulator transition is first-order. T_{MI} happens at the same temperature with the structural transition and NVTE. This structurally-driven metal-insulator transition can be directly related to the enhancement of structure distortion with decreasing temperature as discussed above.

Throughout the entire measured temperature range, the magnitude of $\rho(T)$ for the doped sample is more than one order of magnitude smaller than the pure sample. For all samples with $0 < x < 0.10$, a metallic phase at $T > T_{MI}$ can be well established. In order to elucidate the electronic state in the insulating phase, we analyze the electrical resistivity in the ab plane, $\rho_{ab}(T)$, of single crystal $\text{Ca}_2\text{Ru}_{1-x}\text{Cr}_x\text{O}_4$ for $x = 0.032$. As shown in Fig. 4.7, the result does not fit well to activation-type insulating behavior [201]: $\rho(T) = \rho(0) \exp(E_G/2k_B T)$ in the temperature range $70\text{K} < T < 300$ K. In the same T region of the insulating phase, $\rho(T)$ can well fit to the Efros - Shklovskii mechanism. The Efros - Shklovskii mechanism can be given by $\rho(T) = \rho(0) \exp(T_0/T)^{1/(n+1)}$ ($n = 1, 2, 3$), which represents the n dimensional Variable-Range Hopping (VRH) without interaction among the localized electrons: T_0 is the characteristic temperature. In almost all concentrations of Cr, VRH fits of $\rho(T)$ were much better than the activation law. However, the behavior of the low temperature

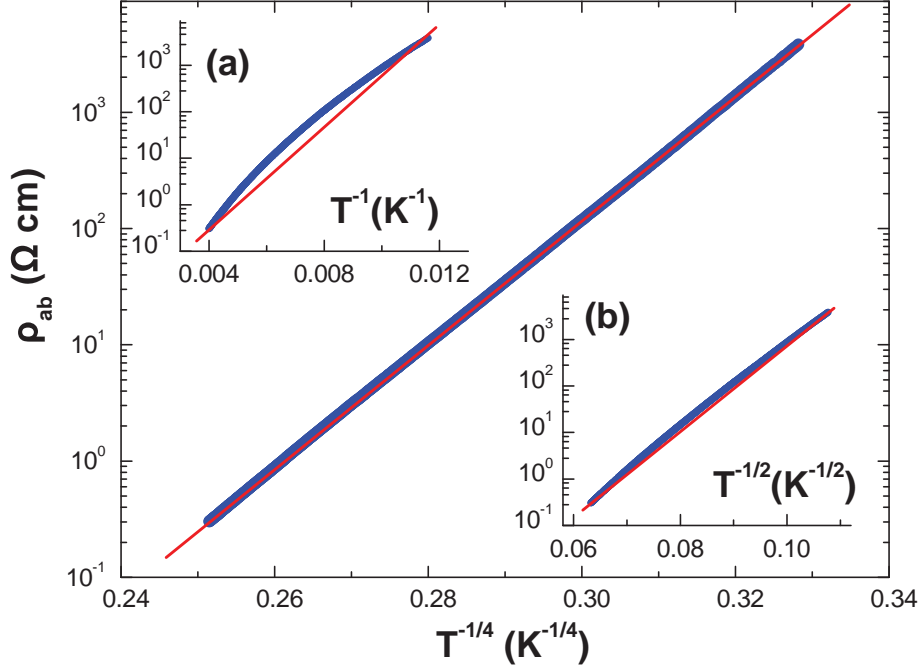


Figure 4.7: Fit of the electrical resistivity in the ab plane, $\rho_{ab}(T)$, of single crystal $\text{Ca}_2\text{Ru}_{1-x}\text{Cr}_x\text{O}_4$ for $x = 0.032$ to variable-range hopping with $n = 3$. Inset: (a) Fit to activation-type insulating behavior were not good; and (b) variable-range hopping with $n = 1$ is less good.

$\rho(T)$ for pure sample and Cr doped sample is fundamentally different. For pure sample ($x = 0$), VRH fits best with $n = 1$ [1,4]. While for $x > 0$, VRH fits best when $n = 3$, as shown in Fig. 4.7, thus Cr doping fundamentally changes the low temperature range conductivity behavior.

The overall temperature dependence of $\text{Ca}_2\text{Ru}_{1-x}\text{Cr}_x\text{O}_4$ samples and the close correlation of NVTE with orbital and magnetic order illustrates our major findings as summarized below: (1) Strong, negative linear thermal expansion occurs not only along the b -axis, but also along the a -axis for $x > 0$ (Fig. 4.3), which gives rise to the much rarer case of NVTE. The overall NVTE is punctuated by an abrupt expansion at T_{MI} . (2) Discontinuities in the a -, b - and c -axis lattice parameters signal a first-order phase transition from a high- T tetragonal, to a low- T orthorhombic phase at 210 K (Fig. 4.3). (3) V abruptly expands by 0.66% with decreasing T near 210 K, and expands again by 0.2% at $T_C = 130$ K, but changes only slightly between these two temperatures (Figs. 4.4 and 4.6).

4.2.3 Cr concentration dependence of the $\text{Ca}_2\text{Ru}_{1-x}\text{Cr}_x\text{O}_4$

The experimental and refinement details of the single crystal X-ray diffraction data with different Cr% are given in Table 4.2. The results of the full structure refinements and comparisons of bond lengths and distortion angles are given in Table 4.3. The Cr concentration dependence of the lattice constants was determined up to 13.5%

(Table 4.3). The position of Ru atom is always (0,0,0). Ru-O-Ru means the bond angle between connected Ru-O bonds and the tilt angles are determined at the two oxygen sites. Note that the tilt is always around the b axis. Selected Ru-O distances of $\text{Ca}_2\text{Ru}_{1-x}\text{Cr}_x\text{O}_4$ obtained at 90 K are also gathered in Table 3. O1 denotes the oxygen in the RuO_4 basal plane and O2 means the oxygen on top and bottom apex of an octahedron. The increase of Ru-O2 bond with increasing Cr doping is counter to the usual thermal expansion. The shrink of the in-plane bond is also remarkable. The overall elongation of the RuO_6 octahedra along the c axis might be associated with a Jahn-Teller distortion. Similar distortions of octahedra and large octahedral tilt angles are also reported in manganites [202] and vanadates [203].

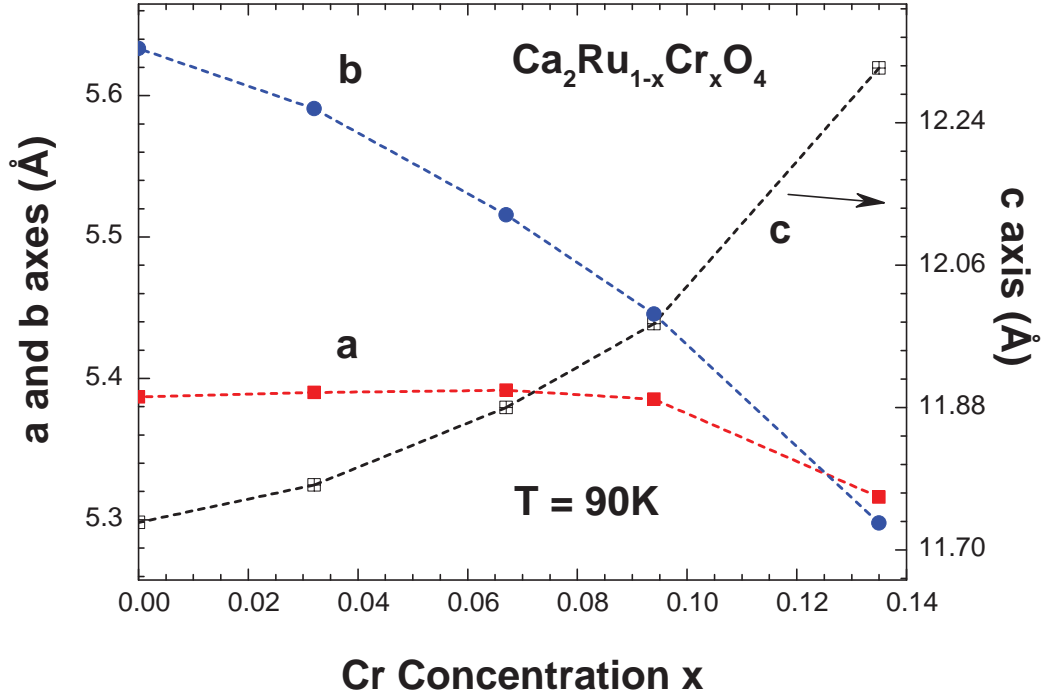


Figure 4.8: Cr concentration x dependence of the a -, b - and c -axis lattice parameters (right scale) for $T = 90$ K.

Fig. 4.8, 4.9 and 4.10 illustrate the overall trends observed in our structural data for $\text{Ca}_2\text{Ru}_{1-x}\text{Cr}_x\text{O}_4$ ($0 < x < 0.135$) single crystals. In Fig. 4.8, we can clearly see the effect of Cr-doping leads to a trend opposite to that of cooling (Refer to Fig. 4.3). Cr doping reduces and eventually suppresses the orthorhombic distortion (e.g., $[b-a] = 0.247$ Å for $x = 0$, but $[b-a] = 0.018$ Å for $x = 0.135$ at $T = 90$ K; see Fig. 4.8). With increased Cr concentration, the c axis is enormously elongated, reflecting the elongation of RuO_6 octahedra by Cr doping. Alternatively, the flattening of RuO_6 octahedra with decreasing temperature is suppressed by Cr doping. The increased volume of the unit cell on cooling, which indicated an extremely large orthorhombic distortion, is also shown to be suppressed with increasing Cr doping.

The weakening structural distortion is accompanied by relaxation of the Ru-O1-Ru bond angle and elongation of the RuO_6 octahedra (i.e., the Ru-O2 bond distance),

Table 4.2: Experimental and refinement details of $\text{Ca}_2\text{Ru}_{1-x}\text{Cr}_x\text{O}_4$ with different x.

	x=0	x=0.032	x=0.067	x=0.094	x=0.135
Crystal Data					
Chemical formula	$\text{Ca}_4\text{Ru}_2\text{O}_8$	$\text{Ca}_4\text{Ru}_{1.936}\text{Cr}_{0.064}\text{O}_8$	$\text{Ca}_4\text{Ru}_{1.866}\text{Cr}_{0.134}\text{O}_8$	$\text{Ca}_4\text{Ru}_{1.812}\text{Cr}_{0.188}\text{O}_8$	$\text{Ca}_4\text{Ru}_{1.73}\text{Cr}_{0.27}\text{O}_8$
M_r	490.26	474.02	474.02	474.02	469.85
Crystal system, space group	Orthorhombic, $Pbca$	Orthorhombic, $Pbca$	Orthorhombic, $Pbca$	Orthorhombic, $Pbca$	Orthorhombic, $Pbca$
Temperature (K)	90	90	90	90	90
a, b, c (Å)	5.3869 (2), 5.6334 (2), 11.7349 (5)	5.3901 (1), 5.5909 (2), 11.7819 (4)	5.3917 (2), 5.5157 (2), 11.8804 (4)	5.3852 (2), 5.4454 (2), 11.9859 (4)	5.3160 (2), 5.2978 (3), 12.3091 (7)
V (Å ³)	356.11 (2)	355.05 (2)	353.31 (2)	351.48 (2)	346.66 (3)
Z	2	2	2	2	2
Radiation type	$\text{MoK}\alpha$	$\text{MoK}\alpha$	$\text{MoK}\alpha$	$\text{MoK}\alpha$	$\text{MoK}\alpha$
μ (mm ⁻¹)	7.13	6.95	6.99	7.02	7.07
Crystal size(mm)	$0.08 \times 0.08 \times 0.04$	$0.08 \times 0.05 \times 0.04$	$0.05 \times 0.05 \times 0.05$	$0.10 \times 0.08 \times 0.05$	$0.08 \times 0.05 \times 0.04$
Data Collection					
Diffractometer	Nonius KappaCCD diffractometer	Nonius KappaCCD diffractometer	Nonius KappaCCD diffractometer	Nonius KappaCCD diffractometer	Nonius KappaCCD diffractometer
Absorption correction	Multi-scan SAD-ABS	Multi-scan SAD-ABS	Multi-scan SAD-ABS	Multi-scan SAD-ABS	Multi-scan SAD-ABS
No. of measured, independent and observed $[I > 2\sigma(I)]$ reflections	6050, 399, 342	7175, 396, 367	7241, 398, 352	6955, 390, 362	7546, 441, 338
R_{int}	0.031	0.025	0.03	0.025	0.033
Refinement					
$R[F^2 > 2\sigma(F^2)], \omega R(F^2), S$	0.021, 0.055, 1.11	0.016, 0.037, 1.10	0.016, 0.046, 1.13	0.018, 0.049, 1.17	0.026, 0.068, 1.33
No. of reflections	399	396	398	390	441
No. of parameters	36	36	36	35	34
No. of restraints	0	0	0	0	0
$\Delta\rho_{max}, \Delta\rho_{min}$ (e Å ⁻³)	0.73, -0.85	0.55, -0.60	0.66, -0.60	0.61, -1.10	0.97, -0.95

Table 4.3: Structure refinement results of $\text{Ca}_2\text{Ru}_{1-x}\text{Cr}_x\text{O}_4$ with different x at 90 K.

Space group	$x=0$ Pbca	$x=0.032$ Pbca	$x=0.067$ Pbca	$x=0.092$ Pbca	$x=0.135$ Pbca
a (Å)	5.3869(2)	5.3901(1)	5.3917(2)	5.3852(2)	5.3160(2)
b (Å)	5.6334(2)	5.5909(2)	5.5157(2)	5.4454(2)	5.2978(3)
c (Å)	11.7349(5)	11.7819(4)	11.8804(4)	11.9859(4)	12.3091(7)
V (Å ³)	356.11(2)	355.05(2)	353.31(2)	351.48(2)	346.66(3)
Ca x/a	0.00297(12)	0.00462(8)	-0.00732(8)	0.00928(7)	0.0088(2)
Ca y/b	0.05957(14)	0.0555(1)	0.04771(13)	0.04074(12)	0.0165(2)
Ca z/c	0.35246(6)	0.35218(5)	0.35145(5)	0.35057(6)	0.34826(13)
O1 x/a	0.1937(4)	0.1951(3)	0.0608(4)	0.1975(3)	0.1953(9)
O1 y/b	0.3011(4)	0.3012(3)	-0.0190(3)	0.3011(3)	0.3042(10)
O1 z/c	0.0280(2)	0.02672(15)	0.16479(16)	0.02214(12)	0.0118(3)
O2 x/a	-0.0701(6)	-0.0665(4)	-0.1967(3)	-0.0556(4)	-0.0296(9)
O2 y/b	-0.0217(4)	-0.0212(3)	0.3008(3)	-0.0166(3)	-0.0063(7)
O2 z/c	0.1644(2)	0.16470(15)	0.02456(15)	0.16488(14)	0.1650(4)
Ru-O1 (Å)	2.018(2)	2.0087(17)	1.9907(16)	1.9724(14)	1.922(5)
Ru-O1 (Å)	2.021(2)	2.0103(16)	1.9915(16)	1.9740(14)	1.929(5)
Ru-O2(Å)	1.970(2)	1.9769(17)	1.9878(18)	2.0008(17)	2.038(5)
Ru-O-Ru (deg)	149.46(13)	150.11(10)	151.14(10)	152.00(9)	154.0(3)
Θ-O1(deg)	13.419(47)	12.872(33)	11.966(38)	10.925(28)	6.098(76)
Θ-O2(deg)	11.626(68)	11.010(51)	9.970(55)	8.993(48)	4.528(138)

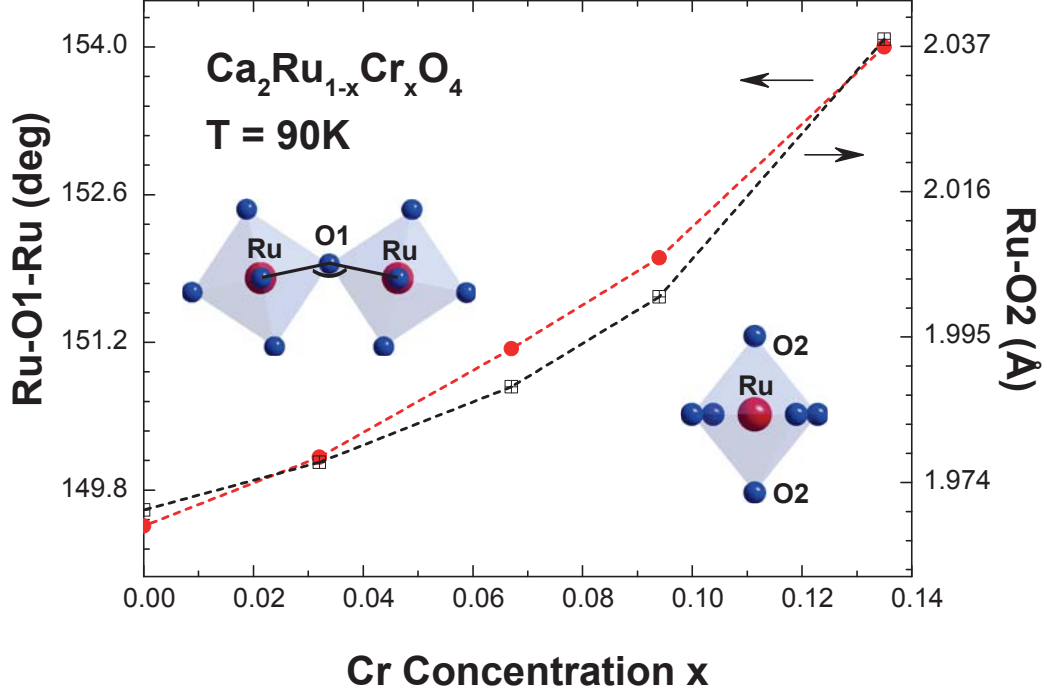


Figure 4.9: Ru-O1-Ru bond angle θ and the Ru-O2 bond distance (right scale) for $T = 90$ K. Inset: Schematics of the distorted Ru-O1-Ru bond angle θ and a RuO6 octahedron.

as shown in Fig. 4.9. The tilt, rotation and bond angle changes in the structure of $\text{Ca}_2\text{Ru}_{1-x}\text{Cr}_x\text{O}_4$ are suppressed by Cr doping. We observe significant decrease in tilt angles with increasing Cr: With 3.2% Cr concentration, $\Theta\text{-O2}$ angle goes down to $11.0(5)^\circ$, comparing with $11.63(7)^\circ$ for pure sample. When x increases to 0.135 the $\Theta\text{-O2}$ angle has decreased to $4.53(14)^\circ$. The similar decrease of $\Theta\text{-O1}$ and increase of Ru - O - Ru angles also provide evidence that increasing Cr concentration can suppress the structure distortion. The close association of this unusual suppression of structural distortion with increasing Cr to different physical properties was investigated in detail and will be shown below.

Cr doping causes the unit cell volume V to expand as T is lowered from 295 K to 90 K for $0.032 < x < 0.13$, as shown in Fig. 4.10. NTE happens in the shaded region where $V(90\text{K}) > V(295\text{K})$.

The anomalous NVTE and structural transition is strongly coupled to a first-order MI transition T_{MI} that is marked by a jump in the basal plane resistivity ρ_{ab} , as shown in Fig. 4.11. The resistance is plotted on a logarithmic scale versus temperature. Upon Cr doping, the T_{MI} decreases dramatically: For $x = 0$, the metal-insulator transition occurs at $T_{MI} = 357$ K and when $x = 0.032$ T_{MI} drops to 284 K. With further Cr doping, T_{MI} decreases further, such that for $x = 0.092$ the metallic phase is retained down to $T_{MI} = 81$ K. This continuous decrease of T_{MI} with the increasing Cr doping is directly related to the suppression of the structural distortion discussed above. The bandwidth W in this system depends critically on the Ru

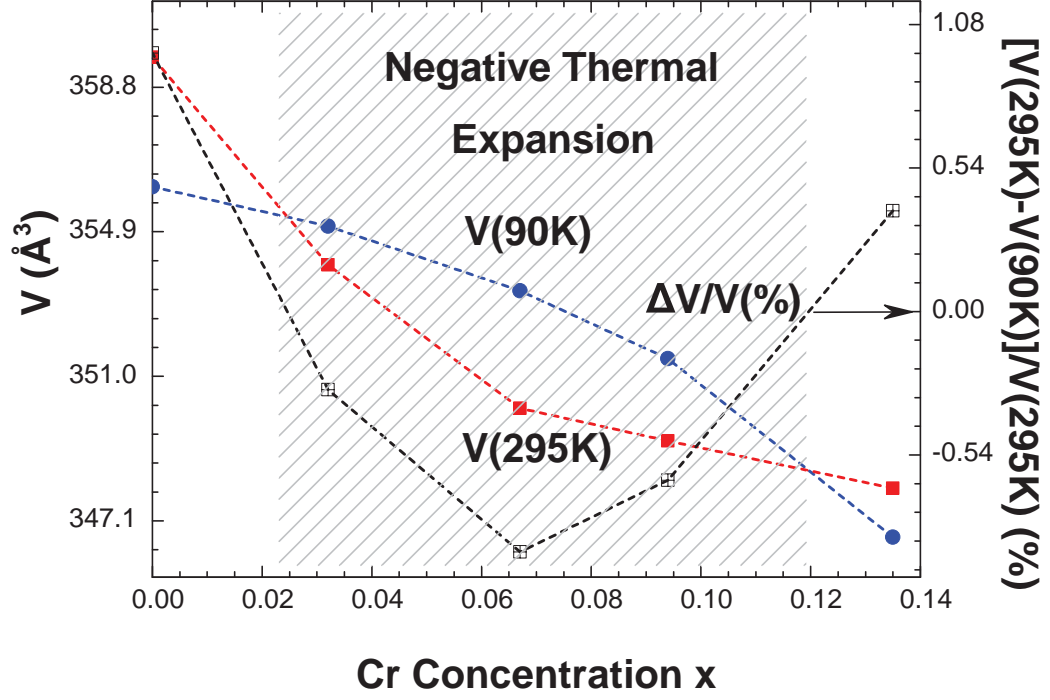


Figure 4.10: Unit cell volume V for $T = 90\text{ K}$ and 295 K , and thermal expansion ratio $[V(295\text{K}) - V(90\text{K})]/V(295\text{K})$ (right scale) for $0 \leq x \leq 0.135$.

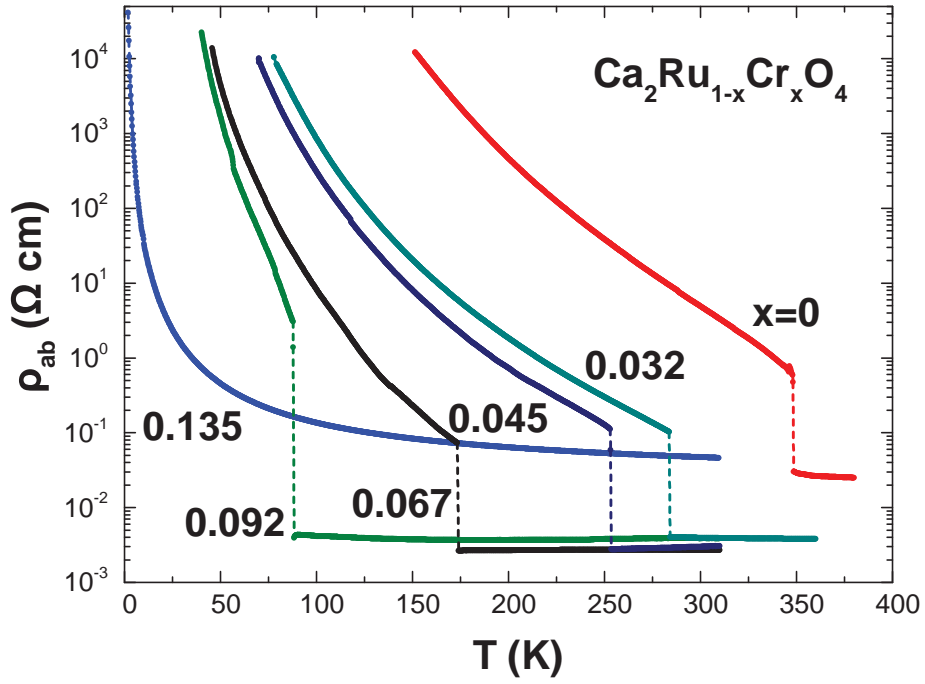


Figure 4.11: Temperature dependences of the ab-plane resistivity ρ_{ab} for $\text{Ca}_2\text{Ru}_{1-x}\text{Cr}_x\text{O}_4$ with $0 \leq x \leq 0.135$.

- O - Ru bond angle distortion. If we suppose there is a critical distortion angle where the MI transition happens, Cr doping suppresses the distortion in the system while cooling increases this distortion. Thus, increased Cr doping requires lower temperature to achieve this critical angle, which means the MI transition happens at lower temperature. The colossal change of T_{MI} can be interpreted as a competition between these two phenomena. These two effects rigorously compete, but Cr doping prevails eventually, thus, the overall disappearance of T_{MI} when Cr is higher than 13.5% can be seen in Fig. 4.11, simultaneous with both the disappearance of the orthorhombic distortion (see Fig. 4.8), and the return of the thermal expansion $\Delta V/V$ to normal behavior (see Fig. 4.10). Clearly, the anomalous NVTE is strongly coupled to the onset of orbital ordering. After T_{MI} is suppressed, the system shows insulating behavior at low temperature, which means the energy gap is still open. Compared to other dopants such as La [188, 204] or Sr [201, 205], the impact of Cr doping on $\rho(T)$ is profoundly different: Cr substitutes on Ru site while La and Sr both occupy a Ca site. High concentrations of La or Sr make the system metallic, but rich Cr doping makes the system an insulator at low temperature due to suppression of the metal-insulator transition.

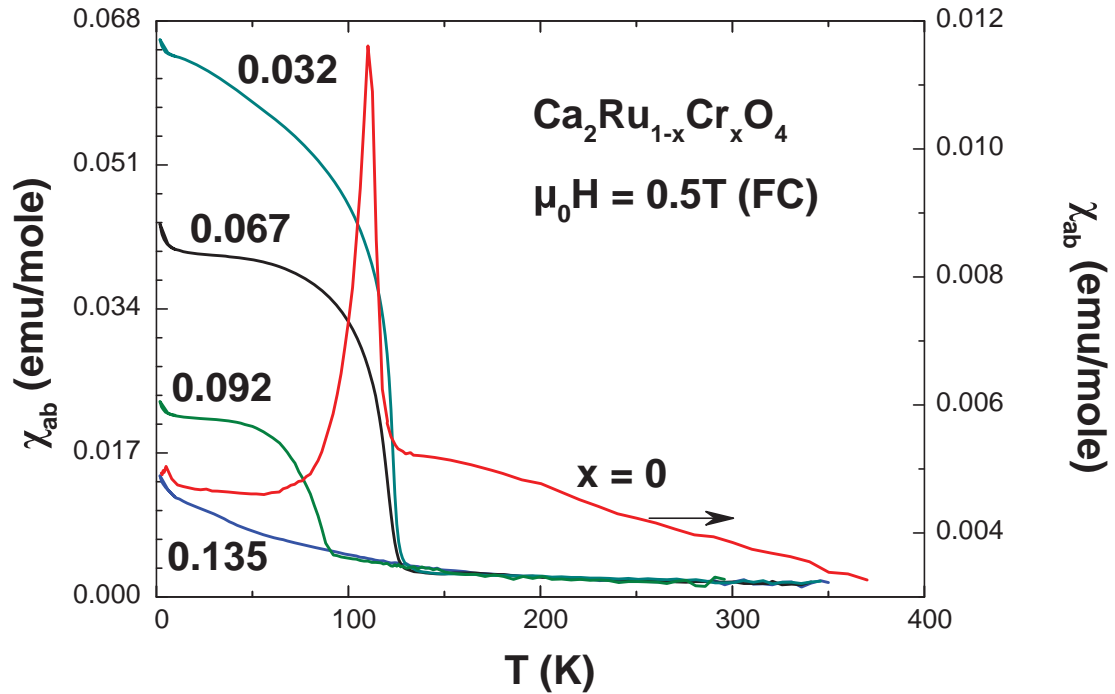


Figure 4.12: The magnetic susceptibility χ_{ab} at applied field $\mu_0 H = 0.5$ T for $\text{Ca}_2\text{Ru}_{1-x}\text{Cr}_x\text{O}_4$ with $0 \leq x \leq 0.135$.

The stability of the AFM state is also critically dependent upon both the Ru-O1-Ru bond angle θ and a concomitant elongation of the apical Ru-O2 distance, which undergo similar, finite shifts at only modest Cr doping levels (Fig. 4.9). In particular, the magnetic critical temperature $T_C(x)$ slowly increases and peaks at 130 K near $x = 0.067$. Moreover, the positive Curie-Weiss temperature CW estimated from high-

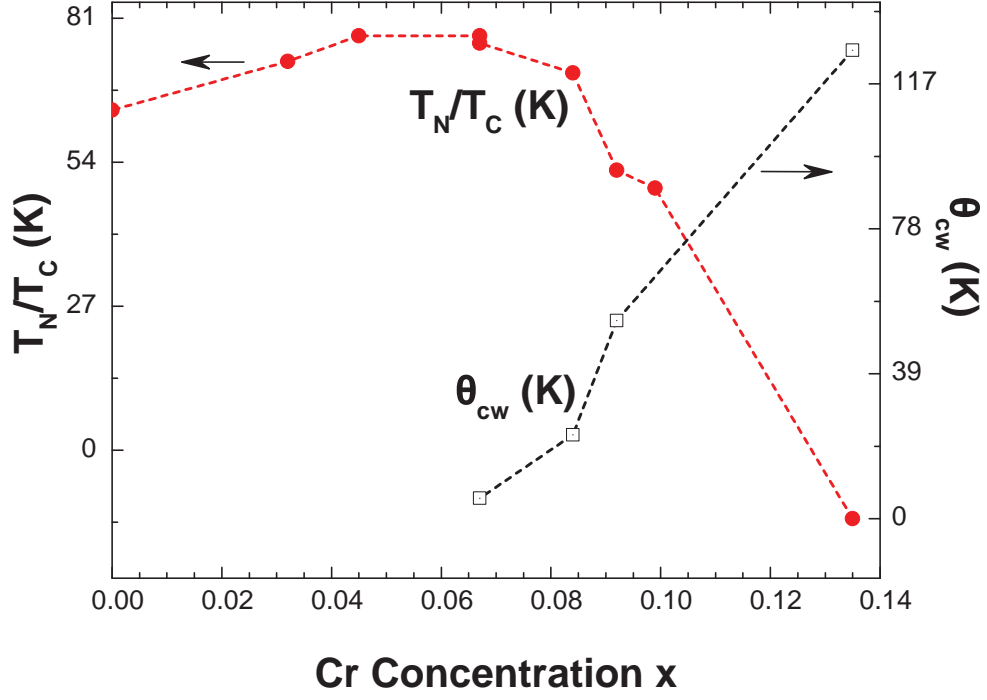


Figure 4.13: T_N , T_C and Curie-Weiss temperature Θ_{CW} for $\text{Ca}_2\text{Ru}_{1-x}\text{Cr}_x\text{O}_4$ with different x .

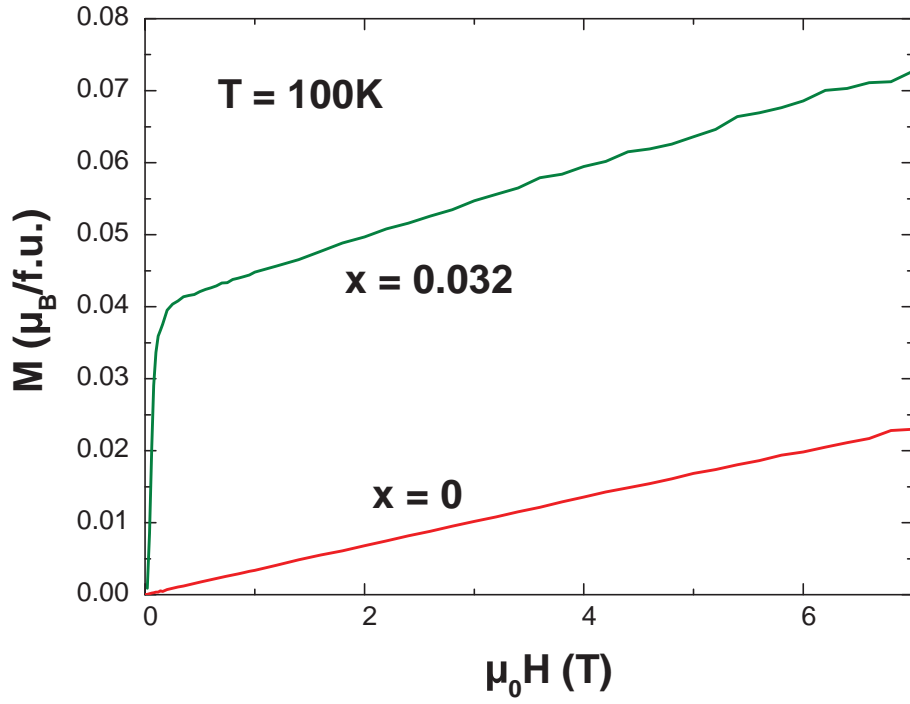


Figure 4.14: The isothermal magnetization $M(H)$ at 100 K for representative compositions $x = 0$ and 0.032.

T fits of magnetic data increases with x , indicating an increasing FM character of the volume-averaged exchange interaction (see Fig. 4.13). Given the low saturation moment ($\sim 0.04 \mu_B/\text{f.u.}$ for $x = 0.032$) and the strong magnetic field dependence of $M(H)$ shown in Fig. 4.14, the ferromagnetic behavior is likely a result of spin canting in an otherwise collinear AFM spin arrangement. The T_C peak is followed by a strong downturn and suppression of magnetic order near the critical composition $x_{cr} = 0.135$ (shown in Fig. 4.12).

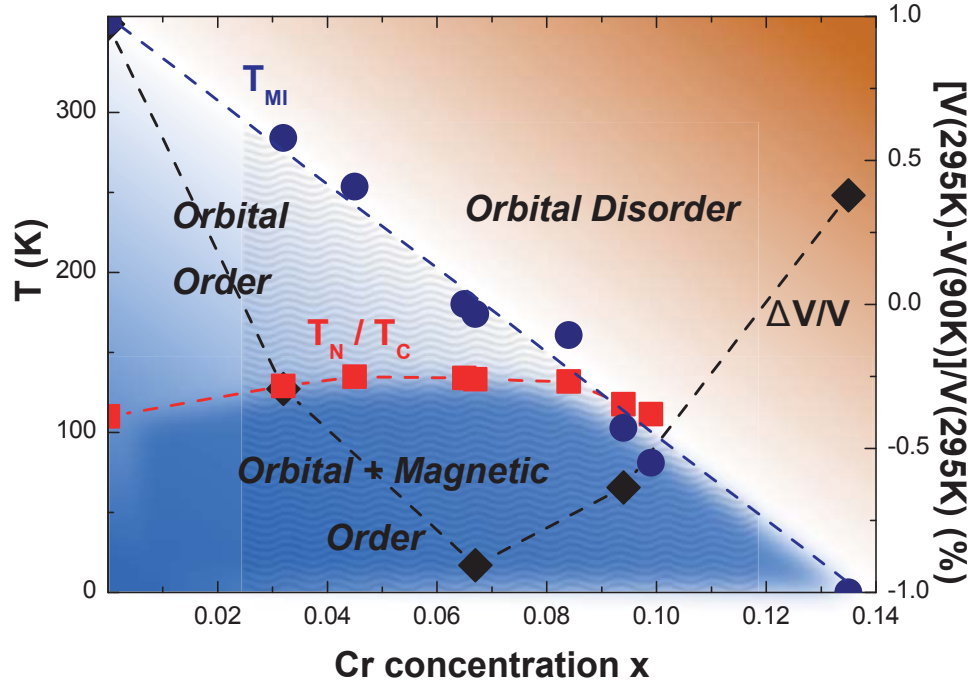


Figure 4.15: The T-x phase diagram summarizing observed phase transitions and phase types. Right scale shows the Cr concentration (x) dependence of the thermal expansion ratio $\Delta V/V$. Note that the hatched region represents NVTE.

The extraordinary, strong dependence of the structural, magnetic and electrical properties of $\text{Ca}_2\text{Ru}_{1-x}\text{Cr}_x\text{O}_4$ on Cr content can be summarized in the T-x phase diagram as follows (see Fig. 4.15). The drastic decrease in T_{MI} observed with increasing Cr doping in $\text{Ca}_2\text{Ru}_{1-x}\text{Cr}_x\text{O}_4$ closely tracks the rapidly weakening orthorhombicity, as well as the reduced tilt and elongation of RuO_6 octahedra (Figs. 4.8 and 4.9) as x increases; the eventual disappearance of T_{MI} is concomitant with vanishing orthorhombicity for $x_{Cr} = 0.135$ (Fig. 4.11). Moreover, the increasing Ru-O2 bond distance and Ru-O1-Ru bond angle (Fig. 4.9) destabilize the collinear AFM state, which, in turn, lead to weak Ferromagnetic behavior and spin canting. A competition between AFM and FM couplings persists to $x < 0.135$, but T_C decreases rapidly as x increases above 0.06 (Fig. 4.12). Consequently, V abruptly expands on cooling just below T_{MI} , where orbital ordering occurs, and further expands at T_C . Higher Cr doping relaxes the orthorhombic distortion that, via a highly unusual spin-lattice

coupling, weakens the AFM state, and results in an extraordinary increase in volume on cooling [147, 148].

4.3 $\text{Ca}_2\text{Ru}_{1-x}\text{Mn}_x\text{O}_4$

4.3.1 Negative Thermal Expansion in $\text{Ca}_2\text{Ru}_{1-x}\text{Mn}_x\text{O}_4$

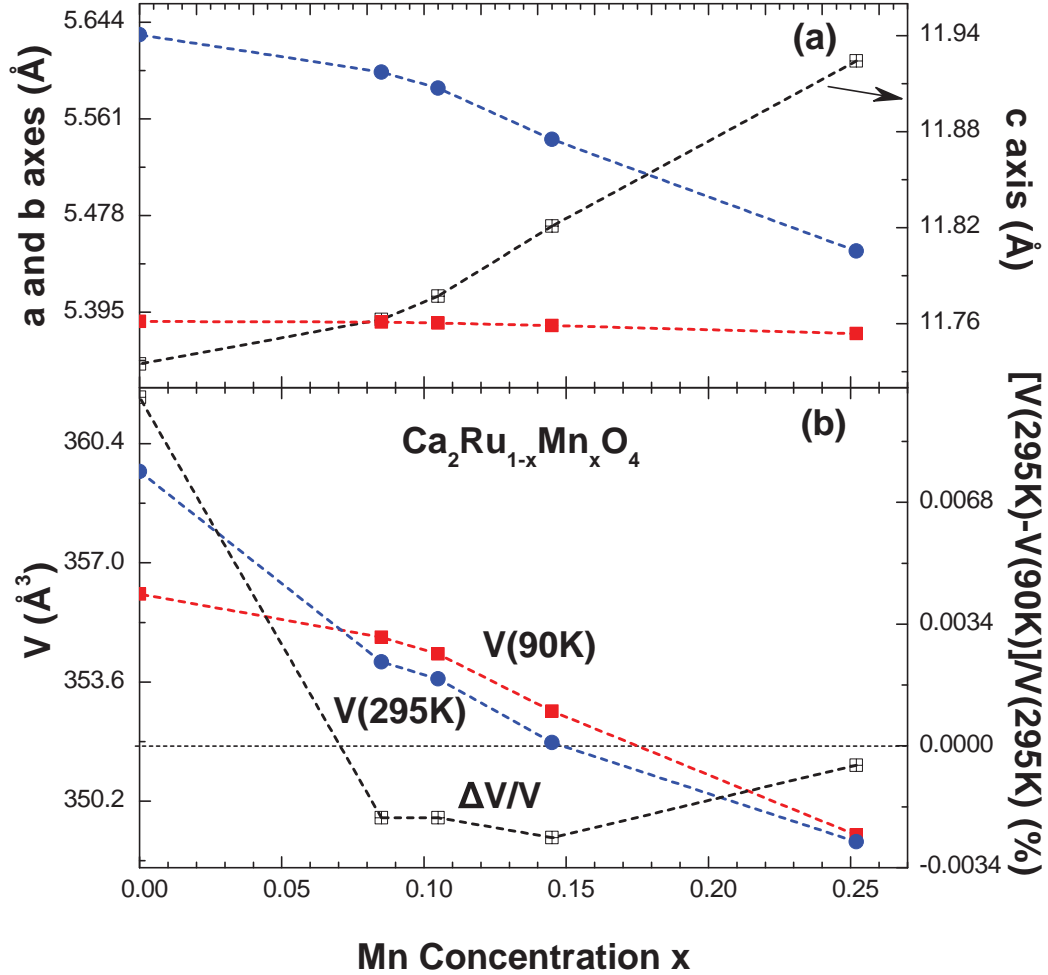


Figure 4.16: For $\text{Ca}_2\text{Ru}_{1-x}\text{Mn}_x\text{O}_4$ with $0 < x < 0.25$, x dependence of (a) the lattice parameter a -, b - and c -axis (right scale) at $T = 90$ K and (b) unit cell volume V and thermal expansion ratio $\Delta V/V = [V(295\text{K}) - V(90\text{K})]/V(295\text{K})$ (right scale). Note that $\Delta V/V$ is only for $90 \text{ K} \leq T \leq 295 \text{ K}$, and this value is much greater for $90 \text{ K} \leq T \leq T_{MI} \sim 380 \text{ K}$.

Similar with Cr doping [147, 148], Mn doping preserves the low temperature orthorhombic symmetry ($Pbca$) but weakens the orthorhombic distortion by reducing the difference between the a - and b -axis ($[b-a]$ changes from 0.25 \AA for $x = 0$ to 0.07 \AA for $x = 0.25$) as shown in Fig.4.16(a). The previous section shows that the

structural distortion evidenced by flattening of RuO_6 octahedron along the c-axis can be associated to a Jahn-Teller distortion [35, 147, 187]. The increasing c-axis lattice parameter with higher Mn concentration clearly indicates that Mn dopant weakens this distortion. The weakening structural distortion is also reflected by the relaxation of the Ru-O1-Ru bond angle and suppression of the octahedral tilt angle Ru-Ru-O2. More importantly, the unit cell volume V for $x > 0.085$ is larger at 90 K than at 295 K, indicating NTE; but the NTE diminishes when x approaches 0.25, as shown in Figs.4.16(b).

4.3.2 Temperature dependence of the $\text{Ca}_2\text{Ru}_{1-x}\text{Mn}_x\text{O}_4$

We now focus on the coupling between the NTE and MI transition at T_{MI} and the magnetic order at T_N by examining two sets of representative data for $x = 0.10$ and 0.25.

At $x = 0.10$, strong NTE not only along the b-axis, but also along the a-axis (see Fig.4.17(a)), which gives rise to the overall negative volume thermal expansion (NVTE). The thermal expansion as a function of temperature can be described by the CTE discussed in Chap.1.3. Over the temperature range $90\text{K} \leq T \leq 430\text{K}$, the CTE is found to be $\alpha_b = -1.244 \times 10^{-4} \text{ K}^{-1}$ for the b-axis; it is striking that such as an uniaxial NTE is two orders of magnitude larger than that for classic NTE materials. There is a first-order phase transition in a temperature range of 375-395 K that leads to a low-T orthorhombic structure from a high-T tetragonal phase. This anomalous NVTE is strongly coupled to the onset of MI transition that occurs at $T_{MI} = 380 \text{ K}$ (ρ_{ab} is in Log scale), as shown in Fig.4.17(b) and (c). The coupling of the NTE to the MI transition and the magnetic order is obvious in that V rapidly expands below $T_{MI} = 380 \text{ K}$, and exhibits a weak yet well-defined anomaly near $T_N = 130 \text{ K}$, where the weak FM behavior takes place, as marked by the shaded area and the dashed line.

The sharpness of the phase transition at T_{MI} vanishes at $x = 0.25$ and the MI transition becomes so broadened that it cannot be well defined. The splitting of a- and b-axis lattice parameter illustrates the tetragonal-orthorhombic structural transition, which occurs at a much lower temperature, 225 K due to the weakening of the orthorhombicity at the higher Mn concentration (see Fig. 4.18(a)). Concomitantly, the NTE diminishes with nearly zero thermal expansion or $\Delta V/V < 0.1\%$ in a remarkably wide temperature range of 90K - 410K, as illustrated in Fig.4.18(b). The simultaneous disappearance of both T_{MI} and the NTE reinforces the unique, strong coupling between the orbital order and NVTE. More interestingly, nearly zero volume thermal expansion is observed in $x=0.25$ sample over a wide (320 K) temperature range, which constitutes a strong *Invar effect*. (e.g., the slight or nearly zero thermal expansion first observed in certain Ni-Fe alloys [206]). The Invar effect was also observed in another ruthenate compound SrRuO_3 , which has ferromagnetism caused by Ru 4d electrons and show the Invar effect below T_C at about 160K [207, 208]. However, the invar effect we found here in $\text{Ca}_2\text{Ru}_{1-x}\text{Mn}_x\text{O}_4$ is associated with structural change, in sharp contrast to the invar effect in SrRuO_3 with no structural transition and has

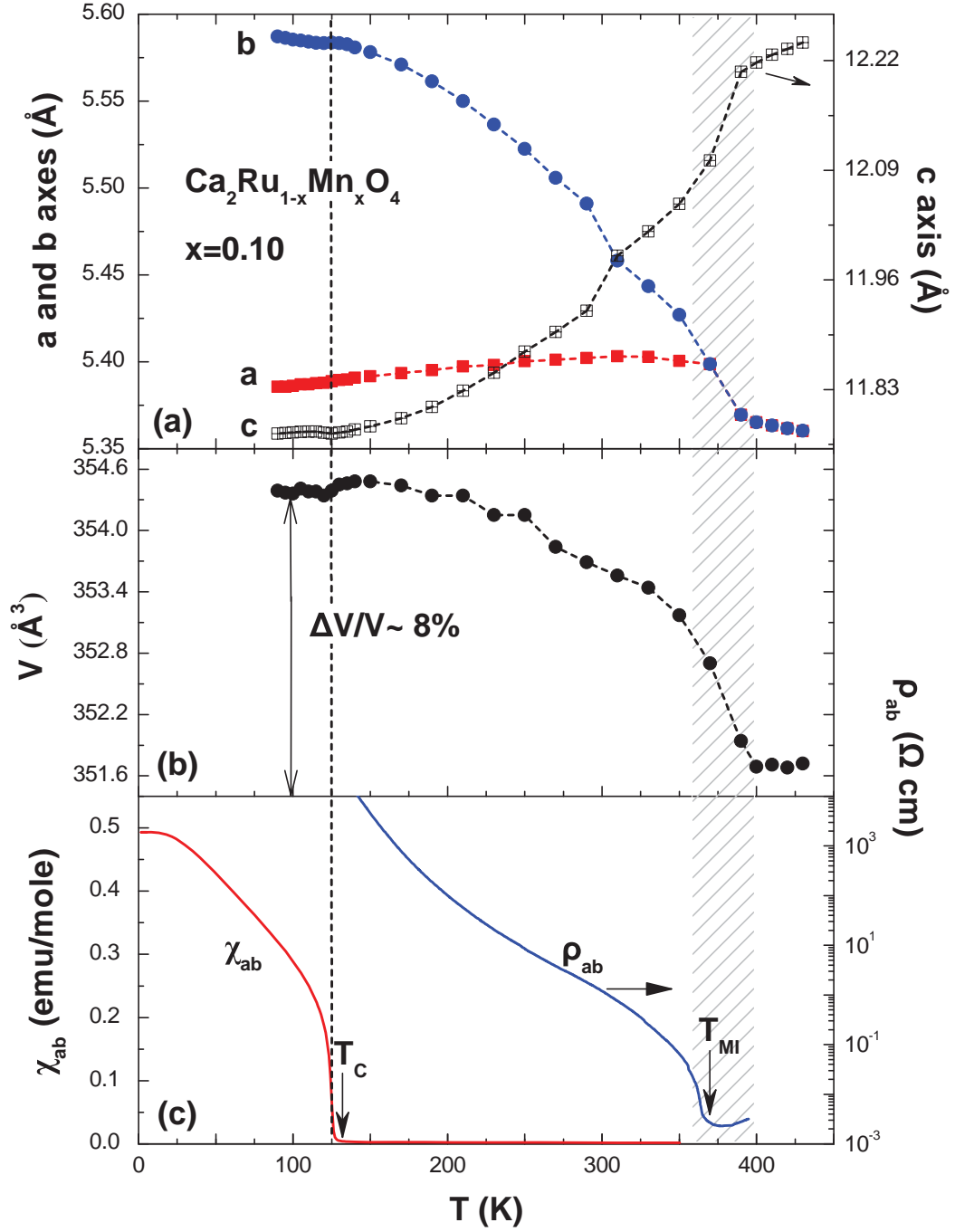


Figure 4.17: For $\text{Ca}_2\text{Ru}_{1-x}\text{Mn}_x\text{O}_4$ with $x = 0.10$, temperature dependences of (a) lattice parameters a -, b - and c -axis (right scale), (b) unit cell volume V and (c) magnetic susceptibility χ_{ab} at $\mu_0 H = 0.1$ T (field cooled) and ab -plane resistivity ρ_{ab} (right scale). The shaded area indicates the concomitant occurrence of the NTE and MI transition.

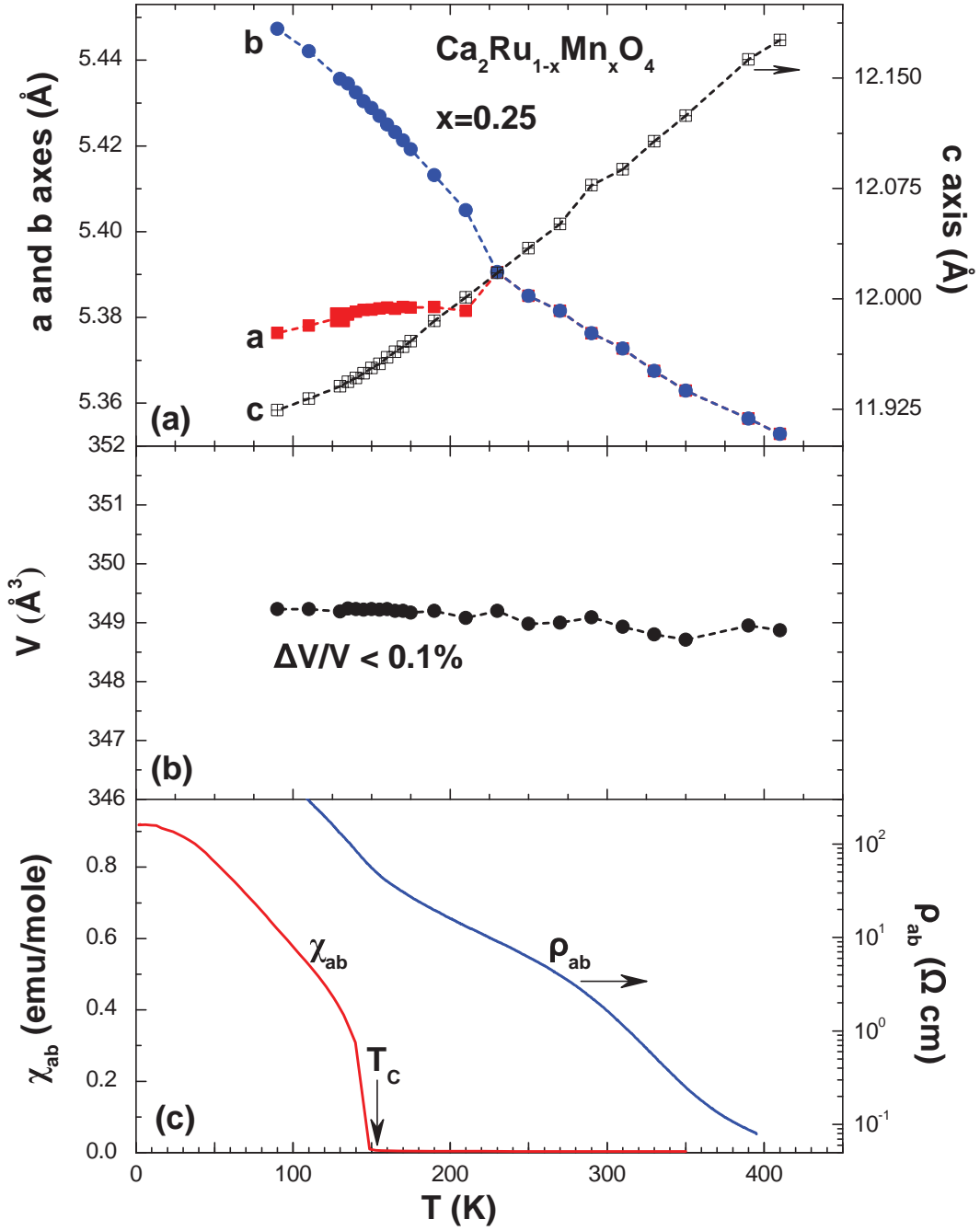


Figure 4.18: For $\text{Ca}_2\text{Ru}_{1-x}\text{Mn}_x\text{O}_4$ with $x = 0.25$, temperature dependences of (a) lattice parameters a -, b - and c -axis (right scale), (b) unit cell volume V and (c) the magnetic susceptibility χ_{ab} at $\mu_0 H = 0.1$ T (field cooled) and the ab -plane resistivity ρ_{ab} (right scale).

the same crystal structure over the whole temperature range [207]. The Invar effect has very broad applications in electronic devices and aerospace industry [209, 210].

4.3.3 Mn concentration dependence of the $\text{Ca}_2\text{Ru}_{1-x}\text{Mn}_x\text{O}_4$

If we look at the physical properties at several representative Mn concentrations, it is clear that the MI transition increases from $T_{MI} = 357$ K for $x = 0$ to around 380 K for $x = 0.085$ and 0.10, but the sharpness of the MI transition diminishes for $x = 0.14$ and vanishes for $x = 0.25$ (see Fig. 4.19). Since the MI transition is primarily due to the structural phase transition between the high-T tetragonal to the low-T orthorhombic distortion, the broadening of the MI transition is more likely due to the diminishing of the structural phase transition as Mn doping readily reduces the difference between the a- and b-axis evident in Fig. 4.16. It is remarkable that single crystals of Ca_2RuO_4 [35, 36] and $\text{Ca}_2\text{Ru}_{1-x}\text{Cr}_x\text{O}_4$ [147, 148] pulverize themselves when undergoing the violent tetragonal-orthorhombic phase transition, a unfavorable feature that is incommodious to measurements and any possible applications of the materials; in contrast, single crystals of $\text{Ca}_2\text{Ru}_{1-x}\text{Mn}_x\text{O}_4$ with $x > 0.1$ undergo a nonviolent, second-order phase transition, while retaining the other favorable underlying physical properties existent in $\text{Ca}_2\text{Ru}_{1-x}\text{Cr}_x\text{O}_4$ [147, 148]. This makes $\text{Ca}_2\text{Ru}_{1-x}\text{Mn}_x\text{O}_4$ more desirable for fundamental studies and potential applications. This second-order phase transition at T_{MI} is also confirmed by peaks in specific heat $C(T)$, which are narrowly separated, as shown in Fig. 4.22.

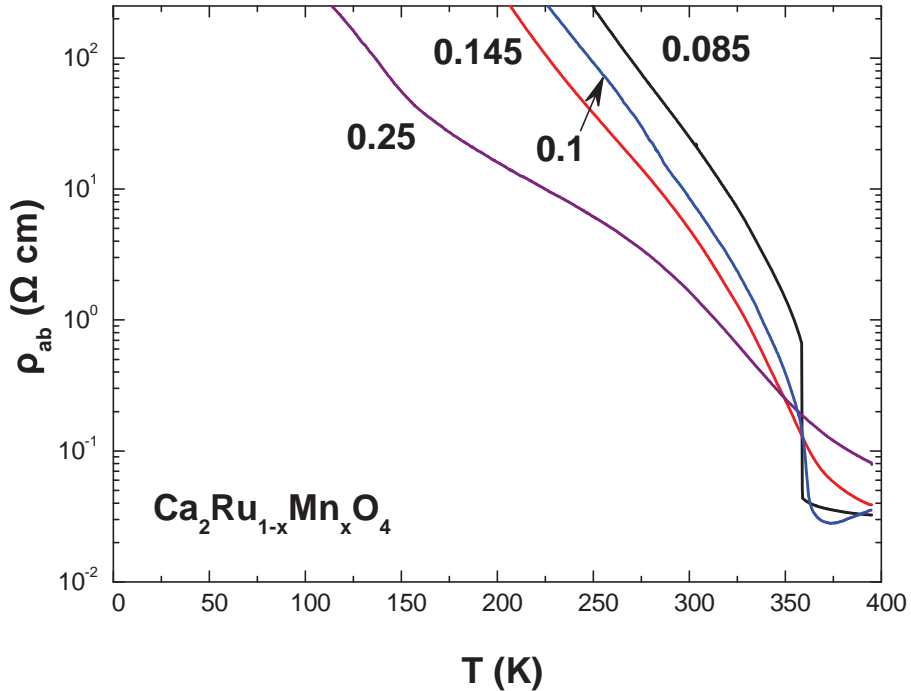


Figure 4.19: Temperature dependence of the ab-plane resistivity ρ_{ab} for $\text{Ca}_2\text{Ru}_{1-x}\text{Mn}_x\text{O}_4$ with $0 < x < 0.25$.

On the other hand, the magnetic ordering temperature T_N systematically rises with increasing x from $T_N = 120$ K for $x = 0.085$ to 130 K for $x = 0.10$ and eventually 150 K for $x = 0.25$, as illustrated in Fig. 4.20 and the inset in Fig. 4.22. The magnetic susceptibility deviates from Curie-Weiss behavior when $x < 0.145$. However, the Curie-Weiss temperature θ_{CW} increases with x and becomes positive when $x=0.25$, indicating an increasing FM character. The systematic change of T_N with x further confirms the homogeneity of the samples studied.

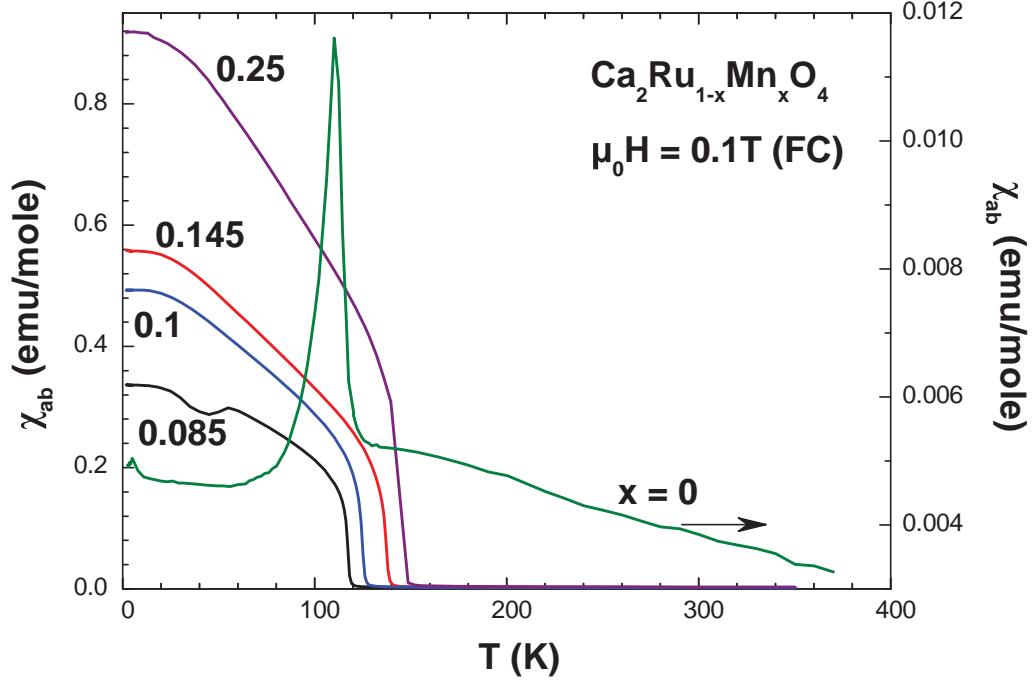


Figure 4.20: Temperature dependence of the magnetic susceptibility χ_{ab} for $\text{Ca}_2\text{Ru}_{1-x}\text{Mn}_x\text{O}_4$ with $0 < x < 0.25$.

Interestingly, Mn doping induces a metamagnetic transition at H_C and a sizable order moment μ_0 ; with increasing x , H_C decreases from 5 T for $x = 0.085$ to 2 T for $x = 0.25$ whereas μ_0 eventually amounts up to $0.2 \mu_B/\text{f.u.}$ for $x = 0.25$, as shown in Fig. 4.21. The metamagnetism indicates a spin canting existent in an AFM background, which explains the weak FM behavior seen in Fig. 4.20. The order along c -axis preserves AFM behavior. This anisotropic nature of this magnetic ordering can be traced back to the quasi-2D structure of Ca_2RuO_4 [36, 211]. The in-plane ferromagnetic coupling can be explained by the double-exchange mechanism, in which the spins on near-neighbor Ru/Mn ions are aligned to promote delocalization of carriers. The out-of-plane AFM coupling is contributed by the interaction between the filled t_{2g} - t_{2g} orbitals along the c -axis [187].

In Fig. 4.22, we show results of specific heat $C(T)$ for $\text{Ca}_2\text{Ru}_{1-x}\text{Mn}_x\text{O}_4$ with $0.085 < x < 0.25$ for $0 < T < 400$ K. In all cases, the electronic specific heat coefficients γ is approaching zero, indicating an energy gap at the Fermi level in the ground state consistent with the nature of the insulating state. The main magnetic peak observed

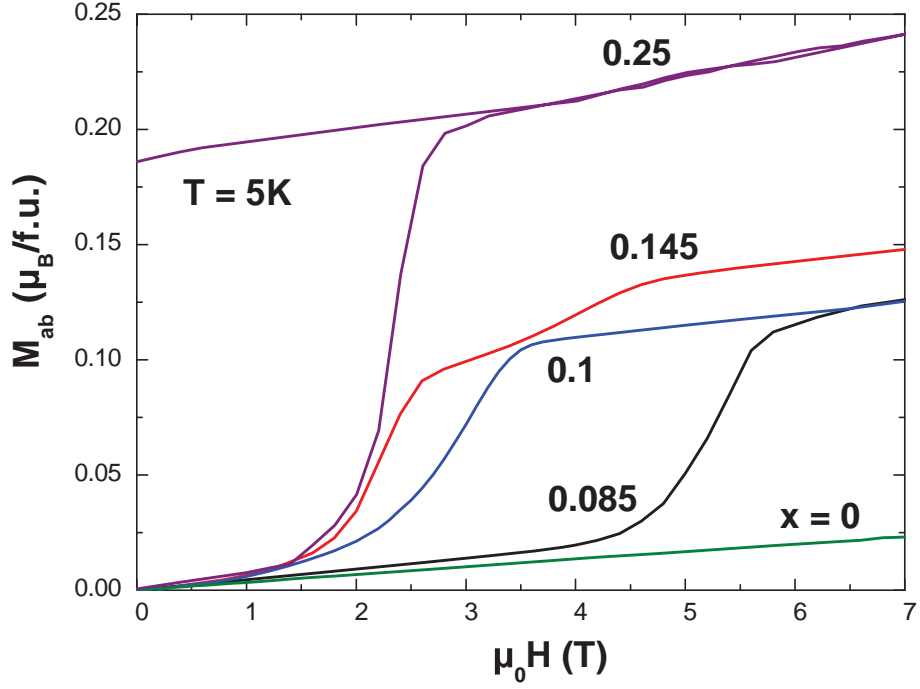


Figure 4.21: The isothermal magnetization M_{ab} for $\text{Ca}_2\text{Ru}_{1-x}\text{Mn}_x\text{O}_4$ with $0 < x < 0.25$.

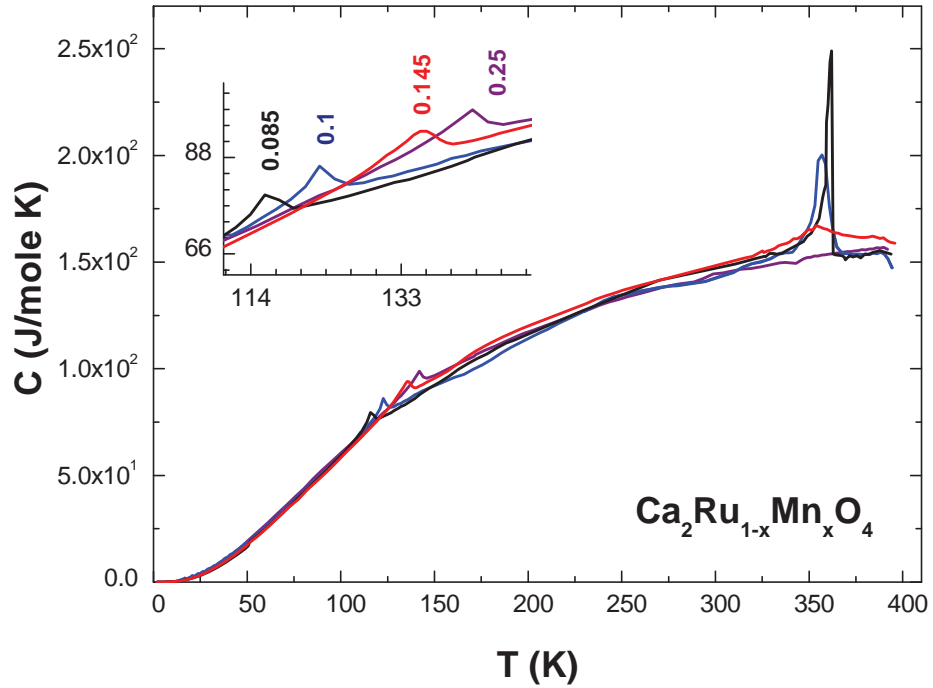


Figure 4.22: Temperature dependence of the specific heat $C(T)$ for $\text{Ca}_2\text{Ru}_{1-x}\text{Mn}_x\text{O}_4$ with $0 < x < 0.25$. Inset: enlarged $C(T)$ near T_N . Note that T_N and the order moment increase with x .

in $C(T)$ (see Fig. 4.22 inset) closely responds to T_C in $\chi_{ab}(T)$ and increases with x . The large, sharp peak at the higher temperature in $C(T)$ is clearly due to the MI transition or orbital order at T_{MI} , consistent with the first-order transition [212]. It has been found that the sharp heat capacity change usually indicate where a first order transition happens although the temperature decay at first order transition cannot be satisfactorily fitted using single decay constant as the PPMS software does [213,214]. The weaker, broadened peak for $x > 0.10$ characterizes a change from first order to second order transition, which is consistent with the weakening of T_{MI} in basal plane resistivity.

In single layered Ca_2RuO_4 system, the t_{2g} bands split into d_{xy} band and d_{xz}, d_{yz} bands because of the Jahn-Teller distortion. Theoretical study shows the metal-insulator transition in this system is driven by the competition of two mechanisms: A small $W_{xz/yz}/W_{xy}$ bandwidth ratio enhances the occupation of the d_{xz}, d_{yz} orbitals while a large crystal-field splitting favors d_{xy} orbital order [215]. Mn doping readily weakens and eventually removes the Jahn-Teller distortion, thus the existence of d_{xy} orbital order and T_{MI} . Moreover, the increasing Ru-O1-Ru bond angle destabilizes the collinear AFM state [216], which, in turn, leads to the weak FM behavior and spin canting. That NVTE does not occur in pure Ca_2RuO_4 , suggests that doping on the Ru sites can soften the lattice and unlock strongly buckled RuO_6 octahedra [147]. At the same time, Mn doping also relaxes the orthorhombic distortion via an unusual spin lattice coupling and eventually results in an extraordinary increase in volume on cooling.

4.4 $\text{Ca}_2\text{Ru}_{1-x}\text{Fe}_x\text{O}_4$

4.4.1 Negative Thermal Expansion in $\text{Ca}_2\text{Ru}_{1-x}\text{Fe}_x\text{O}_4$

Substituting Fe for Ru in Ca_2RuO_4 also effectively weakens the orthorhombic distortion, and induces the NTE. Fig. 4.23 register the lattice parameters for $0.08 < x < 0.22$ taken at 90 K and 295 K. Similar to that for Cr (Fig. 4.10) and Mn doping (Fig. 4.16), the effect of the NTE nearly vanishes at $x = 0.22$ where the orthorhombic distortion is considerably reduced and T_{MI} is no longer well defined. a-axis and b-axis have a tendency to be more close at higher Fe concentration.

Comparing these three different dopant discussed above, we can find the NTE effect is most significant with Cr doping and becomes weaker with the increase of atomic number. NTE of $\text{Ca}_2\text{Ru}_{1-x}\text{Cr}_x\text{O}_4$ peaks around $x=0.07$ and goes back to normal thermal expansion at $x=0.12$ (Fig. 4.10). For $\text{Ca}_2\text{Ru}_{1-x}\text{Mn}_x\text{O}_4$, the peak position increased to $x=0.10$ and didn't overcome until $x=0.25$ (Fig. 4.16). In $\text{Ca}_2\text{Ru}_{1-x}\text{Fe}_x\text{O}_4$, the peak keep moving up to $x=0.18$ and no evidence of crossing to positive until $x=0.22$ (Fig. 4.23). One possible assumption is that it may due to the difference of ionic size, which will change the M-O bond length and the structure may be more relaxed with larger ionic radii [217,218]. More 3d transition metal element dopants need to be investigated to verify this assumption.

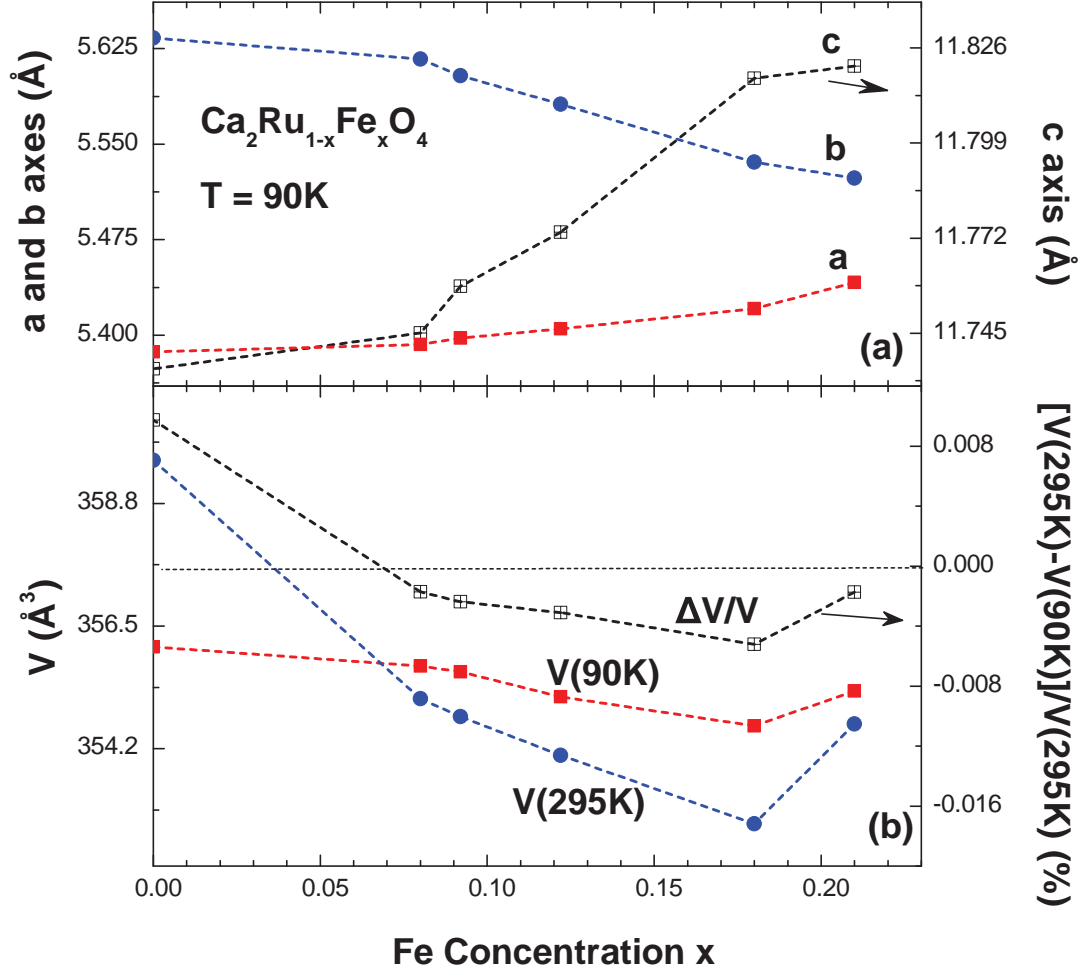


Figure 4.23: For $\text{Ca}_2\text{Ru}_{1-x}\text{Fe}_x\text{O}_4$ with $0 < x < 0.22$, x dependence of (a) the lattice parameters a -, b - and c -axis (right scale) and (b) unit cell volume V at $T = 90\text{ K}$ and 295 K ; thermal expansion ratio $\delta V/V = [V(295\text{K})-V(90\text{K})]/V(295\text{K})$ for $0 \leq x \leq 0.22$.

4.4.2 Temperature dependence of the $\text{Ca}_2\text{Ru}_{1-x}\text{Fe}_x\text{O}_4$

More detailed data for $x = 0.08$ as a function of temperature collected over $1.7 < T < 450\text{ K}$ exhibit the strong NTE along b -axis but a much weaker temperature dependence of the a -axis (see Fig. 4.24(a)), and an overall thermal expansion with $\Delta V/V \sim 0.8\%$ on cooling over $90 < T < 390\text{ K}$ (see Fig. 4.24). It is now no longer a surprise that the onset of the NTE occurs simultaneously with the MI transition at T_{MI} that is characterized by a strong anomaly in the specific heat $C(T)$ (Fig. 4.24(b)) and $\rho_{ab}(T)$ (Fig. 4.24(c), right scale) at $T_{MI} = 380\text{ K}$. It is noted that the NTE peaks near 150 K below which V starts to contract on cooling (Fig. 4.24(b)), and there is no obvious lattice anomaly near the magnetic order at $T_N = 120\text{ K}$, in contrast to the behavior seen in Cr and Mn doped Ca_2RuO_4 . This difference may be associated with unusual magnetic properties absent in Cr and Mn doped Ca_2RuO_4 .

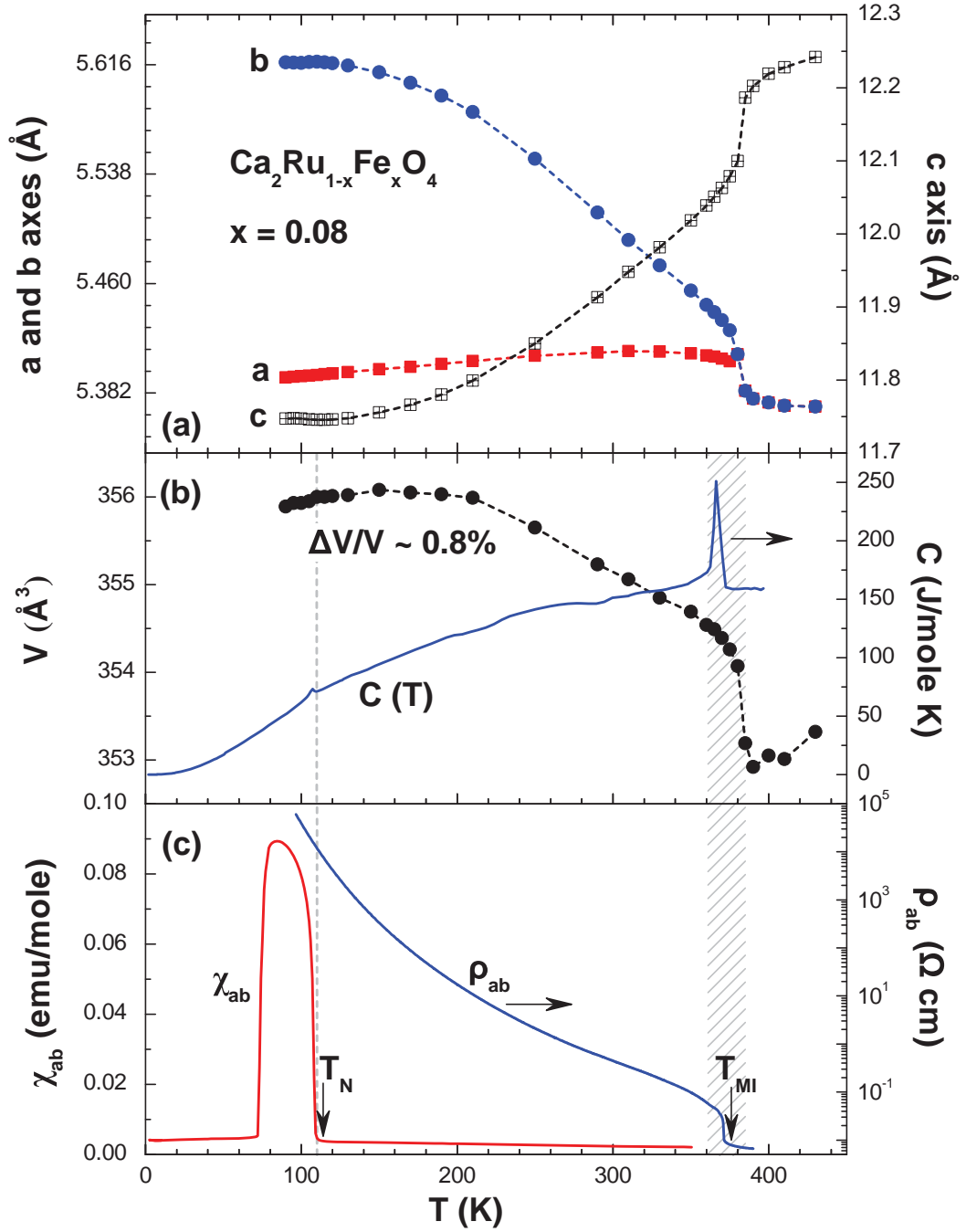


Figure 4.24: For $\text{Ca}_2\text{Ru}_{1-x}\text{Fe}_x\text{O}_4$ with $x = 0.08$, temperature dependences of (a) lattice parameters a -, b - and c -axis (right scale), (b) lattice volume V and specific heat $C(T)$ (right scale) and (c) magnetic susceptibility χ_{ab} at $\mu_0 H = 0.1$ T (field cooled) and ab -plane resistivity ρ_{ab} (right scale).

As seen in Fig. 4.24(c), χ_{ab} for $x = 0.08$ shows a peak at T_N seldom seen in other antiferromagnets.

4.4.3 Fe concentration dependence of the $\text{Ca}_2\text{Ru}_{1-x}\text{Fe}_x\text{O}_4$

Fig. 4.25 shows the temperature dependence of resistivity and specific heat at zero magnetic field for $\text{Ca}_2\text{Ru}_{1-x}\text{Fe}_x\text{O}_4$ with different x . The first order MI transition has already become a second order transition when $x = 0.08$, and continuously become less sharper with higher Fe doping. This change also can be evidenced by the suppression of the corresponding peaks in heat capacity curves.

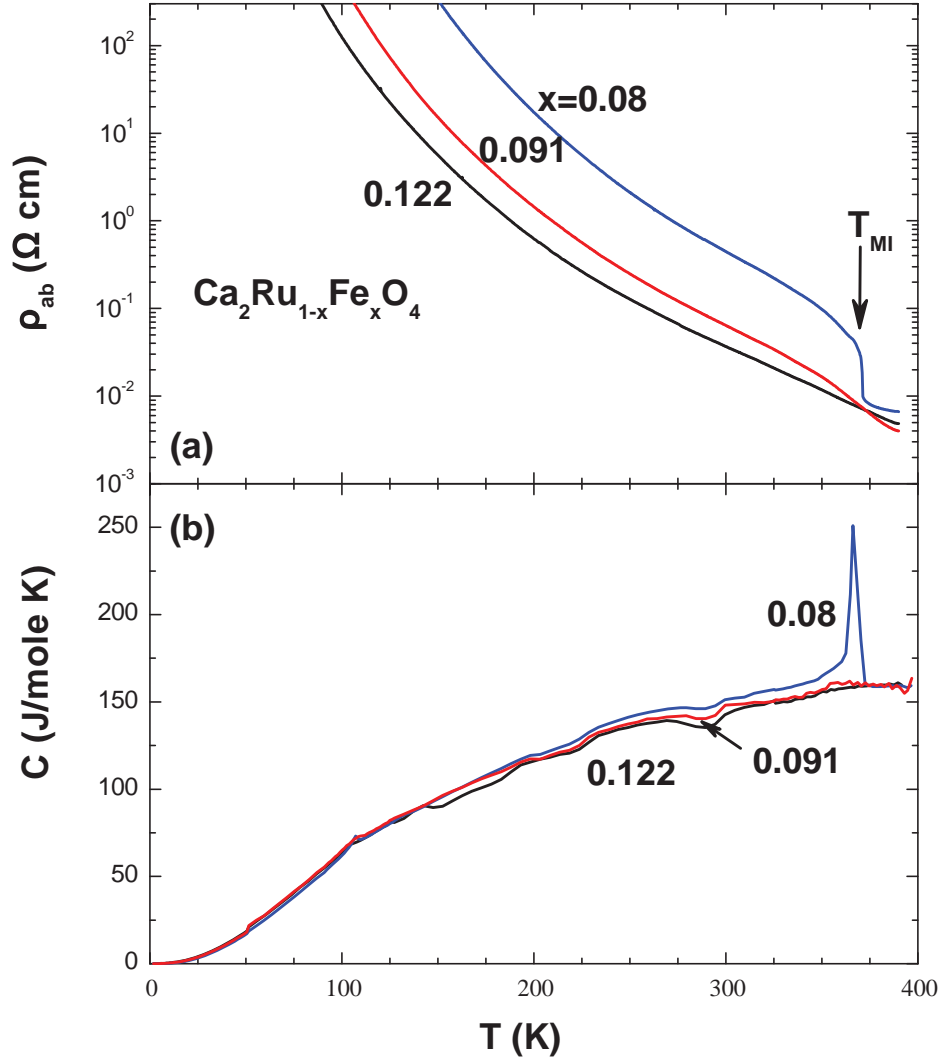


Figure 4.25: For $\text{Ca}_2\text{Ru}_{1-x}\text{Fe}_x\text{O}_4$ with $x = 0.08, 0.091$ and 0.122 , temperature dependences of (a) ab-plane resistivity ρ_{ab} , (b) specific heat $C(T)$.

Fig. 4.26 displays the magnetization M on ab plane as a function of temperature for $\text{Ca}_2\text{Ru}_{1-x}\text{Fe}_x\text{O}_4$ with different dopant concentration. T_N decreases significantly

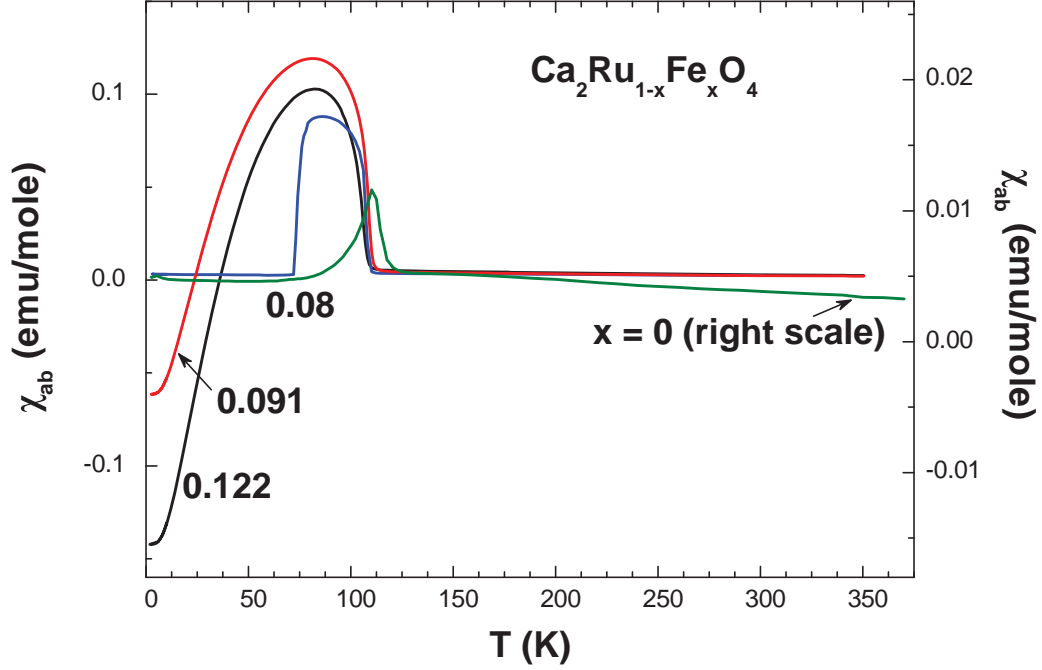


Figure 4.26: Temperature dependence of the magnetic susceptibility χ_{ab} at $\mu_0 H = 0.1$ T (field cooled) for $\text{Ca}_2\text{Ru}_{1-x}\text{Fe}_x\text{O}_4$ with $x = 0$ (right scale), 0.08, 0.091 and 0.122.

with the increment of Fe%. The most striking phenomenon in $\text{Ca}_2\text{Ru}_{1-x}\text{Fe}_x\text{O}_4$ is a magnetization reversal below 25 K under field-cooled (FC) conditions when $\text{Fe}\% > 0.08$. There is a "diamagnetic" state right below T_N followed by a negative magnetization region that becomes more and more negative with higher Fe%, which suggest this negative magnetic moment part may come from the Fe site. To understand this result, magnetic interactions of Fe cations with Ru cations and of Ru cations among themselves can be considered, which then give rise to five distinct interactions [141, 219]. These interactions make it possible to obtain multiple magnetic effects. The Ru-O-Ru interaction is a very strong single interaction, giving rise to a net magnetic moment with a canted spin arrangement. In addition, the Ru-O-Fe interaction also exists as well, with comparable or even greater magnitude. These two moments are antiparallel to each other but with a different temperature dependence, could give rise to this compensation effect of negative magnetization [219, 220]. A more detailed understanding of this behavior requires more accurate knowledge of the two magnetic interactions. Neutron diffraction with various temperature could be a good way to accurately determine these two magnetic sites.

4.4.4 Magnetization Reversal in $\text{Ca}_2\text{Ru}_{1-x}\text{Fe}_x\text{O}_4$

This magnetization reversal in the basal plane below 25 K is not observed in other doped Ca_2RuO_4 samples. It is clear that the FC magnetization shows an abrupt transition at $T_N = 110$ K and then undergoes a rapid drop below $T_D = 80$ K, and anomalously becomes negative at around 25 K, unambiguously signaling a rotation of

the magnetic moment that is in opposition to the magnetic field [221]. This behavior is robust, however, it is not observed under zero-field-cooled (ZFC) condition, which instead remains a typical AFM behavior (seen Fig. 4.27). In the entire temperature range measured, the ZFC magnetization shows reduced moment; there is a slightly broadened AFM ordering peak around $T_N = 110$ K.

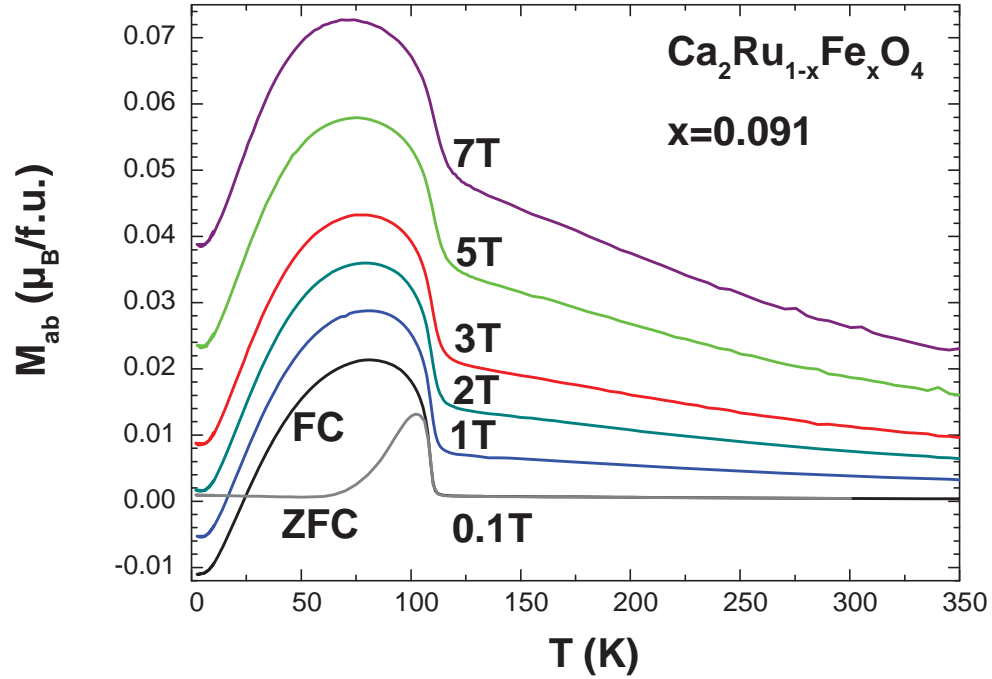


Figure 4.27: Temperature dependence of the magnetization M_{ab} at $B = 0.1\text{T}$, 1T , 2T , 3T , 5T and 7T (field cooled) for $\text{Ca}_2\text{Ru}_{1-x}\text{Fe}_x\text{O}_4$ with $x = 0.091$.

The diamagnetic state is robust and exists even when the external magnetic field goes up to 1T . As the magnetic field increases, the ferromagnetic response becomes stronger. The diamagnetic state diminishes and eventually vanishes at $B = 2\text{T}$, indicating that the magnetic moment parallel with B or the ferromagnetic moment is dominant although the downturn of M below T_D still remains. This downturn remains in 3T , 5T and 7T FC magnetization curves, which suggests that even a huge external magnetic field up to 7T still can not align all the magnetic components that are in opposition to the magnetic field. Also, with the increment of magnetic field, T_N keep increasing from 110 K at 0.1T to 125 K at 7T .

Fig. 4.28 (a) demonstrates the isothermal magnetization as a function of magnetic field B parallel to the basal plane at $T=5\text{K}$, 30K , 60K , 80K , 100K and 120 K in $\text{Ca}_2\text{Ru}_{1-x}\text{Fe}_x\text{O}_4$ with $x=0.091$. M_{ab} shows a significant slope change as T rises. It appears to be more "saturated", suggesting a development of weak ferromagnetic component with increasing T [221]. A linear field dependence at higher fields may indicate an AFM state. In Fig. 4.28 (b), the FC basal plane magnetization at $B = 0.1\text{T}$ is negative, but $dM/dB > 0$, confirming that the diamagnetic state is originated

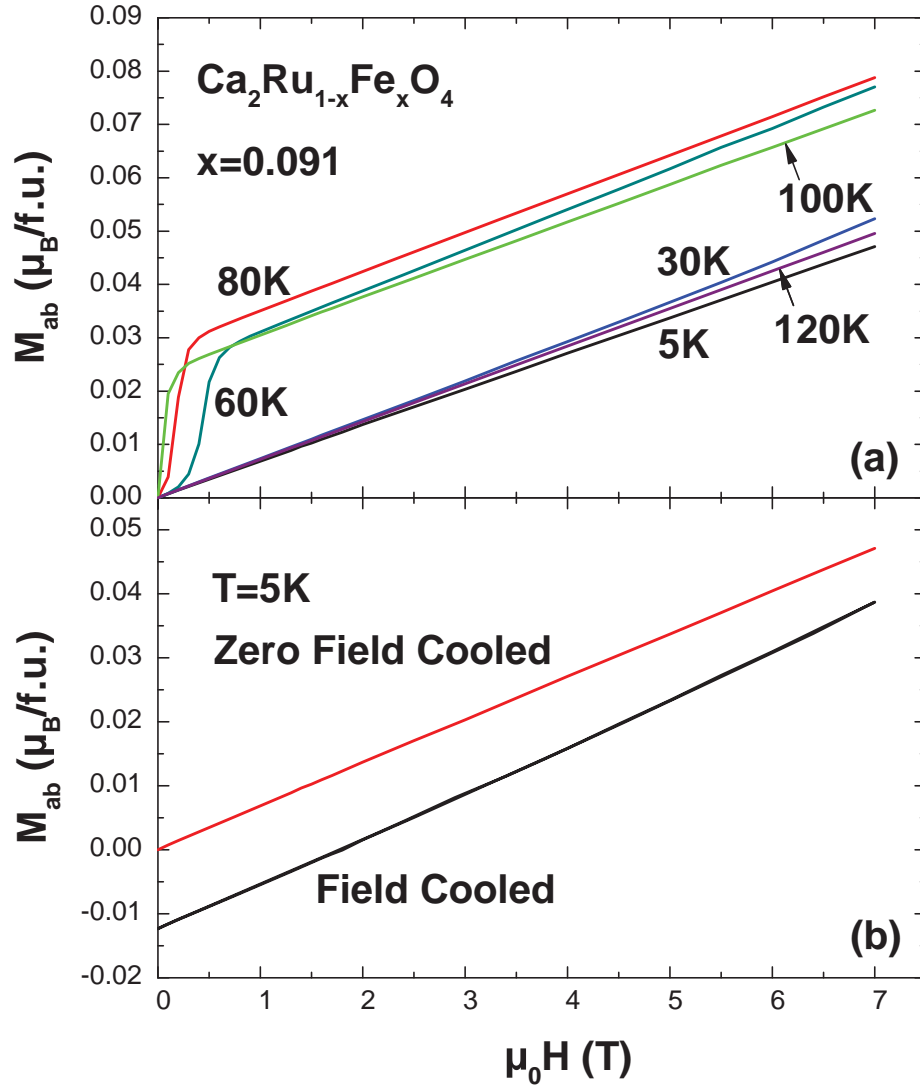


Figure 4.28: For $\text{Ca}_2\text{Ru}_{1-x}\text{Fe}_x\text{O}_4$ with $x = 0.091$, (a) isothermal magnetization M on ab plane at 5K, 30K, 60K, 80K, 100K and 120 K; (b) Field dependence of magnetization M at 5 K for the Field Cooled and Zero Field Cooled sequences.

from spin canting [221]. The ZFC basal plane magnetization shows no magnetization reversal, which is consistent with Fig. 4.27.

This interesting magnetization reversal may come from two different magnetic sites. The Fe doping for Ru in $\text{Ca}_2\text{Ru}_{1-x}\text{Fe}_x\text{O}_4$ may lead to two antiferromagnetically coupled inequivalent magnetic sublattices that have different temperature dependence, resulting in the magnetization reversal [219, 221] 4.4.3. Without apparent spin canting, the magnetoelastic effect may not be strong enough to causes any additional lattice anomaly that features Cr and Mn doped Ca_2RuO_4 [147, 149].

A magnetization reversal is highly unusual but is not without precedent; it has been observed in FM spinels Co_2VO_4 [219] and Co_2TiO_4 [220], and $\text{Sr}_3\text{Ir}_2\text{O}_7$ [221]. However, the magnetization reversal in $\text{Ca}_2\text{Ru}_{1-x}\text{Fe}_x\text{O}_4$ is much more robust, which make it a good sample to study magnetic behavior in Ca_2RuO_4 and has potential applications in electronic devices.

4.5 $\text{Ca}_2\text{Ru}_{1-x}\text{M}_x\text{O}_4$, $\text{M} = 3\text{d transition metal ion}$)

Substituting Ru with a 3d ion always induces a modest and yet critical NTE along the a-axis, as shown in Fig. 4.29. It is this critical change that leads to a rather sizable thermal expansion ratio $\Delta V/V$ on cooling in $\text{Ca}_2\text{Ru}_{1-x}\text{M}_x\text{O}_4$. The fact that this phenomenon does not occur for $x = 0$ despite the strong effect of the NTE along the b-axis underscores how critically M doping "unlocks" strongly buckled Ru/MO6 octahedra and changes the t_{2g} orbital configuration in the basal plane.

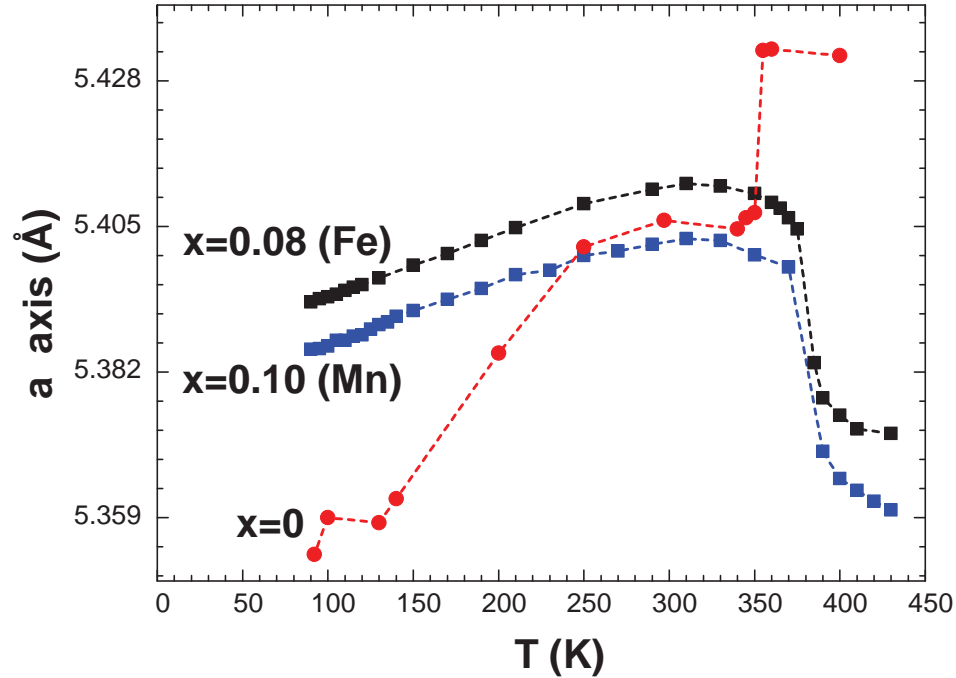


Figure 4.29: Temperature dependences of lattice parameters a-axis for $x = 0$, 0.10 (Mn) and 0.08 (Fe).

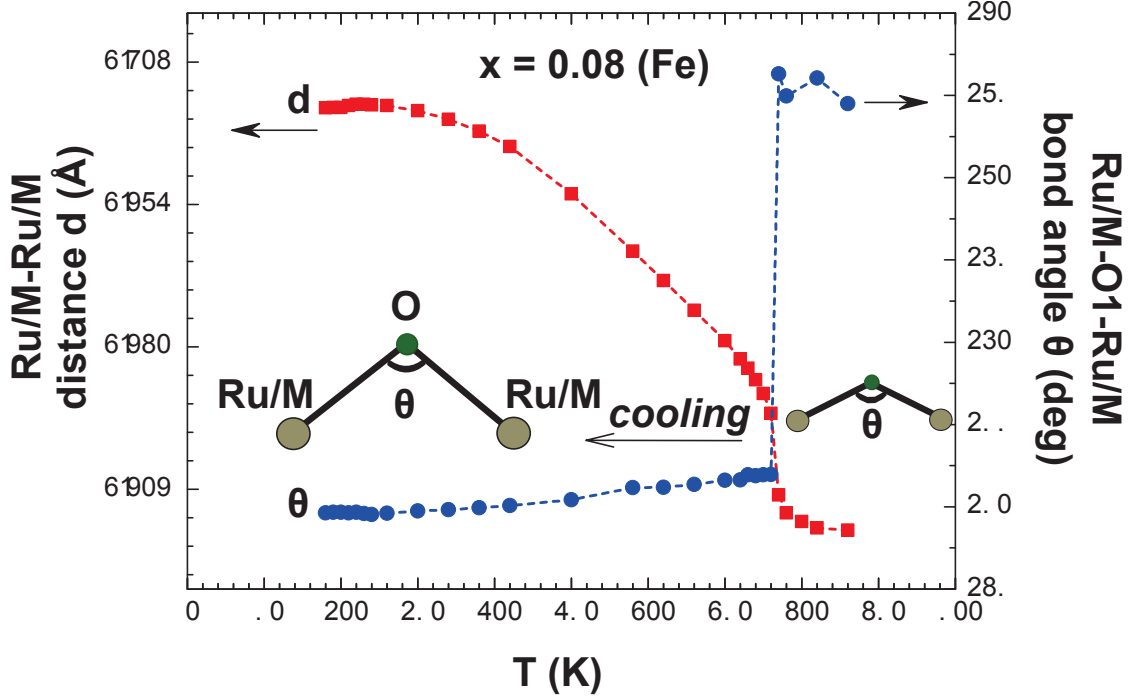


Figure 4.30: Temperature dependences of the Ru/M-Ru/M distance d and the Ru/M-O1-Ru/M bond angle θ (right scale) for $x = 0.08$ (Fe). Inset: schematics illustrating changes of d and θ on cooling.

Indeed, the basal plane Ru/M-O1-Ru/M bond angle θ drastically decreases below T_{MI} that in turn simultaneously prompts an expansion of the Ru/M-O1 bond length and the Ru/M-Ru/M distance d on cooling; as shown in Fig. 4.30 for a representative compound $\text{Ca}_2\text{Ru}_{1-x}\text{Fe}_x\text{O}_4$ with $x = 0.08$, respectively. The expansion of d clearly outweighs positive thermal expansion due to longitudinal vibrational modes, allowing both the a - and b -axis to expand with cooling while preserving the structural symmetry. As a result, V rapidly expands on cooling near T_{MI} where the t_{2g} orbital order takes place. Both the NTE and the orbital order in $\text{Ca}_2\text{Ru}_{1-x}\text{M}_x\text{O}_4$ closely track the changing orthorhombicity as x changes, and disappear when the orthorhombicity vanishes near x_c , a critical doping concentration ($x_c = 0.14, 0.25, 0.22$ and 0.20 for Cr, Mn, Fe and Cu, respectively). As for the magnetic state and the spin-lattice effect, it is recognized that an increase in the Ru-O2 bond length along the c -axis destabilizes the collinear AFM state [216], resulting in strongly competing AFM and FM exchange interactions or spin canting below T_N in doped Ca_2RuO_4 . Except for Fe doping which does not seem to cause spin canting, the spin-lattice coupling or magnetoelastic effect is strong enough to generate an additional lattice anomaly near T_N . It is also noted that the magnitude of the NTE decreases as the atomic number of M increases. This interesting trend may be associated with the fact that with increasing nuclear charge the 3d-orbitals become more contracted, and the 3d-band progressively fills and downshifts away from the Fermi energy E_F , thus weakening the overlapping with 4d-band that stays near E_F .

Copyright© Tongfei Qi, 2012.

Chapter 5 Conclusions

5.1 The New Type of NTE in $\text{Ca}_2\text{Ru}_{1-x}\text{M}_x\text{O}_4$

Ca_2RuO_4 represents a unique archetype of a Mott insulator with a transition at $T_{MI} = 357$ K that is strongly coupled to a structural transition that is not associated with the antiferromagnetic order at $T_N = 110$ K. This study reveals that such a Mott insulator is intimately associated with both NVTE and NLTV when doped by a 3d transition metal ion M for Ru. The NVTE and NLTE observed in this system constitutes a compelling and extraordinary example in that (1) the coefficient of NVTE and NLTE reaches $-213 \times 10^{-6} \text{ K}^{-1}$ and $-148 \times 10^{-6} \text{ K}^{-1}$. The average magnitude of the NTE is about 100 times greater than that for most classic NTE materials, which represents colossal NTE, a phenomenon seldom seen in materials; (2) the NTE anomalies closely track the onset temperatures of orbital and magnetic orders, in sharp contrast to classic NTE that shows no relevance to physical properties; (3) the NTE and physical properties can be effectively tuned via varying M and x in $\text{Ca}_2\text{Ru}_{1-x}\text{M}_x\text{O}_4$; (4) the NTE occurs near room temperature and extends over a wide temperature interval ranging from 100 K to 350 K. With these unique features, these Mott insulators represent a class of novel NTE materials that are intellectually intriguing and technologically desirable.

The conventional theory for NTE focuses on the geometry of lattice structures. For classic NTE materials, such as ZrW_2O_8 and ZrV_2O_7 , the origin of NTE is attributed to the existence of low-frequency phonon modes or rigid unit modes that can propagate without distortions of the WO_4 tetrahedra and ZrO_6 octahedra. This effect alone clearly cannot account for the NTE observed in the ruthenates that tracks orbital and/or magnetic orders, which are dictated by the complex interplay between spin, orbital, lattice and charge degrees of freedom. The microscopic origin therefore are fundamentally different from that for classic NTE materials.

5.2 New Theoretical Paradigm in $\text{Ca}_2\text{Ru}_{1-x}\text{M}_x\text{O}_4$

The unique underlying characteristics of the 4d and 5d materials suggest that there is an electronically-driven mechanism driving the NTE, in sharp contrast to the lattice dynamics dictating classic NTE. Such a mechanism can be qualitatively discussed as follows. In a Mott insulator, the occurrence of an orbital or magnetic order is always accompanied by electron localization. The electron localization costs kinetic energy of electrons whereas lattice expansion reduces the kinetic energy. Meanwhile, the lattice expansion costs the energy for electron-lattice interaction. NTE could happen if the energy gain from the electron-electron interaction and the lattice expansion can overcome the energy cost from the electron-lattice interaction and the electron localization. When the orbital and/or magnetic order takes place, the energy gain of electrons can be described in terms of the short range coupling parameters between

orbital or spin orders; namely, if we use a local exchange effective model to describe the orbital or magnetic order,

$$H = \sum_{ij} J_{ij} A_i A_j \quad (5.1)$$

where A_j represents local spin or orbital moments. The effective coupling parameters J_{ij} are generally determined by virtual hopping processes. Therefore, if the lattice expansion increases J_{ij} , the orbital and/or magnetic order can make the NTE more energetically favorable; this is more likely in a multi-orbital system where the Coulomb repulsion U is relatively small for the reasons: (1) virtual hopping becomes much more complicated in effective bands due to the mixture of different orbitals; and (2) spin-orbit coupling and crystal field effects, which are strongly affected by the lattice expansion, and become comparable to U . $\text{Ca}_2\text{Ru}_{1-x}\text{M}_x\text{O}_4$ are multi-orbital systems with comparable U and spin orbit interaction; therefore, the NTE happens, but in a fashion fundamentally different from that of classic NTE materials, as shown in Fig. 1.4 and 1.5. This work presents convincing evidence that the strong coupling of the NTE to the underlying physical properties exists in a class of the Mott insulators, doped Ca_2RuO_4 , highlighting the new physics yet to be fully understood.

Further efforts on this project needed to be made on both experimental and theoretical studies. We will investigate lattice distortions and associated effects in doped Ca_2RuO_4 with different tools like high pressure and neutron diffraction. We will substitute Ru with all 3d ions from Ti to Zn in a systematic fashion and thoroughly study structural changes as a function of doping and temperature. Then we will extend our study to 4d and 5d element dopants. We are particularly interested in the following aspects in this context:

1. Carefully probe the structural phase transition between tetragonal and orthorhombic distortions.
2. Investigate the relationship between the Ru-O1-Ru bond angle θ and distance d .
3. Generate a phase diagram illustrating the relationship between NTE and orthorhombicity.
4. The structural properties will be also probed by neutron scattering and under different pressure.

Theoretical investigations in this system will take several steps:

First of all, We will use first principle electronic structure calculations to investigate lattice and electronic structures in ordered and unordered (normal) states. Energies from different contributions including spin-orbit, lattice-electron, lattice-lattice and electron-electron interactions and kinetic energy will be calculated separately and compared in different states. The role of spin-orbit coupling in the NVTE will also be studied independently.

Secondly, the calculations above will be analyzed together with experimental measurements to construct a phenomenological model based on *the Landau-Ginzberg theory* with symmetry analysis. We will classify the couplings between lattice distortions and spin and orbital orders, and eventually derive a general phase diagram; this will allow us to address symmetry related questions and will provide a general macroscopic understanding.

Finally, we will focus on developing analytical microscopic models to understand phase transitions and NVTE in this new type of material. We will look for possible signatures in low energy excitations that can be associated with the NVTE. Since orbital, spin and lattice are strongly coupled, thus low energy excitations can be a composed object of these degrees of freedom. Our ultimate objective is to provide an understanding of the NVTE at a microscopic level.

Bibliography

- [1] S. Maekawa, *Physics of transition metal oxides*, vol. 144. Springer Verlag, 2004.
- [2] P. Cox *et al.*, *Transition metal oxides: an introduction to their electronic structure and properties*. Clarendon Press Oxford, 1992.
- [3] Y. Tokura and N. Nagaosa, “Orbital physics in transition-metal oxides,” *science*, vol. 288, no. 5465, pp. 462–468, 2000.
- [4] S. Ishihara, M. Yamanaka, and N. Nagaosa, “Orbital liquid in perovskite transition-metal oxides,” *Physical Review B*, vol. 56, no. 2, p. 686, 1997.
- [5] J. Bednorz and K. Müller, “Possible high Tc superconductivity in the Ba- La- Cu- O system,” *Zeitschrift für Physik B Condensed Matter*, vol. 64, no. 2, pp. 189–193, 1986.
- [6] Y. Maeno, H. Hashimoto, K. Yoshida, S. Nishizaki, T. Fujita, J. G. Bednorz, and F. Lichtenberg, “Superconductivity in a layered perovskite without copper,” *Nature*, vol. 372, pp. 532–534, Dec. 1994.
- [7] M. Rotter, M. Tegel, and D. Johrendt, “Superconductivity at 38 k in the iron arsenide $(\text{Ba}_{1-x}\text{K}_x)\text{Fe}_2\text{As}_2$,” *Physical Review Letters*, vol. 101, no. 10, p. 107006, 2008.
- [8] X. Chen, T. Wu, G. Wu, R. Liu, H. Chen, and D. Fang, “Superconductivity at 43 K in $\text{SmFeAsO}_{1-x}\text{F}_x$,” *Nature*, vol. 453, no. 7196, pp. 761–762, 2008.
- [9] B. Raveau, *Colossal magnetoresistance, charge ordering and related properties of manganese oxides*. World Scientific Publishing Company Incorporated, 1998.
- [10] A. Ramirez, “Colossal magnetoresistance,” *Journal of Physics: Condensed Matter*, vol. 9, no. 39, p. 8171, 1999.
- [11] K. Kang, Y. Meng, J. Bréger, C. Grey, and G. Ceder, “Electrodes with high power and high capacity for rechargeable lithium batteries,” *Science*, vol. 311, no. 5763, pp. 977–980, 2006.
- [12] Y. Idota, T. Kubota, A. Matsufuji, Y. Maekawa, and T. Miyasaka, “Tin-based amorphous oxide: A high-capacity lithium-ion-storage material,” *Science*, vol. 276, no. 5317, pp. 1395–1397, 1997.
- [13] U. Diebold, J. Anderson, K. Ng, and D. Vanderbilt, “Evidence for the Tunneling Site on Transition-Metal Oxides: $\text{TiO}_2(110)$,” *Physical review letters*, vol. 77, no. 7, pp. 1322–1325, 1996.

- [14] M. Ganduglia-Pirovano, A. Hofmann, and J. Sauer, "Oxygen vacancies in transition metal and rare earth oxides: Current state of understanding and remaining challenges," *Surface science reports*, vol. 62, no. 6, pp. 219–270, 2007.
- [15] K. Szot, W. Speier, G. Bihlmayer, and R. Waser, "Switching the electrical resistance of individual dislocations in single-crystalline SrTiO₃," *Nature materials*, vol. 5, no. 4, pp. 312–320, 2006.
- [16] R. Kurtz and V. Henrich, "Surface electronic structure of corundum transition-metal oxides: Ti₂O₃," *Physical Review B*, vol. 25, no. 6, p. 3563, 1982.
- [17] Z. Lu and J. Dahn, "Effects of Stacking Fault Defects on the X-ray Diffraction Patterns of T₂, O₂, and O₆ Structure Li_{2/3}[Co_xNi_{1/3-x}Mn_{2/3}]O₂," *Chemistry of materials*, vol. 13, no. 6, pp. 2078–2083, 2001.
- [18] M. Lee, S. Han, S. Jeon, B. Park, B. Kang, S. Ahn, K. Kim, C. Lee, C. Kim, I. Yoo, *et al.*, "Electrical manipulation of nanofilaments in transition-metal oxides for resistance-based memory," *Nano letters*, vol. 9, no. 4, pp. 1476–1481, 2009.
- [19] P. Bueno, E. Leite, M. Oliveira, M. Orlandi, and E. Longo, "Role of oxygen at the grain boundary of metal oxide varistors: A potential barrier formation mechanism," *Applied Physics Letters*, vol. 79, no. 1, pp. 48–50, 2001.
- [20] V. Kataev, K. Choi, M. Grüninger, U. Ammerahl, B. Büchner, A. Freimuth, and A. Revcolevschi, "Strong anisotropy of superexchange in the copper-oxygen chains of La_{14-x}Ca_xCu₂₄O₄₁," *Physical Review Letters*, vol. 86, no. 13, pp. 2882–2885, 2001.
- [21] F. Barriquand and G. Sawatzky, "Superexchange, hole-hole interactions, and oxygen spin dynamics in high-T_c superconductors," *Physical Review B*, vol. 50, no. 22, p. 16649, 1994.
- [22] C. Delmas, C. Fouassier, and P. Hagenmuller, "Structural classification and properties of the layered oxides," *Physica B+C*, vol. 99, no. 1, pp. 81–85, 1980.
- [23] A. Bolzan, C. Fong, B. Kennedy, and C. Howard, "Structural studies of rutile-type metal dioxides," *Acta Crystallographica Section B: Structural Science*, vol. 53, no. 3, pp. 373–380, 1997.
- [24] R. Mani, S. Achary, K. Chakraborty, S. Deshpande, J. Joy, A. Nag, J. Gopalakrishnan, and A. Tyagi, "Dielectric properties of some MM'O₄ and MTiM'O₆ (M = Cr, Fe, Ga; M' = Nb, Ta, Sb) rutile-type oxides," *Journal of Solid State Chemistry*, vol. 183, no. 6, pp. 1380–1387, 2010.
- [25] H. Tanaka and M. Misono, "Advances in designing perovskite catalysts," *Current Opinion in Solid State and Materials Science*, vol. 5, no. 5, pp. 381–387, 2001.

- [26] R. Coates and J. McMillan, "Oxygen deficiency in perovskite-type compounds of calcium," *Journal of Applied Chemistry*, vol. 14, no. 8, pp. 346–350, 1964.
- [27] S. Javed, A. Khan, A. Majid, A. Mirza, and J. Bashir, "Lattice constant prediction of orthorhombic ABO_3 perovskites using support vector machines," *Computational materials science*, vol. 39, no. 3, pp. 627–634, 2007.
- [28] R. Hines, *Atomistic simulation and ab initio studies of polar solids*. PhD thesis, University of Bristol, 1997.
- [29] V. Goldschmidt, "Die gesetze der krystallochemie," *Naturwissenschaften*, vol. 14, no. 21, pp. 477–485, 1926.
- [30] H. Kronmüller and S. Parkin, *Handbook of magnetism and advanced magnetic materials*. Wiley Online Library, 2007.
- [31] S. Ruddlesden and P. Popper, "New compounds of the K_2NiF_4 type," *Acta Crystallographica*, vol. 10, no. 8, pp. 538–539, 1957.
- [32] S. Ruddlesden and P. Popper, "The compound $\text{Sr}_3\text{Ti}_2\text{O}_7$ and its structure," *Acta Crystallographica*, vol. 11, no. 1, pp. 54–55, 1958.
- [33] B. Beznosikov and K. Aleksandrov, "Perovskite-like crystals of the ruddlesden-popper series," *Crystallography Reports*, vol. 45, no. 5, pp. 792–798, 2000.
- [34] G. Cao, O. Korneta, S. Chikara, L. DeLong, and P. Schlottmann, "Non-Fermi-liquid behavior in single-crystal CaRuO_3 : Comparison to ferromagnetic SrRuO_3 ," *Solid State Communications*, vol. 148, no. 7, pp. 305–309, 2008.
- [35] G. Cao, S. McCall, M. Shepard, J. E. Crow, and R. P. Guertin, "Magnetic and transport properties of single-crystal Ca_2RuO_4 : Relationship to superconducting Sr_2RuO_4 ," *Physical Review B*, vol. 56, p. 2916, Aug. 1997.
- [36] C. S. Alexander, G. Cao, V. Dobrosavljevic, S. McCall, J. E. Crow, E. Lochner, and R. P. Guertin, "Destruction of the Mott insulating ground state of Ca_2RuO_4 by a structural transition," *Physical Review B*, vol. 60, p. 8422, Sept. 1999.
- [37] P. Brüesch, *Phonons: Theory and Experiments I*. Springer-Verlag, 1982.
- [38] V. Korthuis, N. Khosrovani, A. W. Sleight, N. Roberts, R. Dupree, and W. W. J. Warren, "Negative thermal-expansion and phase-transitions in the $\text{ZrV}_{2-x}\text{P}_x\text{O}_7$ series," *Chemistry of Materials*, vol. 7, pp. 412–417, February 1995.
- [39] N. Khosrovani, V. Korthuis, A. Sleight, and T. Vogt, "Unusual 180° pop bond angles in ZrP_2O_7 ," *Inorganic chemistry*, vol. 35, no. 2, pp. 485–489, 1996.
- [40] J. Evans, J. Hanson, and A. Sleight, "Room-temperature superstructure of ZrV_2O_7 ," *Acta Crystallographica Section B: Structural Science*, vol. 54, no. 6, pp. 705–713, 1998.

- [41] R. Withers, J. Evans, J. Hanson, and A. Sleight, "An *In Situ* Temperature-Dependent Electron and X-ray Diffraction Study of Structural Phase Transitions in ZrV_2O_7 ," *Journal of Solid State Chemistry*, vol. 137, no. 1, pp. 161–167, 1998.
- [42] J. Evans, T. Mary, T. Vogt, M. Subramanian, and A. Sleight, "Negative thermal expansion in ZrW_2O_8 and HfW_2O_8 ," *Chemistry of materials*, vol. 8, no. 12, pp. 2809–2823, 1996.
- [43] T. A. Mary, J. S. O. Evans, T. Vogt, and A. W. Sleight, "Negative Thermal Expansion from 0.3 to 1050 Kelvin in ZrW_2O_8 ," *Science*, vol. 272, pp. 90–92, Apr. 1996.
- [44] C. Lind, A. Wilkinson, Z. Hu, S. Short, and J. Jorgensen, "Synthesis and properties of the negative thermal expansion material cubic ZrMo_2O_8 ," *Chemistry of materials*, vol. 10, no. 9, pp. 2335–2337, 1998.
- [45] C. Closmann, A. Sleight, and J. Haygarth, "Low-temperature synthesis of ZrW_2O_8 and mo-substituted ZrW_2O_8 ," *Journal of Solid State Chemistry*, vol. 139, no. 2, pp. 424–426, 1998.
- [46] J. S. O. Evans, T. A. Mary, and A. W. Sleight, "Negative Thermal Expansion in a Large Molybdate and Tungstate Family," *Journal of Solid State Chemistry*, vol. 133, pp. 580–583, Nov. 1997.
- [47] J. Evans, T. Mary, and A. Sleight, "Negative thermal expansion in $\text{Sc}_2(\text{WO}_4)_3$," *Journal of Solid State Chemistry*, vol. 137, no. 1, pp. 148–160, 1998.
- [48] P. Forster, A. Yokochi, and A. Sleight, "Enhanced negative thermal expansion in $\text{Lu}_2\text{W}_3\text{O}_{12}$," *Journal of Solid State Chemistry*, vol. 140, no. 1, pp. 157–158, 1998.
- [49] T. Mary and A. Sleight, "Bulk thermal expansion for tungstate and molybdates of the type $\text{A}_2\text{M}_3\text{O}_{12}$," *Journal of Materials research*, vol. 14, no. 03, pp. 912–915, 1999.
- [50] P. Tschaufeser and S. Parker, "Thermal expansion behavior of zeolites and AlPO_4s ," *The Journal of Physical Chemistry*, vol. 99, no. 26, pp. 10609–10615, 1995.
- [51] M. Attfield, "Strong negative thermal expansion in siliceous faujasite," *Chem. Commun.*, no. 5, pp. 601–602, 1998.
- [52] M. Attfield and A. Sleight, "Exceptional negative thermal expansion in $\text{AlPO}_4\text{-17}$," *Chemistry of materials*, vol. 10, no. 7, pp. 2013–2019, 1998.
- [53] D. Woodcock, P. Lightfoot, L. Villaescusa, M. Díaz-Cabañas, M. Camblor, and D. Engberg, "Negative thermal expansion in the siliceous zeolites chabazite and ITQ-4: A neutron powder diffraction study," *Chemistry of materials*, vol. 11, no. 9, pp. 2508–2514, 1999.

- [54] D. Woodcock, P. Lightfoot, P. Wright, L. Villaescusa, and M. Cambor, "Strong negative thermal expansion in the siliceous zeolites ITQ-1, ITQ-3 and SSZ-23," *J. Mater. Chem.*, vol. 9, no. 2, pp. 349–351, 1999.
- [55] T. Amos and A. Sleight, "Negative thermal expansion in orthorhombic NbOPO_4 ," *Journal of Solid State Chemistry*, vol. 160, no. 1, pp. 230–238, 2001.
- [56] T. Amos, A. Yokochi, and A. Sleight, "Phase transition and negative thermal expansion in tetragonal NbOPO_4 ," *Journal of Solid State Chemistry*, vol. 141, no. 1, pp. 303–307, 1998.
- [57] R. Roy, D. Agrawal, and H. McKinstry, "Very Low Thermal-Expansion Coefficient Materials," *Annual Review of Materials Science*, vol. 19, pp. 59–81, 1989.
- [58] J. Evans, T. Mary, and A. Sleight, "Negative thermal expansion materials," *Physica B: Condensed Matter*, vol. 241, pp. 311–316, 1997.
- [59] A. Pryde, K. Hammonds, M. Dove, V. Heine, J. Gale, and M. Warren, "Origin of the negative thermal expansion in ZrW_2O_8 and ZrV_2O_7 ," *Journal of Physics: Condensed Matter*, vol. 8, p. 10973, 1996.
- [60] D. Olson, G. Kokotailo, S. Lawton, and W. Meier, "Crystal structure and structure-related properties of ZSM-5," *The Journal of Physical Chemistry*, vol. 85, no. 15, pp. 2238–2243, 1981.
- [61] R. Weis and T. Gaylord, "Lithium niobate: summary of physical properties and crystal structure," *Applied Physics A: Materials Science & Processing*, vol. 37, no. 4, pp. 191–203, 1985.
- [62] T. Sarkar, B. Ghosh, A. Raychaudhuri, and T. Chatterji, "Crystal structure and physical properties of half-doped manganite nanocrystals of less than 100-nm size," *Physical Review B*, vol. 77, no. 23, p. 235112, 2008.
- [63] X. Luo, X. Wang, J. Ying, Y. Yan, Z. Li, M. Zhang, A. Wang, P. Cheng, Z. Xiang, G. Ye, *et al.*, "Crystal structure, physical properties and superconductivity in $\text{A}_x\text{Fe}_2\text{Se}_2$ single crystals," *New Journal of Physics*, vol. 13, no. 5, p. 053011, 2011.
- [64] S. Chen, X. Gong, A. Walsh, and S. Wei, "Crystal and electronic band structure of CuZnSnX ($\text{X} = \text{S}$ and Se) photovoltaic absorbers: First-principles insights," *Applied Physics Letters*, vol. 94, p. 041903, 2009.
- [65] C. Barrett and T. Massalski, *Structure of metals*, vol. 631. McGraw-Hill New York, 1966.
- [66] S. Sun and C. Murray, "Synthesis of monodisperse cobalt nanocrystals and their assembly into magnetic superlattices," *Journal of Applied Physics*, vol. 85, no. 8, pp. 4325–4330, 1999.

- [67] T. Yamanaka, K. Hirose, W. Mao, Y. Meng, P. Ganesh, L. Shulenburger, G. Shen, and R. Hemley, “Crystal structures of $(\text{Mg}_{1-x}, \text{Fe}_x) \text{SiO}_3$ postperovskite at high pressures,” *Proceedings of the National Academy of Sciences*, vol. 109, no. 4, pp. 1035–1040, 2012.
- [68] L. Farrugia, “WinGX suite for small-molecule single-crystal crystallography,” *Journal of Applied Crystallography*, vol. 32, no. 4, pp. 837–838, 1999.
- [69] T. Proffen and R. Neder, “DISCUS: A program for diffuse scattering and defect-structure simulation,” *Journal of applied crystallography*, vol. 30, no. 2, pp. 171–175, 1997.
- [70] W. Bragg and W. Bragg, “The structure of the diamond,” *Nature*, vol. 91, p. 557, 1913.
- [71] W. Bragg, “The reflection of x-rays by crystals,” *Nature*, vol. 91, p. 477, 1913.
- [72] J. Pflugrath, “The finer things in X-ray diffraction data collection,” *Acta Crystallographica Section D: Biological Crystallography*, vol. 55, no. 10, pp. 1718–1725, 1999.
- [73] R. Neutze, R. Wouts, D. van der Spoel, E. Weckert, and J. Hajdu, “Potential for biomolecular imaging with femtosecond X-ray pulses,” *Nature*, vol. 406, no. 6797, pp. 752–757, 2000.
- [74] F. Van der Veen and F. Pfeiffer, “Coherent x-ray scattering,” *Journal of Physics: Condensed Matter*, vol. 16, no. 28, p. 5003, 2004.
- [75] R. Stewart, E. Davidson, and W. Simpson, “Coherent X-Ray Scattering for the Hydrogen Atom in the Hydrogen Molecule,” *The Journal of Chemical Physics*, vol. 42, p. 3175, 1965.
- [76] D. Bellet, G. Dolino, M. Ligeon, P. Blanc, and M. Krisch, “Studies of coherent and diffuse x-ray scattering by porous silicon,” *Journal of applied physics*, vol. 71, no. 1, pp. 145–149, 1992.
- [77] E. Prince, *International tables for crystallography*. Kluwer Academic Publishers Dordrecht, The Netherlands, 2004.
- [78] H. Bale and P. Schmidt, “Small-angle x-ray-scattering investigation of submicroscopic porosity with fractal properties,” *Physical Review Letters*, vol. 53, no. 6, pp. 596–599, 1984.
- [79] A. Ankudinov, B. Ravel, J. Rehr, and S. Conradson, “Real-space multiple-scattering calculation and interpretation of x-ray-absorption near-edge structure,” *Physical Review B*, vol. 58, no. 12, p. 7565, 1998.
- [80] G. Pawley, “Unit-cell refinement from powder diffraction scans,” *Journal of Applied Crystallography*, vol. 14, no. 6, pp. 357–361, 1981.

- [81] C. Kittel and P. McEuen, *Introduction to solid state physics*, vol. 7. Wiley New York, 1996.
- [82] M. Imada, A. Fujimori, and Y. Tokura, “Metal-insulator transitions,” *Reviews of Modern Physics*, vol. 70, no. 4, p. 1039, 1998.
- [83] N. Mott, “Metal-insulator transition,” *Reviews of Modern Physics*, vol. 40, pp. 677–683, 1968.
- [84] M. Fabrizio, A. Gogolin, and A. Nersesyan, “From band insulator to mott insulator in one dimension,” *Physical review letters*, vol. 83, no. 10, pp. 2014–2017, 1999.
- [85] A. Garg, H. Krishnamurthy, and M. Randeria, “Can correlations drive a band insulator metallic?,” *Physical review letters*, vol. 97, no. 4, p. 46403, 2006.
- [86] J. Cherian, “Mott metal insulator transitions,” *Bulletin of Florida state University*, p. 8, 2010.
- [87] T. Rice, H. Launois, and J. Pouget, “Comment on" VO₂: Peierls or Mott-Hubbard? A View from Band Theory",” *Physical review letters*, vol. 73, no. 22, pp. 3042–3042, 1994.
- [88] H. Fehske, G. Wellein, G. Hager, A. Weisse, and A. Bishop, “Quantum lattice dynamical effects on single-particle excitations in one-dimensional mott and peierls insulators,” *Physical Review B*, vol. 69, no. 16, p. 165115, 2004.
- [89] J. Pichard, M. Sanquer, K. Slevin, and P. Debray, “Broken symmetries and localization lengths in anderson insulators: Theory and experiment,” *Physical review letters*, vol. 65, no. 14, pp. 1812–1815, 1990.
- [90] J. Li, R. Chu, J. Jain, and S. Shen, “Topological anderson insulator,” *Physical review letters*, vol. 102, no. 13, p. 136806, 2009.
- [91] N. der NV Philips’ Gloeilampenfabrieken and H. E. V. Eindhoven, “Semiconductors with partially and with completely filled 3-lattice bands,” *Proceedings of the Physical Society*, vol. 49, 1937.
- [92] N. Mott and R. Peierls, “Discussion of the paper by de Boer and Verwey,” *Proceedings of the Physical Society*, vol. 49, no. 4S, p. 72, 1937.
- [93] F. Gebhard, *The mott metal-insulator transition: models and methods*, vol. 137. Springer, 1997.
- [94] N. Mott, *Metal-insulator transitions*. Taylor & Francis London, 1990.
- [95] G. Kotliar and D. Vollhardt, “Strongly correlated materials: Insights from dynamical mean-field theory,” *Physics Today*, vol. 57, no. 3, pp. 53–60, 2004.

- [96] N. Mott and H. Jones, *The theory of the properties of metals and alloys*. Dover Publications, 1958.
- [97] N. Mott, “The transition to the metallic state,” *Philosophical Magazine*, vol. 6, no. 62, pp. 287–309, 1961.
- [98] A. Sutton, *Electronic structure of materials*. Oxford University Press, USA, 1993.
- [99] P. Fazekas, *Lecture notes on electron correlation and magnetism*, vol. 24. World Scientific, 1999.
- [100] P. Anderson, “Absence of diffusion in certain random lattices,” *Physical review*, vol. 109, no. 5, p. 1492, 1958.
- [101] N. Mott, M. Pepper, S. Pollitt, R. Wallis, C. Adkins, N. Mott, M. Pepper, S. Pollitt, R. Wallis, and C. Adkins, “The Anderson transition,” *Proceedings of the Royal Society of London. A. Mathematical and Physical Sciences*, vol. 345, no. 1641, pp. 169–205, 1975.
- [102] X. Chen, *Numerical studies of the combined effects of interactions and disorder at metal-insulator transitions*. PhD thesis, Queen’s University, 2009.
- [103] S. Blundell and D. Thouless, *Magnetism in condensed matter*, vol. 13. Oxford University Press New York, 2001.
- [104] R. Greenberger, *The Technology of Ancient China*. Rosen Central, 2006.
- [105] I. Charvátová, J. Klokočník, J. Kolmaš, and J. Kostecký, “Chinese tombs oriented by a compass: Evidence from paleomagnetic changes versus the age of tombs,” *Studia Geophysica et Geodaetica*, vol. 55, no. 1, pp. 159–174, 2011.
- [106] S. Chikazumi and S. Charap, *Physics of magnetism*. Krieger New York, 1978.
- [107] T. Zhou, S. Leong, Z. Yuan, S. Hu, C. Ong, and B. Liu, “Manipulation of magnetism by electrical field in a real recording system,” *Applied Physics Letters*, vol. 96, no. 1, pp. 012506–012506, 2010.
- [108] E. Kneller and R. Hawig, “The exchange-spring magnet: a new material principle for permanent magnets,” *Magnetics, IEEE Transactions on*, vol. 27, no. 4, pp. 3588–3560, 1991.
- [109] C. Demaine and P. Semm, “The avian pineal gland as an independent magnetic sensor,” *Neuroscience letters*, vol. 62, no. 1, pp. 119–122, 1985.
- [110] C. Hurd, “Varieties of magnetic order in solids,” *Contemporary Physics*, vol. 23, no. 5, pp. 469–493, 1982.
- [111] F. Hippert, E. Geissler, J. Hodeau, E. Lelièvre-Berna, and J. Regnard, *Neutron and X-ray Spectroscopy*. Springer, 2005.

- [112] B. J. Kim, H. Jin, S. J. Moon, J.-Y. Kim, B.-G. Park, C. S. Leem, J. Yu, T. W. Noh, C. Kim, S.-J. Oh, J.-H. Park, V. Durairaj, G. Cao, and E. Rotenberg, “Novel $J_{\text{eff}} = 1/2$ Mott State Induced by Relativistic Spin-Orbit Coupling in Sr_2IrO_4 ,” *Phys. Rev. Lett.*, vol. 101, p. 076402, Aug 2008.
- [113] S. Chikara, O. Korneta, W. P. Crummett, L. E. DeLong, P. Schlottmann, and G. Cao, “Giant magnetoelectric effect in the $J_{\text{eff}}=\frac{1}{2}$ Mott insulator Sr_2IrO_4 ,” *Phys. Rev. B*, vol. 80, p. 140407, Oct 2009.
- [114] M. Ge, T. F. Qi, O. B. Korneta, D. E. De Long, P. Schlottmann, W. P. Crummett, and G. Cao, “Lattice-driven magnetoresistivity and metal-insulator transition in single-layered iridates,” *Phys. Rev. B*, vol. 84, p. 100402, Sep 2011.
- [115] O. Korneta, T. Qi, S. Chikara, S. Parkin, L. De Long, P. Schlottmann, and G. Cao, “Electron-doped $\text{Sr}_2\text{IrO}_{4-\delta}$ ($0 \leq \delta \leq 0.04$): Evolution of a disordered $J_{\text{eff}}=1/2$ Mott insulator into an exotic metallic state,” *Physical Review B*, vol. 82, no. 11, p. 115117, 2010.
- [116] R. Burns, *Mineralogical applications of crystal field theory*, vol. 5. Cambridge University Press, 1993.
- [117] J. Post, “Manganese oxide minerals: Crystal structures and economic and environmental significance,” *Proceedings of the National Academy of Sciences*, vol. 96, no. 7, pp. 3447–3454, 1999.
- [118] D. Wood, J. Ferguson, K. Knox, and J. Dillon Jr, “Crystal-Field Spectra of d Ions. III. Spectrum of Cr in Various Octahedral Crystal Fields,” *The Journal of Chemical Physics*, vol. 39, p. 890, 1963.
- [119] J. Ferguson, D. Wood, and K. Knox, “Crystal-Field Spectra of d, d Ions. II. KCoF , CoCl , CoBr , and CoWO ,” *The Journal of Chemical Physics*, vol. 39, p. 881, 1963.
- [120] F. De Groot, J. Fuggle, B. Thole, and G. Sawatzky, “ $2p$ x-ray absorption of $3d$ transition-metal compounds: An atomic multiplet description including the crystal field,” *Physical Review B*, vol. 42, no. 9, p. 5459, 1990.
- [121] D. Fröhlich, E. Mohler, and P. Wiesner, “Observation of exciton polariton dispersion in CuCl ,” *Physical Review Letters*, vol. 26, no. 10, pp. 554–556, 1971.
- [122] H. Jahn and E. Teller, “Stability of polyatomic molecules in degenerate electronic states. i. orbital degeneracy,” *Proceedings of the Royal Society of London. Series A, Mathematical and Physical Sciences*, vol. 161, no. 905, pp. 220–235, 1937.
- [123] M. O’Brien and C. Chancey, “The Jahn-Teller effect: An introduction and current review,” *American Journal of Physics*, vol. 61, pp. 688–697, 1993.

- [124] O. Korneta, *A systematic study of transport, magnetic and thermal properties of layered iridates*. PhD thesis, University of Kentucky, 2012.
- [125] A. Millis, B. Shraiman, and R. Mueller, “Dynamic Jahn-Teller Effect and Colossal Magnetoresistance in $\text{La}_{1-x}\text{Sr}_x\text{MnO}_3$,” *Physical review letters*, vol. 77, no. 1, pp. 175–178, 1996.
- [126] G. Gehring and K. Gehring, “Cooperative Jahn-Teller effects,” *Reports on Progress in Physics*, vol. 38, no. 1, p. 1, 2001.
- [127] B. Halperin and R. Englman, “Cooperative Dynamic Jahn-Teller Effect. II. Crystal Distortion in Perovskites,” *Physical Review B*, vol. 3, no. 5, p. 1698, 1971.
- [128] H. Meskine, H. König, and S. Satpathy, “Orbital ordering and exchange interaction in the manganites,” *Physical Review B*, vol. 64, no. 9, p. 094433, 2001.
- [129] M. Ruderman and C. Kittel, “Indirect exchange coupling of nuclear magnetic moments by conduction electrons,” *Physical Review*, vol. 96, no. 1, p. 99, 1954.
- [130] S. Tarucha, D. Austing, Y. Tokura, W. Van der Wiel, and L. Kouwenhoven, “Direct coulomb and exchange interaction in artificial atoms,” *Physical review letters*, vol. 84, no. 11, pp. 2485–2488, 2000.
- [131] C. Zener, “Interaction between the d shells in the transition metals,” *Physical Review*, vol. 81, no. 3, p. 440, 1951.
- [132] T. Moriya, “Anisotropic superexchange interaction and weak ferromagnetism,” *Physical Review*, vol. 120, no. 1, p. 91, 1960.
- [133] G. Prinz, “Magnetoelectronics,” *Science*, vol. 282, no. 5394, pp. 1660–1663, 1998.
- [134] N. Huang and R. Orbach, “Biquadratic superexchange,” *Physical Review Letters*, vol. 12, no. 11, pp. 275–276, 1964.
- [135] K. Klabunde and R. Richards, *Nanoscale materials in chemistry*. Wiley Online Library, 2001.
- [136] R. Stuart and W. Marshall, “Direct exchange in ferromagnets,” *Physical Review*, vol. 120, no. 2, p. 353, 1960.
- [137] P. de Chatel, “The rkky interaction in disordered systems,” *Journal of Magnetism and Magnetic Materials*, vol. 23, no. 1, pp. 28–34, 1981.
- [138] J. Kanamori, “Superexchange interaction and symmetry properties of electron orbitals,” *Journal of Physics and Chemistry of Solids*, vol. 10, no. 2, pp. 87–98, 1959.

- [139] Z. Shen and D. Dessau, “Electronic structure and photoemission studies of late transition-metal oxides-mott insulators and high-temperature superconductors,” *Physics Reports*, vol. 253, no. 1, pp. 1–162, 1995.
- [140] J. van den Brink, P. Horsch, F. Mack, and A. Oleś, “Orbital dynamics in ferromagnetic transition-metal oxides,” *Physical Review B*, vol. 59, no. 10, p. 6795, 1999.
- [141] P. W. Anderson, “New approach to the theory of superexchange interactions,” *Phys. Rev.*, vol. 115, pp. 2–13, Jul 1959.
- [142] K. Kubo and N. Ohata, “A quantum theory of double exchange. i,” *Journal of the Physical society of Japan*, vol. 33, p. 21, 1972.
- [143] P. G. de Gennes, “Effects of double exchange in magnetic crystals,” *Phys. Rev.*, vol. 118, pp. 141–154, Apr 1960.
- [144] C. Zener, “Interaction between the d -shells in the transition metals. ii. ferromagnetic compounds of manganese with perovskite structure,” *Phys. Rev.*, vol. 82, pp. 403–405, May 1951.
- [145] T. Moriya, “New mechanism of anisotropic superexchange interaction,” *Physical Review Letters*, vol. 4, no. 5, pp. 228–230, 1960.
- [146] I. Dzyaloshinsky, “A thermodynamic theory of "weak" ferromagnetism of antiferromagnetics,” *Journal of Physics and Chemistry of Solids*, vol. 4, no. 4, pp. 241–255, 1958.
- [147] T. F. Qi, O. B. Korneta, S. Parkin, L. E. de Long, P. Schlottmann, and G. Cao, “Negative Volume Thermal Expansion Via Orbital and Magnetic Orders in $\text{Ca}_2\text{Ru}_{1-x}\text{Cr}_x\text{O}_4$ ($0 < x < 0.13$),” *Physical Review Letters*, vol. 105, p. 177203, Oct. 2010.
- [148] T. F. Qi, M. Ge, O. B. Korneta, S. Parkin, L. E. de Long, and G. Cao, “Structurally-driven metal-insulator transition in $\text{Ca}_2\text{Ru}_{1-x}\text{Cr}_x\text{O}_4$ ($0 \leq x < 0.14$): A single crystal X-ray diffraction study,” *Journal of Solid State Chemistry*, vol. 184, pp. 893–898, Apr. 2011.
- [149] T. F. Qi, O. Korneta, S. Parkin, J. Hu, and G. Cao, “Magnetic and orbital orders coupled to negative thermal expansion in Mott insulators $\text{Ca}_2\text{Ru}_{1-x}\text{M}_x\text{O}_4$ ($\text{M} = \text{Mn}$ and Fe),” *Physical Review B*, vol. 85, no. 16, p. 165143, 2012.
- [150] O. Korneta, S. Chikara, S. Parkin, L. DeLong, P. Schlottmann, and G. Cao, “Pressure-induced insulating state in $\text{Ba}_{1-x}\text{R}_x\text{IrO}_3$ ($\text{R} = \text{Gd}, \text{Eu}$) single crystals,” *Physical Review B*, vol. 81, no. 4, p. 045101, 2010.
- [151] T. Qi, O. Korneta, X. Wan, L. DeLong, P. Schlottmann, and G. Cao, “Strong magnetic instability in correlated metallic $\text{Bi}_2\text{Ir}_2\text{O}_7$,” *Journal of Physics: Condensed Matter*, vol. 24, no. 34, p. 345601, 2012.

- [152] F. Ye, S. Chi, H. Cao, B. Chakoumakos, J. Fernandez-Baca, R. Custelcean, T. Qi, O. Korneta, and G. Cao, "Direct evidence of a zigzag spin-chain structure in the honeycomb lattice: A neutron and x-ray diffraction investigation of single-crystal Na_2IrO_3 ," *Physical Review B*, vol. 85, no. 18, p. 180403, 2012.
- [153] X. Liu, V. Katukuri, L. Hozoi, W. Yin, M. Dean, M. Upton, J. Kim, D. Casa, A. Said, T. Gog, T. F. Qi, G. Cao, A. M. Tsvelik, J. van den Brink, and J. P. Hill, "Testing the Validity of the Strong Spin-Orbit-Coupling Limit for Octahedrally Coordinated Iridate Compounds in a Model System $\text{Sr}_3\text{CuIrO}_6$," *Physical Review Letters*, vol. 109, no. 15, p. 157401, 2012.
- [154] T. F. Ciszek and T. H. Wang, "Silicon defect and impurity studies using float-zone crystal growth as a tool," *Journal of Crystal Growth*, vol. 237-239, pp. 1685–1691, 2002.
- [155] P. Capper, *Bulk Crystal Growth in Electronic, Optical and Optoelectronic Materials*. Wiley, April 2005.
- [156] *Instruction manual -SC II-MDH-11020 Single crystal growing apparatus*. NEC Machinery Corporation, 2002.
- [157] G. Cao, S. McCall, J. E. Crow, and R. P. Guertin, "Observation of a Metallic Antiferromagnetic Phase and Metal to Nonmetal Transition in $\text{Ca}_3\text{Ru}_2\text{O}_7$," *Physical Review Letters*, vol. 78, pp. 1751–1754, Mar. 1997.
- [158] K. Tsuji, J. Injuk, and R. Grieken, *X-ray spectrometry: recent technological advances*. John Wiley & Sons Inc, 2004.
- [159] J. Goldstein, D. Newbury, P. Echlin, D. Joy, C. Fiori, and E. Lifshin, *Scanning electron microscopy and X-ray microanalysis: A text for biologists, materials scientists, and geologists*. Plenum Press, New York, NY, USA, 1981.
- [160] J. Goldstein, *Scanning electron microscopy and X-ray microanalysis*, vol. 1. Springer, 2003.
- [161] *Scintag X1. Technical Manual*. No. 95014, Scintag Inc. USA, Cupertino, CA, 1999.
- [162] D. Smith and R. Jenkins, "The powder diffraction file: past, present, and future," *Journal of research of the National Institute of Standards and Technology*, vol. 101, no. 3, 1996.
- [163] M. Tate, E. Eikenberry, S. Barna, M. Wall, J. Lowrance, and S. Gruner, "A large-format high-resolution area X-ray detector based on a fiber-optically bonded charge-coupled device (CCD)," *Journal of applied crystallography*, vol. 28, no. 2, pp. 196–205, 1995.

- [164] P. Fenter, J. Catalano, C. Park, and Z. Zhang, "On the use of ccd area detectors for high-resolution specular x-ray reflectivity," *Journal of synchrotron radiation*, vol. 13, no. 4, pp. 293–303, 2006.
- [165] J. Zaleski, G. Wu, and P. Coppens, "On the correction of reflection intensities recorded on imaging plates for incomplete absorption in the phosphor layer.," *Journal of applied crystallography*, vol. 31, no. 2, pp. 302–304, 1998.
- [166] G. M. Sheldrick, "A short history of *SHELX*," *Acta Crystallographica Section A*, vol. 64, pp. 112–122, Jan 2008.
- [167] G. M. Sheldrick, *SADABS*. University of Gottingen, Germany, 1996.
- [168] S. Parkin, B. Moezzi, and H. Hope, "XABS2: an empirical absorption correction program," *Journal of Applied Crystallography*, vol. 28, pp. 53–56, Feb 1995.
- [169] C. Bean, "Magnetization of high-field superconductors," *Reviews of Modern Physics*, vol. 36, no. 1, pp. 31–38, 1964.
- [170] S. Kotler, *The Magnetic Susceptibility of a Superconductor*. PhD thesis, Lake Forest College, 2009.
- [171] A. Ginsberg, R. Martin, and R. Sherwood, "Magnetic exchange in transition metal complexes. IV. Linear trimeric bis (acetylacetonato) Nickel (II)," *Inorganic Chemistry*, vol. 7, no. 5, pp. 932–936, 1968.
- [172] B. Figgis and J. Lewis, "The magnetic properties of transition metal complexes," *Progress in inorganic chemistry*, vol. 6, pp. 37–239, 1964.
- [173] E. de Lacheisserie, D. Gignoux, and M. Schlenker, *Magnetism: Materials and applications*, vol. 2. Springer, 2004.
- [174] K. Buschow, "Concise encyclopedia of magnetic & super conducting materials," *Recherche*, vol. 67, p. 02, 2005.
- [175] *Magnetic Property Measurement System MPMS XL. Hardware Reference Manual*. Quantum Design, San Diego, CA, 2000.
- [176] J. CLARKE and A. Braginski, "The squid handbook, vol 2: Applications of squids & squid systems," *Recherche*, vol. 67, p. 02, 2006.
- [177] M. McElfresh, "Fundamentals of magnetism and magnetic measurements featuring Quantum Design's magnetic property measurement system," *Quantum Design*, vol. 11578, 1994.
- [178] D. Doshi, *New Living Science PHYSICS for CLASS 9 With More Numerical Problems*. Ratna Sagar, 2006.
- [179] "EPO-TEK H20E" *Material Safety Data Sheet*. Epoxy Technology Inc., Billerica, MA, September 2010.

- [180] "7031 Varnish (Phenolic Butvar Resin)" *Material Safety Data Sheet*. General Electric Co. Schenectady, NY, 1985.
- [181] *LR-700 AC Resistance Bridge User's Manual, v1.3 ed.* Linear Research Inc., San Diego, CA, 1996.
- [182] "Apiezon N, cryogenic high vacuum grease." *Technical Data Sheet*. M&I Materials, Manchester, United Kingdom, August 2005.
- [183] "Apiezon H, high temperature vacuum grease." *Technical Data Sheet*. M&I Materials, Manchester, United Kingdom, August 2005.
- [184] *Physical Property Measurement System PPMS. Hardware Reference Manual, 3rd ed.* Quantum Design, San Diego, CA, 2000.
- [185] J. Hwang, K. Lin, and C. Tien, "Measurement of heat capacity by fitting the whole temperature response of a heat-pulse calorimeter," *Review of scientific instruments*, vol. 68, no. 1, pp. 94–101, 1997.
- [186] V. Pecharsky and K. Gschneidner, "Heat capacity near first order phase transitions and the magnetocaloric effect: An analysis of the errors, and a case study of $\text{Gd}_5(\text{Si}_2\text{Ge}_2)$ and Dy," *Journal of applied physics*, vol. 86, no. 11, pp. 6315–6321, 1999.
- [187] M. Braden, G. André, S. Nakatsuji, and Y. Maeno, "Crystal and magnetic structure of Ca_2RuO_4 : Magnetoelastic coupling and the metal-insulator transition," *Physical Review B*, vol. 58, pp. 847–861, July 1998.
- [188] G. Cao, S. McCall, V. Dobrosavljevic, C. S. Alexander, J. E. Crow, and R. P. Guertin, "Ground-state instability of the Mott insulator Ca_2RuO_4 : Impact of slight La doping on the metal-insulator transition and magnetic ordering," *Physical Review B*, vol. 61, p. 5053, Feb. 2000.
- [189] D. B. McWhan, T. M. Rice, and J. P. Remeika, "Mott Transition in Cr-Doped V_2O_3 ," *Phys. Rev. Lett.*, vol. 23, pp. 1384–1387, Dec 1969.
- [190] J. Jung, Z. Fang, J. He, Y. Kaneko, Y. Okimoto, and Y. Tokura, "Change of Electronic Structure in Ca_2RuO_4 Induced by Orbital Ordering," *Physical Review Letters*, vol. 91, p. 056403, July 2003.
- [191] G.-Q. Liu, "Spin-orbit coupling induced Mott transition in $\text{Ca}_{2-x}\text{Sr}_x\text{RuO}_4$ ($0 \leq x \leq 0.2$)," *Physical Review B*, vol. 84, p. 235136, Dec. 2011.
- [192] C. S. Snow, S. L. Cooper, G. Cao, J. E. Crow, H. Fukazawa, S. Nakatsuji, and Y. Maeno, "Pressure-Tuned Collapse of the Mott-Like State in $\text{Ca}_{n+1}\text{Ru}_n\text{O}_{3n+1}$ ($n=1,2$): Raman Spectroscopic Studies," *Physical Review Letters*, vol. 89, p. 226401, Nov. 2002.
- [193] T. Hotta and E. Dagotto, "Prediction of Orbital Ordering in Single-Layered Ruthenates," *Physical Review Letters*, vol. 88, p. 017201, Dec 2001.

- [194] T. Mizokawa, L. H. Tjeng, G. A. Sawatzky, G. Ghiringhelli, O. Tjernberg, N. B. Brookes, H. Fukazawa, S. Nakatsuji, and Y. Maeno, “Spin-Orbit Coupling in the Mott Insulator Ca_2RuO_4 ,” *Physical Review Letters*, vol. 87, p. 077202, Aug. 2001.
- [195] S. Nakatsuji and Y. Maeno, “Quasi-Two-Dimensional Mott Transition System $\text{Ca}_{2-x}\text{Sr}_x\text{RuO}_4$,” *Physical Review Letters*, vol. 84, pp. 2666–2669, Mar. 2000.
- [196] J. S. Lee, Y. S. Lee, T. W. Noh, S.-J. Oh, J. Yu, S. Nakatsuji, H. Fukazawa, and Y. Maeno, “Electron and Orbital Correlations in $\text{Ca}_{2-x}\text{Sr}_x\text{RuO}_4$ Probed by Optical Spectroscopy,” *Physical Review Letters*, vol. 89, p. 257402, Dec. 2002.
- [197] V. Durairaj, S. Chikara, X. N. Lin, A. Douglass, G. Cao, P. Schlottmann, E. S. Choi, and R. P. Guertin, “Highly anisotropic magnetism in cr doped perovskite ruthenates,” *Physical Review B*, vol. 73, p. 214414, Jun 2006.
- [198] G. Cao, V. Durairaj, S. Chikara, L. E. DeLong, and P. Schlottmann, “Observation of strong spin valve effect in bulk $\text{Ca}_3(\text{Ru}_{1-x}\text{Cr}_x)_2\text{O}_7$,” *Physical Review Letters*, vol. 100, p. 016604, Jan 2008.
- [199] M. Imada, “Universality classes of metal-insulator transitions in strongly correlated electron systems and mechanism of high-temperature superconductivity,” *Phys. Rev. B*, vol. 72, p. 075113, Aug 2005.
- [200] R. Shaheen, M. Akhtar, M. Nadeem, and M. Haque, “Atomistic computer simulation studies of Sr_2RuO_4 and Ca_2RuO_4 ,” *Journal of Physics and Chemistry of Solids*, vol. 64, no. 2, pp. 237 – 245, 2003.
- [201] S. Nakatsuji, V. Dobrosavljević, D. Tanasković, M. Minakata, H. Fukazawa, and Y. Maeno, “Mechanism of Hopping Transport in Disordered Mott Insulators,” *Phys. Rev. Lett.*, vol. 93, p. 146401, Sep 2004.
- [202] J. M. Chen, T. L. Chou, J. M. Lee, S. A. Chen, T. S. Chan, T. H. Chen, K. T. Lu, W. T. Chuang, H.-S. Sheu, S. W. Chen, C. M. Lin, N. Hiraoka, H. Ishii, K. D. Tsuei, and T. J. Yang, “Pressure-induced structural distortion of TbMnO_3 : A combined x-ray diffraction and x-ray absorption spectroscopy study,” *Phys. Rev. B*, vol. 79, p. 165110, Apr 2009.
- [203] A. Niazi, S. L. Bud’ko, D. L. Schlagel, J. Q. Yan, T. A. Lograsso, A. Kreyssig, S. Das, S. Nandi, A. I. Goldman, A. Honecker, R. W. McCallum, M. Reehuis, O. Pieper, B. Lake, and D. C. Johnston, “Single-crystal growth, crystallography, magnetic susceptibility, heat capacity, and thermal expansion of the antiferromagnetic $S = 1$ chain compound CaV_2O_4 ,” *Phys. Rev. B*, vol. 79, p. 104432, Mar 2009.
- [204] H. Fukazawa and Y. Maeno, “Filling control of the mott insulator Ca_2RuO_4 ,” *Journal of the Physical Society of Japan*, vol. 70, no. 2, pp. 460–467, 2001.

- [205] M. Kriener, P. Steffens, J. Baier, O. Schumann, T. Zabel, T. Lorenz, O. Friedt, R. Müller, A. Gukasov, P. G. Radaelli, P. Reutler, A. Revcolevschi, S. Nakatsuji, Y. Maeno, and M. Braden, “Structural Aspects of Metamagnetism in $\text{Ca}_{2-x}\text{Sr}_x\text{RuO}_4$: Evidence for Field Tuning of Orbital Occupation,” *Phys. Rev. Lett.*, vol. 95, p. 267403, Dec 2005.
- [206] M. Van Schilfgaarde, I. Abrikosov, and B. Johansson, “Origin of the invar effect in iron-nickel alloys,” *Nature*, vol. 400, no. 6739, pp. 46–49, 1999.
- [207] T. Kiyama, K. Yoshimura, K. Kosuge, Y. Ikeda, and Y. Bando, “Invar effect of SrRuO_3 : Itinerant electron magnetism of Ru 4d electrons,” *Phys. Rev. B*, vol. 54, pp. R756–R759, Jul 1996.
- [208] R. Ranjan, A. Senyshyn, R. Garg, and H. Boysen, “Magnetic structure and magneto-elastic-structural coupling in Cr-modified SrRuO_3 : A neutron powder diffraction study,” *Journal of Applied Physics*, vol. 109, no. 7, pp. 073908–073908, 2011.
- [209] R. Weiss, “The origin of the invar effect,” *Proceedings of the Physical Society*, vol. 82, no. 2, p. 281, 2002.
- [210] B. Deng, G. Han, and D. FENG, “Development of low thermal expansion superalloys and their application in aerospace,” *J Aeronaut Mater*, vol. 23, pp. 244–9, 2003.
- [211] F. Nakamura, Y. Senoo, T. Goko, M. Ito, T. Suzuki, S. Nakatsuji, H. Fukazawa, Y. Maeno, P. Alireza, and S. Julian, “Pressure-induced ferromagnetic metal for a Mott insulator Ca_2RuO_4 ,” *Physica B: Condensed Matter*, vol. 329, pp. 803–804, 2003.
- [212] V. Egorov, B. Smirnov, V. Shpeizman, R. Nikolaev, and N. Sidorov, “C60 heat capacity anomaly at the orientational phase transition,” *Physics of the Solid State*, vol. 47, no. 10, pp. 1993–1997, 2005.
- [213] R. Nirmala, D. Paudyal, V. Pecharsky, K. Gschneidner, and A. Nigam, “First order transition in $\text{Dy}_5\text{Si}_3\text{Ge}$: Transport and thermal properties, and first principles calculations,” *Journal of Applied Physics*, vol. 109, no. 7, pp. 07A923–07A923, 2011.
- [214] J. Lashley, M. Hundley, A. Migliori, J. Sarrao, P. Pagliuso, T. Darling, M. Jaime, J. Cooley, W. Hults, L. Morales, *et al.*, “Critical examination of heat capacity measurements made on a quantum design physical property measurement system,” *Cryogenics*, vol. 43, no. 6, pp. 369–378, 2003.
- [215] E. Gorelov, M. Karolak, T. Wehling, F. Lechermann, A. Lichtenstein, and E. Pavarini, “Nature of the Mott Transition in Ca_2RuO_4 ,” *Physical review letters*, vol. 104, no. 22, p. 226401, 2010.

- [216] Z. Fang and K. Terakura, “Magnetic phase diagram of $\text{Ca}_{2-x}\text{Sr}_x\text{RuO}_4$ governed by structural distortions,” *Physical Review B*, vol. 64, p. 020509, July 2001.
- [217] N. Moreau, A. Boccara, and J. Badoz, “Jahn-Teller effect and relaxation processes in the $^1\text{T}_{2g}$ state of Ni^{2+} in MgO ,” *Physical Review B*, vol. 10, pp. 64–70, 1974.
- [218] A. Juhin, G. Calas, D. Cabaret, L. Galois, and J. Hazemann, “Structural relaxation around substitutional Cr^{3+} in pyrope garnet,” *American Mineralogist*, vol. 93, no. 5-6, pp. 800–805, 2008.
- [219] N. Menyuk, K. Dwight, and D. Wickham, “Magnetization Reversal and Asymmetry in Cobalt Vanadate (IV),” *Physical Review Letters*, vol. 4, no. 3, pp. 119–120, 1960.
- [220] N. Sakamoto, “Magnetic Properties of Cobalt Titanate,” *Journal of the Physical Society of Japan*, vol. 17, no. 1, 1962.
- [221] G. Cao, Y. Xin, C. S. Alexander, J. E. Crow, P. Schlottmann, M. K. Crawford, R. L. Harlow, and W. Marshall, “Anomalous magnetic and transport behavior in the magnetic insulator $\text{Sr}_3\text{Ir}_2\text{O}_7$,” *Physical Review B*, vol. 66, p. 214412, Dec. 2002.

Vita

Tongfei Qi

Date and place of birth

Nov. 05, 1983, Bi Yang, He Nan Province, China

Educational Institutions Attended and Degrees Awarded

2009-Now PhD program,

University of Kentucky, Lexington, Kentucky, USA

Department of Physics and Astronomy

Advisor: Prof. Gang Cao

Area of Study: Condensed Matter Physics,

2006-2009 M.S., Condensed Matter Physics

University of Kentucky, Lexington, Kentucky, USA

Department of Physics and Astronomy

Advisor: Prof. Gang Cao

2000-2004 B.S., Applied Optics,

Tongji University

Shanghai, China

Advisor: Prof. Yonggang Wu

Professional Positions Held

2009-2012 Research Assistant

University of Kentucky

2006-2009 Teaching Assistant

University of Kentucky

Scholastic and Professional Honors

- University of Kentucky Domestic Travel Student Support Award, 2009-2012
- University of Kentucky Huffaker Travel Scholarships, 2009-2012
- University of Kentucky Outstanding Teaching Assistant Award, 2009

Publication List

1. **T.F. Qi**, O. B. Korneta, L. Li, K. Butrouna, V. S. Cao, X. Wan, P. Schlottmann, R. K. Kaul, and G. Cao, "Spin-orbit tuned metal-insulator transitions in single-crystal $\text{Sr}_2\text{Ir}_{1-x}\text{Rh}_x\text{O}_4$ ($0 \leq x \leq 1$)" , *Physical Review B*, volume 86, pp. 125105, 2012.
2. **T.F. Qi**, O.B. Korneta, X. Wan, L. E. DeLong, P. Schlottmann, G. Cao, "Strong magnetic instability in correlated metallic $\text{Bi}_2\text{Ir}_2\text{O}_7$ " , *Journal of Physics: Condensed Matter*, volume 24, pp. 345601, 2012.
3. **T.F. Qi**, O.B. Korneta, S. Parkin, J. Hu, G. Cao, "Colossal Negative Thermal Expansion Coupled to Magnetic and Orbital Orders in $\text{Ca}_2\text{Ru}_{1-x}\text{M}_x\text{O}_4$ (M= Cr, Mn, Fe and Cu)" , *Physical Review B*, volume 85, pp. 165143, 2012.
4. X. Liu, Vamshi M. Katukuri, L. Hozoi, Wei-Guo Yin, M. P. M. Dean, M. H. Upton, Jung-ho Kim, D. Casa, A. Said, T. Gog, **T. F. Qi**, G. Cao, A. M. Tsvelik, Jeroen van den Brink, and J. P. Hill, "Testing the Validity of the Strong Spin-Orbit-Coupling Limit for Octahedrally Coordinated Iridate Compounds in a Model System $\text{Sr}_3\text{CuIrO}_6$ " , *Physical Review Letters*, volume 109, pp. 157401, 2012.
5. F. Ye, S. Chi, H. Cao, B.C. Chakoumakos, J.A. Fernandez-Baca, R. Custelcean, **T.F. Qi**, O.B. Korneta, G. Cao, "Direct evidence of a zigzag spin chain structure in the honeycomb lattice: A neutron and x-ray diffraction investigation on single crystal Na_2IrO_3 " , *Physical Review B*, volume 85, pp. 180403R, 2012.
6. S. W. Lovesey , D. D. Khalyavin, P. Manuel, L. C. Chapon, G. Cao, **T. F. Qi** "Magnetic symmetries in neutron and resonant x-ray Bragg diffraction patterns of four iridium oxides " , *Journal of Physics: Condensed Matter*, volume 24, pp. 496003, 2012.
7. **T.F. Qi**, O.B. Korneta, S. Chikara, M. Ge, S. Parkin, L.E. De Long, P. Schlottmann, G. Cao, Electron doped $\text{Sr}_2\text{IrO}_{4-\delta}$ ($0 \leq \delta \leq 0.04$): Evolution of a disordered Jeff= 1/2 Mott insulator into an exotic metallic state , *Journal of Applied Physics*, volume 109, pp. 07D906, 2011.
8. **T.F. Qi**, M. Ge, O.B. Korneta, S. Parkin, L.E. De Long, G. Cao, "Structurally-driven metal-insulator transition in $\text{Ca}_2\text{Ru}_{1-x}\text{Cr}_x\text{O}_4$ " , *Journal of Solid State Chemistry*, Elsevier, 2011.
9. O.B. Korneta, **T.F. Qi**, M. Ge, S. Parkin, L.E. De Long, P. Schlottmann, G. Cao, "Correlated giant dielectric peaks and antiferromagnetic transitions near room temperature in pure and alkali-doped $\text{BaMnO}_{3-\delta}$ " , *Journal of Physics: Condensed Matter*, volume 23, pp. 435901, 2011.
10. M. Ge, O.B. Korneta, **T.F. Qi**, S. Parkin, P. Schlottmann, G. Cao, "Magnetic anisotropy and geometrical frustration in the Ising spin-chain system $\text{Sr}_5\text{Rh}_4\text{O}_{12}$ " , *Journal of Applied Physics*, volume 109, pp. 07E164, 2011.

11. M. Ge, **T.F. Qi**, O.B. Korneta, DE De Long, P. Schlottmann, WP Crummett, G. Cao, "Lattice-driven magnetoresistivity and metal-insulator transition in single-layered iridates" , *Physical Review B*, volume 84, pp. 100402, 2011.
12. **T.F. Qi**, O.B. Korneta, S. Parkin, L.E. De Long, P. Schlottmann, G. Cao, "Negative Volume Thermal Expansion Via Orbital and Magnetic Orders in $\text{Ca}_2\text{Ru}_{1-x}\text{Cr}_x\text{O}_4$ " , *Physical Review Letters*, volume 105, pp. 177203, 2010.
13. O.B. Korneta, **T.F. Qi**, S. Chikara, S. Parkin, L.E. De Long, P. Schlottmann, G. Cao, "Electron-doped $\text{Sr}_2\text{IrO}_{4-\delta}$ ($0 \leq \delta \leq 0.04$): Evolution of a disordered $J_{\text{eff}} = 1/2$ Mott insulator into an exotic metallic state" , *Physical Review B*, volume 82, pp. 115117, 2010.